Faculty of Physics and Astronomy

University of Heidelberg

Diploma thesis

in Physics

submitted by

Jan Meier

born in Mannheim

December 2007

Matching of the beam from a negative-ion source for capture in a Penning trap

This diploma thesis was carried out by Jan Meier at the

Max Planck Institute for Nuclear Physics

under the supervision of

Dr. Alban Kellerbauer

Anpassung des Ionenstrahls aus einer negativen Sputter-Ionenquelle für den Einfang in eine Penningfalle:

Ziel dieser Diplomarbeit war es, einen ionenoptischen Aufbau zu entwerfen, welcher einen Strahl negativ geladener Osmiumionen $^{192}Os^-$ bei einer Strahlenergie von 5 keV für den Einfang in eine Penningfalle liefern sollte. Dabei war vorgegeben, $^{192}Os^-$ von anderen Isotopen und sonstigen unerwünschten negativen Ionen zu trennen. Der ionenoptische Aufbau besteht aus einer Sputterquelle für negative Ionen, einer Einzellinse, elektrostatischen Quadrupolen und einem Sektorfeldmagneten zur Massenseparation. Alle Teile des Aufbaus, insbesondere die Sputter-Ionenquelle werden vorgestellt und deren Funktion erklärt. Schließlich werden Simulation und die Ergebnisse der Aufnahme eines Massenspektrums, welche im Erstbetrieb des Aufbaus durchgeführt wurde, miteinander verglichen.

Matching of the beam from a negative-ion source for capture in a Penning trap:

The goal of this diploma thesis was to design a beam line capable of mass separating $^{192}Os^-$ with 5 keV beam energy from other isotopes as well as other unwanted ions. The beam line consists of a negative ion sputter source, einzel lens, electrostatic quadrupoles, and a bending magnet for mass separation. All components of the beam line, in particular the sputter ion source are presented and their function explained in detail. Simulations of the beam line are compared with and a mass spectrum measurement from the first operation of the beam line setup.

CONTENTS

1. Introduction and motivation 1

2. Theoretical background 3
- 2.1 Negative ions 3
- 2.2 Properties of ion beams 6
  - 2.2.1 Phase space 6
  - 2.2.2 Liouville's theorem 7
  - 2.2.3 Emittance 7
  - 2.2.4 Sources 9
- 2.3 Ion-optical simulations 13
  - 2.3.1 Boundary conditions 13
  - 2.3.2 Relaxation method for solving the Laplace equation numerically . . 14
  - 2.3.3 Application of the Relaxation method in simion 8 16
  - 2.3.4 Over-Relaxation 18
  - 2.3.5 Fast adjustment 18
  - 2.3.6 Trajectory calculations in simion 20

3. Negative ion source 23
- 3.1 Basic ionization processes 23
  - 3.1.1 Charge exchange 23
  - 3.1.2 Extraction from a plasma 25
  - 3.1.3 Surface ionization 26
- 3.2 Types of negative ion sources 28
  - 3.2.1 Plasma sources with volume production 28
  - 3.2.2 Plasma sources with surface ionization 28
  - 3.2.3 Sputter type negative ion sources 30
  - 3.2.4 Negative ion source in our experiment 32
- 3.3 Experimental results 36

4. Mass separation and ion-optical elements . . . 43
4.1 Overall setup . . . 43
4.2 Ion optical simulation . . . 45
4.2.1 Source and einzel lens . . . 47
4.2.2 Quadrupole triplets . . . 48
4.2.3 Bending magnet . . . 49
4.2.4 Simulation of mass spectra . . . 53
4.3 Experimental results . . . 54

5. Conclusion . . . 65

A. Matrix formalism of ion optical elements . . . 67
A.1 Drift space . . . 67
A.2 Thin lens . . . 67
A.3 Examples . . . 68
A.4 Acceptance . . . 70
A.5 Einzel lens . . . 70
A.6 Electrostatic quadrupole . . . 74
A.7 Magnetic sector lens . . . 78
A.8 Derivation of mass resolution . . . 81
A.9 Fringe field compensation . . . 83

B. MISS operating manual . . . 87
B.1 Start up . . . 87
B.1.1 Target preparation . . . 87
B.1.2 Target assembly . . . 87
B.1.3 Filling the cesium reservoir . . . 89
B.2 Operation . . . 92
B.2.1 Running up (heating up) the MISS . . . 92
B.2.2 Desired values for operating the MISS . . . 92
B.3 Cleaning . . . 93
B.3.1 Dismantling of the MISS . . . 93
B.3.2 Dismantling step by step . . . 94
B.3.3 Circuit diagram . . . 94

Bibliography . . . 97

1. INTRODUCTION AND MOTIVATION

Ever since the postulation of fermionic antimatter by Paul Dirac in 1931 [1] and the subsequent discovery of the positron by Carl Anderson in 1932 [2], the creation of bound atoms made entirely of antimatter has fuelled the imagination of theorists and experimentalists alike. The PS210 experiment at CERN was the first, in 1995, to create antihydrogen atoms ($\overline{\mathrm{H}}$), albeit at very high velocity and in very small numbers [3]. Since then, several international teams working at CERN's antiproton decelerator (AD) have been developing new schemes, largely based on ion trap techniques, with a view to creating larger numbers of antihydrogen atoms at the lowest possible temperatures.

According to the CPT theorem, an antimatter particle is obtained when the combined operations of charge conjugation, spatial inversion and time reversal are applied to a particle's wavefunction. If CPT symmetry holds exactly, these antimatter partners are expected to have all the same properties as their ordinary counterparts, with some quantities (such as electric charge) inverted. Thus, if $\overline{\mathrm{H}}$ atoms could be produced and trapped in sufficient numbers, a comparison between the H and $\overline{\mathrm{H}}$ spectra could be made. This would constitute a direct experimental test of CPT symmetry. Further, the behavior of antimatter in gravitational fields has never been experimentally observed. Quantum theories of gravity, for instance, allow for a deviation of the gravitational acceleration $\bar{g}$ for $\overline{\mathrm{H}}$ from that for H.

The experiments Athena [4] and Atrap [5] have produced large numbers of $\overline{\mathrm{H}}$ by recombination of antiprotons and positrons in cryogenic Penning traps. They have been able to demonstrate that the generation of sufficient numbers of $\overline{\mathrm{H}}$ atoms for laser spectroscopy is possible. However, these experiments have also shown that the temperature of the generated $\overline{\mathrm{H}}$ was higher than expected from naive models of the cooling and recombination process, and too high for trapping in a magnetic-multipole trap [6, 7]. These results show that in order for confinement in magnetic-multipole to be feasible, $\overline{\mathrm{H}}$ must be produced at 4 K, and possible well below. Since the temperature of the generated $\overline{\mathrm{H}}$ mainly depends on the temperature of the antiprotons prior to recombination with positrons, the cooling of antiprotons prior to recombination is a promising, if not the only, route toward confined $\overline{\mathrm{H}}$.

The direct laser cooling of antiprotons is of course impossible since antiprotons do not have an atomic structure that could absorb and emit photons. Cooling of negative ions, such as antiprotons, could also be achieved by sympathetic cooling, *i.e.* cooling via Coulomb collisions with other, but colder, negatively charged particles. Based on this principle, an

antiproton cooling scheme has been proposed in which negative atomic ions are laser-cooled and then sympathetically cool the antiprotons which are simultaneously confined in the same ion trap [8].

In a recent laser spectroscopy experiment, it was found that negative osmium has a bound excited state of opposite parity with respect to the ground state [9]. This negative ion is therefore presently the first and only candidate for laser cooling of a negative ion. This thesis work was embedded in a larger project whose aim it is to determine whether laser cooling of negative osmium ions in a Penning trap is possible. For this purpose, a Penning trap was designed to capture negtive Os ions of at most 5 keV energy.

The goals of this diploma thesis were defined as follows:

- To adapt the design of an existing negative-ion source for operation at 5 keV;
- To produce the technical drawings for this source and oversee its construction;
- To design a beam line for the 5-keV beam, including a mass separation stage in order to suppress isotopic as well as molecular contaminants from the source;
- To build up the entire system and measure its performance in terms of efficiency and mass resolving power.

To that end, a negative-ion sputter source for the generation of a negative-ion beam was built and tested (Chapter 3). Further, the beam line and mass separation stage for the suppression of isotopic as well as molecular contaminants from the source was designed, built, and characterized (Chapter 4).

2. THEORETICAL BACKGROUND

In this chapter, first, negative ions and their properties are introduced. The larger the electron affinity E_A of an atom or molecule, the more easily it forms a negative ion. Therefore, the negative ion yield in ion sources is high for particles with large electron affinities.

To find a convenient beam line design, it is in general helpful not to try to calculate single ion trajectories but to consider an ensemble of ions as a beam. Moreover, a beam line can be considered as a sequence of ion optical elements, where each element has a specific effect on the ion beam. With these considerations the behavior of ions passing the beam line can be visualized and understood. Therefore, in the present chapter, main ion beam properties and ion optical elements are introduced.

With the progress of computer design and the increasing calculating capacity, direct, numerical calculations of ion trajectories have become possible. Such calculations were made here with simion 8. Therefore, basic approaches to numerical field and ion trajectory computations are finally presented in this chapter.

2.1 Negative ions

Diverse molecules and many elements have bound (singly charged) negative ion states. In these cases, the formation of a bound negative ion state, *i.e.* the capturing of an additional electron to a neutral atom or molecule X, is exothermic. The energy released in this process is called electron affinity E_A:

$$X + e^- \longrightarrow X^-, \tag{2.1}$$

$$E_\mathrm{tot}(X) + E_\mathrm{kin}(e^-) + m_\mathrm{e}c^2 \longrightarrow E_\mathrm{tot}(X^-) + E_\mathrm{kin}(e^-) + E_\mathrm{A}(X). \tag{2.2}$$

Where $E_\mathrm{tot}(X)$ and $E_\mathrm{tot}(X^-)$ are total energies of atom and ion in the lowest (hyperfine-structure) energy level ground state respectively. $E_\mathrm{kin}(e^-)$ is the kinetic energy of the electron e^- and m_e its mass. The electron affinity of an element X can thus be expressed as:

$$E_\mathrm{A}(X) = E_\mathrm{tot}(X) - E_\mathrm{tot}(X^-) + m_\mathrm{e}c^2. \tag{2.3}$$

Elements with positive E_A form bound negative ions, while such with E_A smaller than zero do not have bound states. Nevertheless, some of the elements with negative electron

	1	2	3	4	5	6	7	8	9	10	11	12	13	14	15	16	17	18
1	1 H 0.75																	2 He <0
2	3 Li 0.62	4 Be <0											5 B 0.28	6 C 1.26	7 N <0	8 O 1.46	9 F 3.40	10 Ne <0
3	11 Na 0.55	12 Mg <0											13 Al 0.43	14 Si 1.39	15 P 0.75	16 S 2.08	17 Cl 3.61	18 Ar <0
4	19 K 0.50	20 Ca 0.02	21 Sc 0.19	22 Ti 0.08	23 V 0.53	24 Cr 0.68	25 Mn <0	26 Fe 0.15	27 Co 0.66	28 Ni 1.16	29 Cu 1.24	30 Zn <0	31 Ga 0.41	32 Ge 1.23	33 As 0.81	34 Se 2.02	35 Br 3.36	36 Kr <0
5	37 Rb 0.49	38 Sr 0.05	39 Y 0.31	40 Zr 0.43	41 Nb 0.89	42 Mo 0.75	43 Tc 0.55	44 Ru 1.05	45 Rh 1.14	46 Pd 0.56	47 Ag 1.30	48 Cd <0	49 In 0.40	50 Sn 1.11	51 Sb 1.05	52 Te 1.97	53 I 3.06	54 Xe <0
6	55 Cs 0.47	56 Ba 0.14	57 La 0.47	72 Hf ~0	73 Ta 0.32	74 W 0.82	75 Re 0.15	76 Os 1.08	77 Ir 1.56	78 Pt 2.13	79 Au 2.31	80 Hg <0	81 Tl 0.38	82 Pb 0.36	83 Bi 0.94	84 Po 1.9	85 At 2.8	86 Rn <0

Fig. 2.1: Periodic table of elements (not complete) with their rounded electron affinities in units of eV. The values are adapted from Ref. [10] as being the most reliable. They are rounded to the second position after decimal point (except Po and At where the error was around 0.2 eV).

affinity can form instable negative ions with lifetimes up to a few hundred µs, such that it is possible to accelerate them and detect them in a mass spectrometer. Negative ions with rather short lifetimes, down to the order of 10^{-15} s, can be detected as resonances in electron scattering experiments for example. In Ref. [10] diverse principles of negative ion spectroscopy are introduced. Chlorine has the largest known atomic electron affinity of ~ 3.61 eV. In Fig. 2.1 elements with their (rounded) electron affinities, recommended from Andersen *et al.* (Ref. [10]) as being the most reliable, are shown.

The larger the electron affinity of an atom, the more easily the atom forms a negative ion. The negative ion yield of an element in diverse processes, *e.g.* in secondary particle emission which also occurs in the negative ion source of this experiment, is therefore in general high if the electron affinity of that element is large. For instance, in the mass spectrum (Fig. 4.13) of the source operated with FeS it can be seen that almost no Fe^- [$E_A(Fe) \approx 0.15$ eV] is generated, but much more S^- [$E_A(S) \approx 2.08$ eV].

Electron correlation effects are responsible for the stability of atomic negative ions. The correlation effects are a result of Pauli exclusion principle and Coulomb repulsion. Since electrons are fermions, they are subject to the Pauli exclusion principle, and therefore the overlap of their wave functions is minimal. This results in a maximum average distance between the electrons, and so in a minimal Coulomb energy of the electron interaction (electrostatic repulsion). If an electron is added to a neutral atom, energy (correlation energy) can be released due to this correlation effect.

Negative ions do not have a large number of excited states such as neutral atoms (Rydberg series), because the other electrons shield the nucleus against an outer excited

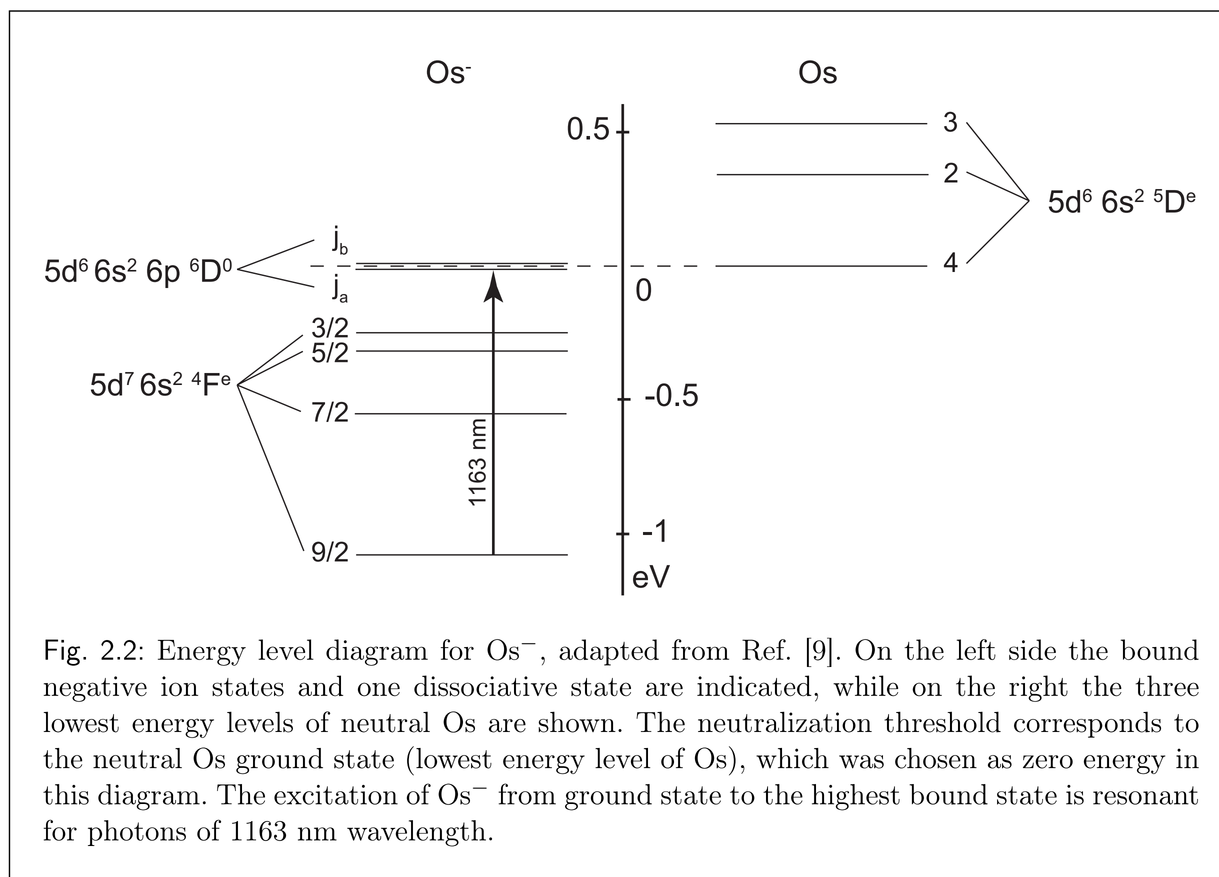

Fig. 2.2: Energy level diagram for Os^-, adapted from Ref. [9]. On the left side the bound negative ion states and one dissociative state are indicated, while on the right the three lowest energy levels of neutral Os are shown. The neutralization threshold corresponds to the neutral Os ground state (lowest energy level of Os), which was chosen as zero energy in this diagram. The excitation of Os^- from ground state to the highest bound state is resonant for photons of 1163 nm wavelength.

electron too strongly to form highly excited states. In general the Coulomb interaction between an outer electron and the nucleus is suppressed in negative ions. Nevertheless, some atomic negative ions do have excited bound states.

In 2000, Bilodeau *et al.* [9] observed the first negative ion with bound excited state of opposite parity with respect to its ground state, in a laser photodetachment threshold (LPT) experiment with negative osmium $^{192}Os^-$ (natural abundance $\approx$41%). An electron affinity of $\approx$1.08 eV was measured. One unstable (dissociative) state was found to be just $\approx$3.5 meV ($5d^6\ 6s^2\ 6p\ ^6D^0$, j_b) above the neutralization threshold (see Fig. 2.2). The energy level of the highest bound excited state ($5d^6\ 6s^2\ 6p\ ^6D^0$, j_a), which is the one with opposite parity with respect to the ground state, was measured to be only $\approx$11.5 meV below the neutralization threshold, *i.e.* the binding energy of this state is only $\approx$11.5 meV.

It was deduced from the measured cross-section that the transition between the ground state and this state is an allowed dipole transition. The corresponding photon wavelength of this transition is about 1163 nm. The existence of this bound state qualifies osmium as the only known candidate for laser cooling of negative ions.

2.2 Properties of ion beams

The motion of particles moving in electromagnetic fields is governed by the Lorentz equation:

$$m\dot{\vec{v}} = q \cdot (\vec{E} + \vec{v} \times \vec{B}). \tag{2.4}$$

To find (exact) solutions for the particle trajectories, the fields have to be known exactly. Mostly electromagnetic fields cannot be determined analytically, and so the fields and particle trajectories have to be calculated numerically. This was done here with the field- and ion trajectory simulation program simion 8, which is introduced in Sec. 2.3.

Another way to approximate particle motions is to separate the beam line into optical elements. This is similar to light optics, where optical elements such as lenses and drift spaces are used. The beam behavior can then be described with matrices. In this section, basic beam properties and the beam behavior in different optical elements are introduced. Properties of optical elements used in our setup and their transformation matrices are presented in the Appendix A.

2.2.1 Phase space

Basic definitions of beam properties are based on phase space. The phase space is a six-dimensional space spanned by the three space coordinates (x, y, z) and three momentum coordinates (p_x, p_y, p_z). For a fixed time, each particle occupies a certain point in phase space, described by the six coordinates (x, y, z, p_x, p_y, p_z). Classically, from this position in phase space the trajectory, *i.e.* the position of the particle in phase space is determined for all future times.

For a group of particles, a six dimensional phase space volume $\sim \Delta x \Delta y \Delta z \Delta p_x \Delta p_y \Delta p_z$ can be found, containing all particles' positions in phase space. If particle motions in the three dimensions x, y and z are independent of each other, the projections of the phase space in the three planes (x, p_x), (y, p_y) and (z, p_z) are uncorrelated. Graphs of these projections are called "phase space diagrams". Generally the phase space volume (area) in a subspace is defined as

$$S_x = \int\int dx dp_\mathrm{x}. \tag{2.5}$$

The definition is analogous for the y- and z-direction.

For independent motions in the three space coordinates, the phase space volume in the entire six dimensional phase space is then given by the product of areas in the subspaces

$$S = S_x S_y S_z. \tag{2.6}$$

2.2.2 Liouville's theorem

Liouville's theorem states that in conservative fields and without particle interaction, the phase space density, and in particular the phase space volume of an ensemble of particles, is conserved. This means, for example, that it is impossible to decrease or increase the phase space volume of a collection of ions with static electric or magnetic fields. In contrast, this does not need to be true for time-dependent fields.

It should be noted that in this theorem, the amount of volume is constant but the shape of a volume can change significantly, *i.e.* the phase space volume behaves like an incompressible fluid. For independent motions in x-, y- and z-direction, Liouville's theorem is valid for the three subspaces (x, p_x), (y, p_y) and (z, p_z), *i.e.* S_x, S_y and S_z are then conserved respectively, if only conservative fields are applied.

2.2.3 Emittance

Since the phase space is conserved under certain conditions, it can be used to characterize a collection of particles. Let us consider a group of particles having an average momentum p_0. To describe the collection of particles with the subspaces (x, p_x), (y, p_y) and (z, p_z) the momenta can also be substituted by $x' := p_x/p_0$, $y' := p_y/p_0$ and $z' := p_z/p_0$ respectively. Graphs of the so defined subspaces (x, x'), (y, y') and (z, z') are known as emittance diagrams. The emittance ϵ is defined as the area in an emittance diagram. The phase space volume (area) and the emittance are connected through

$$S_x = \int\int dx\ dp_x, \tag{2.7}$$

$$= p_0 \int\int dx\ d\frac{p_x}{p_0}, \tag{2.8}$$

$$= p_0\ \epsilon_x, \tag{2.9}$$

and accordingly for ϵ_y and ϵ_z.

Now we consider a continuous ion beam and choose a coordinate system in which the average momentum points along the z-direction. To characterize such a continuous ion beam, the transverse two-dimensional phase space projections (x, x') and (y, y') are convenient. In rotationally symmetric systems, the beam can be characterized with one phase space projection $(r, r') := (x, x') = (y, y')$. Usually the approximation:

$$r' = \frac{p_r}{p_0} = \tan \alpha_r \approx \alpha_r, \tag{2.10}$$

is convenient for ion beams. The quantity r' can therefore be considered as the angle between average momentum $(p_z = p_0)$ and particle momentum, projected into to (r, z)-plane, where p_r is the component of the ion momentum in the r direction. The units

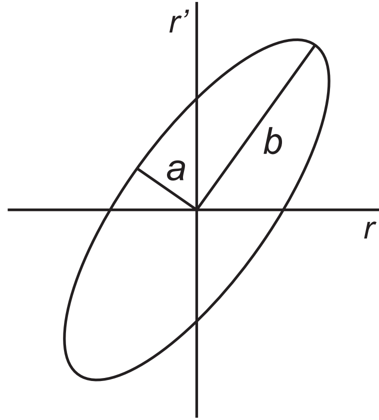

Fig. 2.3: Emittance diagram. The area of the ellipse is given by $A = \pi \cdot ab$ mm mrad.

are usually mm for r, and mrad for r'. Since ion beams often have elliptical shapes in phase space diagrams, the emittance is mostly expressed in π mm mrad. In these units the emittance is equal to the product $a \cdot b$ of the semiaxis of the ellipse (Fig. 2.3), since the area A of the ellipse is given by $\pi \cdot ab$.

From Eq. (2.9) we find that the emittance depends on the average momentum p_0, since the phase space is constant. That means that accelerations and decelerations, for example, change the emittance of an ion beam. The normalized emittance ϵ_{n} is independent of the particle momentum and is constant under certain conditions, like the phase space volume. The normalized emittance $\epsilon_{\mathrm{n}r}$ in a transverse phase space projection (r, r') is defined as

$$\epsilon_{\mathrm{n}r} := \pi \left(\frac{\int \int dr dr'}{\pi} \right) \sqrt{E}, \tag{2.11}$$

or

$$\epsilon_{\mathrm{n}r} := \pi \left(\frac{\int \int dr dr'}{\pi} \right) \beta\gamma, \tag{2.12}$$

where E is the particle energy and β the ratio of particle velocity to the speed of light v/c, and $\gamma := 1/\sqrt{1-\beta^2}$. Often the displacement of beam particles from the beam axis and the angles of their motion follow Gaussian distributions. Then the shape of the emittance can be reasonably approximated with an ellipse. This emittance ellipse contains a fraction of the beam that has to be indicated in addition to the emittance, *e.g.* the emittance ellipse contains a fraction of the beam out to 2σ of the distribution, or it contains 80% of the beam. The normalized emittance defined in Eq. (2.11) is usually expressed in units of π mm mrad $\sqrt{\mathrm{MeV}}$, while that defined in Eq. (2.12) is expressed in units of π mm mrad. The

parameter β can be approximated non-relativistically:

$$\beta \approx \frac{1}{c}\sqrt{\frac{2qU}{m}} \approx 1.465 \cdot 10^{-3}\sqrt{\frac{\xi U_{\mathrm{kV}}}{A}}, \tag{2.13}$$

where q is the ion charge, U the acceleration voltage of the beam, m the ion mass, ξ the charge state of the ion, U_{kV} the acceleration voltage of the beam in kV, and A the atomic mass number.

In relativistic cases, γ can be numerically calculated directly from the beam energy and β deduced from it afterward:

$$\gamma = \frac{qU}{m_0 c^2} + 1, \tag{2.14}$$

where U is the acceleration voltage of the beam, q the ion charge and m_0 the ion's rest mass.

2.2.4 Sources

Now we consider a particle source with exit apertures like in Fig. 2.4. Particles are moving from left to right. In ion sources usually the second aperture is that of an extraction electrode. For simplicity, we assume that ions are generated and already accelerated when they arrive at the exit aperture on the left side in Fig. 2.4. So both apertures are at equal potential and no particle acceleration between them takes place. Particles are emitted from the whole aperture along r at z_1 with different directions of motion r_1'. Not all of them can pass the second aperture at z_2, which is positioned after a drift length L. Only those particles inside the parallelogram in the emittance diagram (on the right-hand side of Fig. 2.4) are able to pass the second aperture. The diameter of both apertures and their distance determine the shape and amount of the particle beam emittance in the emittance diagram.

If the distributions of the starting position r_1 and particle direction r_1' were uniform, the emittance would indeed have a parallelogram-like shape. The ellipse inscribed in the parallelogram in Fig. 2.4 is that with the largest phase space that would pass through the second aperture without any loss.

Figure 2.5 shows the result of an emittance measurement. The beam intensity is plotted as a function of the position in phase space (r, r'), where 100% beam intensity corresponds to the maximum beam intensity. We can see that this beam intensity profile is rather inhomogenious and somewhat symmetrically distributed around the maximum intesity. Gaussian distributions of r and r' around the maximum intensity coordinates seem to be reasonable distributions. In Fig. 2.6, the corresponding surface plot is shown, *i.e.* this plot can be interpreted as Fig. 2.5 observed from the top. An ellipse, with its center at maximum beam intensity and circumscribing a large percentage of the beam is a reasonable approximation of the beam emittance.

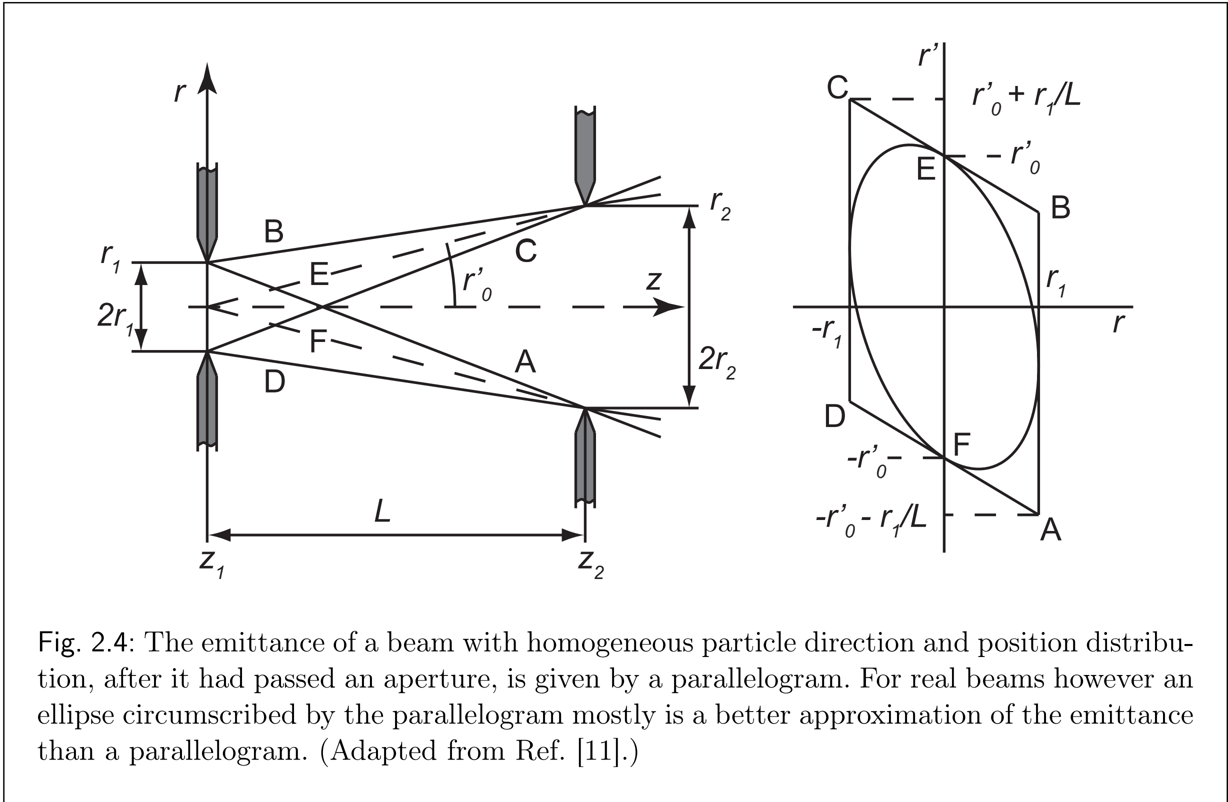

Fig. 2.4: The emittance of a beam with homogeneous particle direction and position distribution, after it had passed an aperture, is given by a parallelogram. For real beams however an ellipse circumscribed by the parallelogram mostly is a better approximation of the emittance than a parallelogram. (Adapted from Ref. [11].)

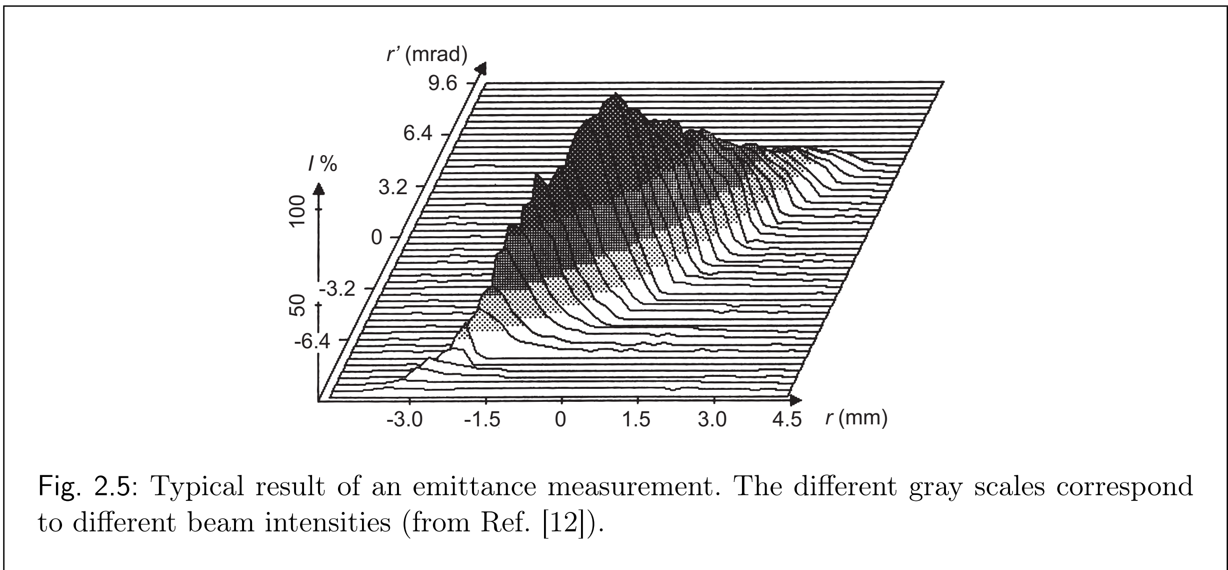

Fig. 2.5: Typical result of an emittance measurement. The different gray scales correspond to different beam intensities (from Ref. [12]).

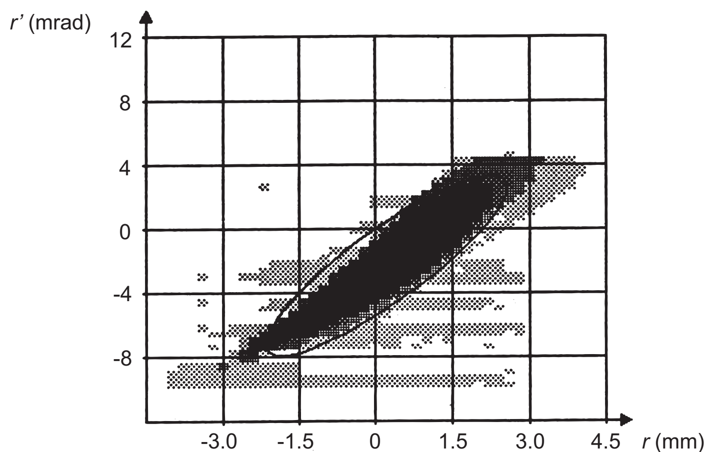

Fig. 2.6: Surface plot of the results in Fig. 2.5 (from Ref. [12]). The gray scale corresponds to diverse percentages of the total beam current (95, 90, 85, and 80%). The plotted ellipse is a reasonable approximation of the emittance.

Ion optical elements

The ion optical elements used in the beam line are, generally speaking, different types of lenses and drift spaces. The beam behavior and the transformation properties can be described in an analogous way to light optics. As in light optics, a space in which a beam propagates without any forces acting on beam particles, *i.e.* a field free region, is called drift space. In this space, beam particles maintain their direction of motion, *i.e.* a divergent or parallel beam remains divergent or parallel.

An einzel lens consists of three rotationally symmetric electrodes and a voltage on the central electrode. The analogon of an einzel lens in light optics is a thick lens. An einzel lens has a focusing effect on ion beams.

An electrostatic quadrupole can be considered as another type of lens. It is realized with a configuration of four electrodes and corresponding voltages generating a quadrupole field, where all forces act perpendicular to the axis of propagation of the beam. This lens has different transformation properties for the two different directions perpendicular to the axis of propagation. In one direction it focuses a beam, while in the other a beam is defocused.

By supplying a magnetic field perpendicular to the axis of propagation such that the beam is bent over a sector, the beam carries out a circular motion. In this plane, the beam is focused, *i.e.* a magnetic sector lens is realized. In the direction normal to this plane no forces act on ions since they move along the magnetic field lines. Therefore, in this direction the beam behaves like in a drift space.

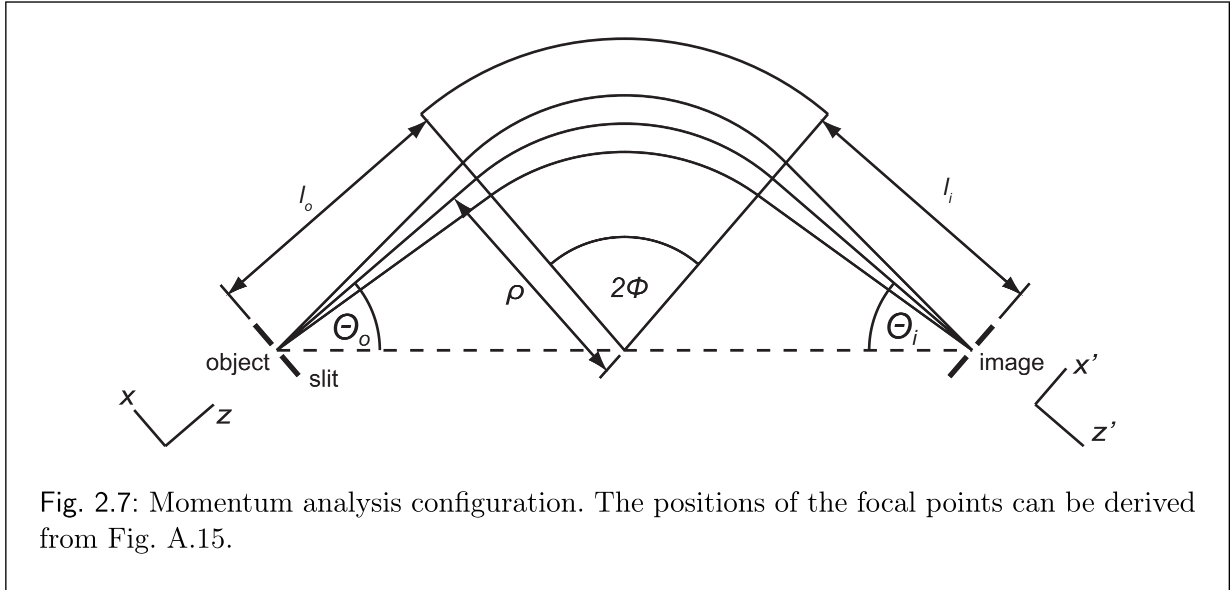

Fig. 2.7: Momentum analysis configuration. The positions of the focal points can be derived from Fig. A.15.

The transfer matrices and detailed properties of all ion optical elements which have been briefly introduced here are discussed in detail in Appendix A.

Momentum and mass analysis

The ion beam generated in our source consists of fractions of different molecules, elements and isotopes. A desired $^{192}Os^{-}$ ion beam of maximal purity makes the laser cooling experiment as easy as possible. Therefore, properties of mass analysis, *i.e.* the resolving power of our mass separator configuration is of particular interest.

The mass separator configuration in the beam line is realized with a bending magnet (90° magnetic sector lens) and entrance and exit slits. As is shown in detail in Appendix A, magnetic sectors can be used for momentum analysis. This can be achieved by an object-image relation (Fig. 2.7) and with the use of slits. An object in x-position is defined by the space between two slits, at a focal plane in distance l_i, before the magnetic sector field. The beam is re-focused onto an image plane behind the magnetic field region. All ions with the same momentum (assuming all ions have equal charge and equal object position) are focused to one x'-position at the image plane, with distance l_o behind the magnetic sector field. With two slits in the image plane, ions with desired momentum can be separated.

Displacements from the desired image position can occur because of displacements of the object and because of differences in the ion momentum. If the beam is monoenergetic, the momentum is only dependent on the ion mass, so that the magnetic sector acts as a mass separator.

Figure 2.7 presents an example of a momentum or mass separator. For a symmetric

geometry, *i.e.* $l_i = l_o$ and $\Theta_i = \Theta_o$, we find: $l_i = l_o = g = \rho / \tan\Phi$. This can be derived, considering the configuration in Fig. 2.7 as a sequence of two equal magnetic sector lenses with sector angle Φ, introduced in Sec. A.7. Figure A.15 shows such a sector lens.

It is assumed that the images of two different masses are just resolved if the distance of their centers equals their expansion. For a monoenergetic beam, a symmetric geometry, and an object (slit) width w_o, *i.e.* the distance between the two slits defining the object, the resolution is given by

$$\frac{m}{\Delta m} = \frac{\rho}{w_o}. \tag{2.15}$$

For an object width of zero, *i.e.* all particles are starting from one position (x-coordinate) but with an energy of E and an energy distribution with full width at half maximum of ΔE the resolution is given by

$$\frac{m}{\Delta m} = \frac{E}{\Delta E}. \tag{2.16}$$

For a beam with a full width at half maximum of its energy distribution ΔE and a slit width of w_o, particles with a relative mass difference of:

$$\frac{\Delta m}{m} \geq \frac{w_o}{\rho} + \frac{\Delta E}{E}, \tag{2.17}$$

can in principle be resolved by a 90° mass separation configuration. A derivation of this can be found in the Sec. A.8. Some additional notes about mass resolution can be found in Refs. [11] and [13].

2.3 Ion-optical simulations

For the simulation of the beam line, fields and ion trajectories had to be numerically calculated. Therefore, in this section, first, the basic problem of finding solutions for a potential function V is presented. Furthermore, boundary conditions are introduced, and a motivation why numerical approximations are necessary is given. After this, basic principles of numerical approximations of static electric and magnetic fields, accomplished by simion 8, are introduced. All potential calculations are based on numerical computations (relaxation method) of electric and magnetic potentials. In simion, magnetic and electrostatic potentials are treated in the same way. Simion 8 is also able to compute ion trajectories by numerical integration, which is also presented here.

2.3.1 Boundary conditions

The basic problem in electrostatics is to find a solution $V(\vec{r})$ of the Poisson equation:

$$\Delta V(\vec{r}) = -\frac{\rho(\vec{r})}{\epsilon_0}, \tag{2.18}$$

where V is the electrostatic potential, ρ the charge density, and ϵ_0 the dielectric constant. If $\rho(\vec{r})$ is known, and there are no boundary conditions, the solution of the Poisson equation is given by:

$$V(\vec{r}) = \frac{1}{4\pi\epsilon_0} \int d^3r' \frac{\rho(\vec{r})}{|\vec{r} - \vec{r'}|}. \tag{2.19}$$

However, this is rarely the case. Mostly $\rho(\vec{r})$ is given in a finite volume with boundary conditions (*e.g.* electrodes with fixed voltages) on the volumes surface (boundary surface) and on surfaces inside the volume. These boundary conditions can be classified in two ways:

1) Dirichlet boundary conditions:
   V is given on the boundary surface.

2) Neumann boundary conditions:
   $\vec{n} \cdot \vec{\nabla} V = -\vec{n} \cdot \vec{E}$ is given on the boundary surface.

Both kinds of boundary conditions can be given simultaneously on different parts of the surface. The solution $V(\vec{r})$ of the problem is unique if boundary conditions are closed, *i.e.* they are given on the whole boundary surface ("first uniqueness theorem"). For more information on how to solve such problems analytically see Ref. [14], for example. It should be mentioned that there are only few, and very special cases, for which an analytical solution exists. Therefore, in most cases, the potential function $V(\vec{r})$ has to be calculated numerically.

2.3.2 Relaxation method for solving the Laplace equation numerically

If we consider a volume with charge only on electrodes but not in the space between them (*e.g.* electrodes in vacuum and if space charge effects are neglected), the Laplace equation

$$\Delta V(\vec{r}) = 0, \tag{2.20}$$

has to be solved for volume elements outside of electrodes, instead of the Poisson equation, while the boundary conditions are given by the electrode surfaces and the boundary surface of the volume.

Suppose a function $f(x)$, which is differentiable a sufficient number of times, and which

can be expanded into a Taylor series:

$$\begin{aligned}
\text{I} \qquad & f(x+\Delta x) = f(x) + f'(x)\Delta x + \frac{1}{2}f''(x)\Delta x^2 + \frac{1}{6}f'''(x)\Delta x^3 + ..., \\
\text{II} \qquad & f(x-\Delta x) = f(x) - f'(x)\Delta x + \frac{1}{2}f''(x)\Delta x^2 - \frac{1}{6}f'''(x)\Delta x^3 + ..., \\
\text{I}+\text{II} \qquad & f(x+\Delta x) + f(x+\Delta x) = 2f(x) + f''(x)\Delta x^2 + O(\Delta x^4), \\
\Rightarrow \qquad & f''(x) = \frac{f(x+\Delta x) + f(x-\Delta x) - 2f(x)}{\Delta x^2} + O(\Delta x^2),
\end{aligned}$$

i.e. for "small" Δx the following approximation can be used

$$f''(x) \approx \frac{f(x+\Delta x) + f(x-\Delta x) - 2f(x)}{\Delta x^2}. \tag{2.21}$$

Now we divide the volume in which the Laplace equation is to be solved into small cubes (finite elements) of equal dimensions. The center points of these cubes constitute a lattice, where each has an equal distance h to each nearest neighbor center point. Now we estimate the potential at the center points only:

$$V(n_x, n_y, n_z) := V(x = n_x h, y = n_y h, z = n_z h), \tag{2.22}$$

where $n_x, n_y, n_z \in \mathbb{Z}$, and $\Delta x = \Delta y = \Delta z = h$. The method of dividing a volume into small cubes and estimating values of a quantity inside each cube is called "finite-element method".

Inserting the approximation for $f''(x)$ [Eq. (2.21)] into the three-dimensional Laplace equation (in Cartesian coordinates):

$$\Delta V(\vec{r}) = \frac{\partial^2 V(x,y,z)}{\partial x^2} + \frac{\partial^2 V(x,y,z)}{\partial y^2} + \frac{\partial^2 V(x,y,z)}{\partial z^2} = 0,$$

and with Eq. (2.22) we find

$$\begin{aligned}
& \frac{V(n_x+1,n_y,n_z) + V(n_x-1,n_y,n_z) - 2V(n_x,n_y,n_z)}{h^2} \\
+ & \frac{V(n_x,n_y+1,n_z) + V(n_x,n_y-1,n_z) - 2V(n_x,n_y,n_z)}{h^2} \\
+ & \frac{V(n_x,n_y,n_z+1) + V(n_x,n_y,n_z-1) - 2V(n_x,n_y,n_z)}{h^2} = 0.
\end{aligned} \tag{2.23}$$

This leads us to:

$$\begin{aligned}
V(n_x,n_y,n_z) = \frac{1}{6}[& V(n_x+1,n_y,n_z) + V(n_x-1,n_y,n_z) + V(n_x,n_y+1,n_z) \\
& + V(n_x,n_y-1,n_z) + V(n_x,n_y,n_z+1) + V(n_x,n_y,n_z-1)].
\end{aligned} \tag{2.24}$$

This equation can be used to iteratively approximate the potential at the lattice points. The points belonging to an electrode or defining boundary conditions (points on the volume boundary) have fixed potentials. As an initial value for all other none electrode points, the potential can be set to 0 V. The potential at points outside of electrodes can then iteratively approximated, with the help of Eq. (2.24) as follows:

$$\begin{aligned} V_{n+1}(n_x, n_y, n_z) = \frac{1}{6}[&V_n(n_x+1, n_y, n_z) + V_n(n_x-1, n_y, n_z) + V_n(n_x, n_y+1, n_z) \\ &+V_n(n_x, n_y-1, n_z) + V_n(n_x, n_y, n_z+1) + V_n(n_x, n_y, n_z-1)], \end{aligned} \tag{2.25}$$

i.e. the potential V_{n+1} at a lattice point of the next iteration is calculated by building the average of the potential V_n of all nearest neighbor points of the present iteration. A condition for stopping the iteration process could be to claim $|V_{n+1}(n_x, n_y, n_z) - V_n(n_x, n_y, n_z)| < \epsilon$ for all lattice points. The value ϵ has to be chosen depending on the desired accuracy. This iteration process is called the relaxation method.

2.3.3 Application of the Relaxation method in simion 8

Simion uses the finite-element method, as explained above, to estimate the potential at different points inside a given volume, with the help of the relaxation method. In simion there are two kinds of points in a given volume, electrode and non-electrode points. The user defines the geometry of the electrodes and their voltages, *i.e.* the user defines which points in the volume are electrode points and which constant voltages are supplied at those points. Simion then, on the other hand, computes the potential at non-electrode points with the relaxation method (as described above).

The voltages of all lattice points of a volume are saved in a so called potential array (PA). As already explained, the solution of an electrostatic problem is unique if boundary conditions are given on the whole surface ("closed conditions"). Dirichlet boundary conditions are given by the user in defining the shape and voltages of electrodes. If the user does not define points on the volume surface as electrode points, simion automatically sets the Neumann-like boundary condition $\vec{n} \cdot \nabla \vec{V} = 0$ to all surface points. That means that every PA file in simion automatically has closed boundary conditions in order to ensure the uniqueness of the solution of the potential function inside the volume. Those closed conditions always consist of some combination of Dirichlet and Neumann-like boundary conditions (Fig. 2.8). The user must take care of using convenient boundary conditions for his/her specific problem. Figures 2.9 and 2.10 show potential views in a plane cutting through the center of the electrode(s). The central electrode is at equal voltage in both views. The presence of a second electrode, set to 0 V, changes the potential function significantly. In the example of Fig. 2.9 simion calculated all volume points to be at equal potential, which is not the case in Fig. 2.10.

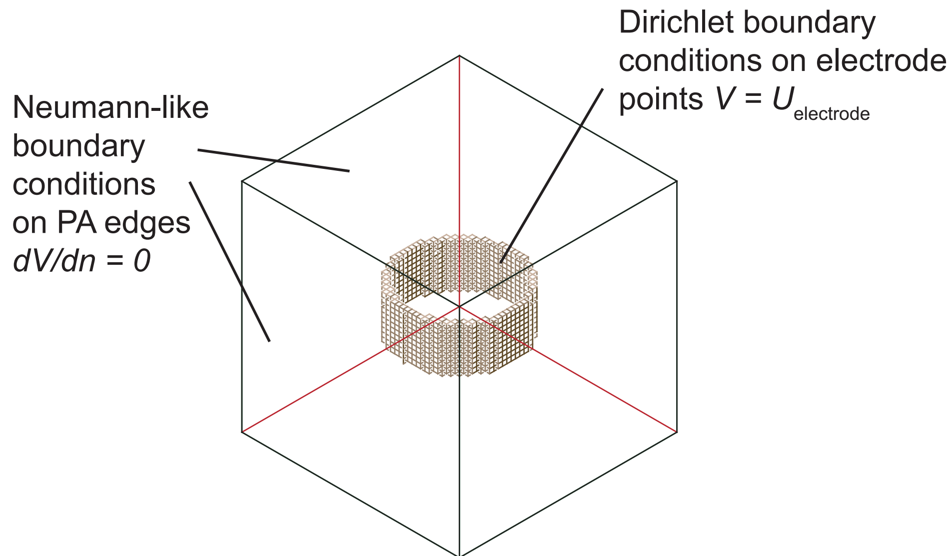

Fig. 2.8: (Color.) 3d view of a potential array. Electrode points define Dirichlet boundary conditions while simion automatically defines the Neumann-like boundary condition $\vec{n}\cdot\nabla\vec{V} = 0$ for all non-electrode PA edge points.

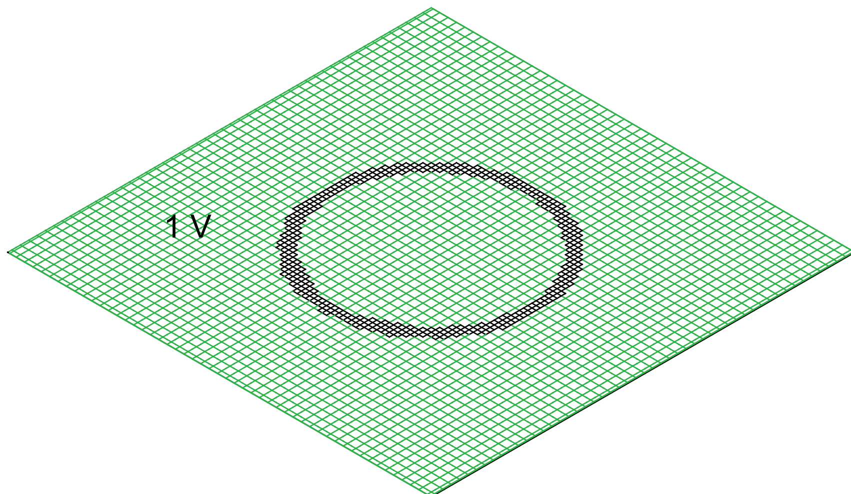

Fig. 2.9: (Color.) Potential view for a plane slicing the electrode in the center. The electrode voltage is set to 1 V.

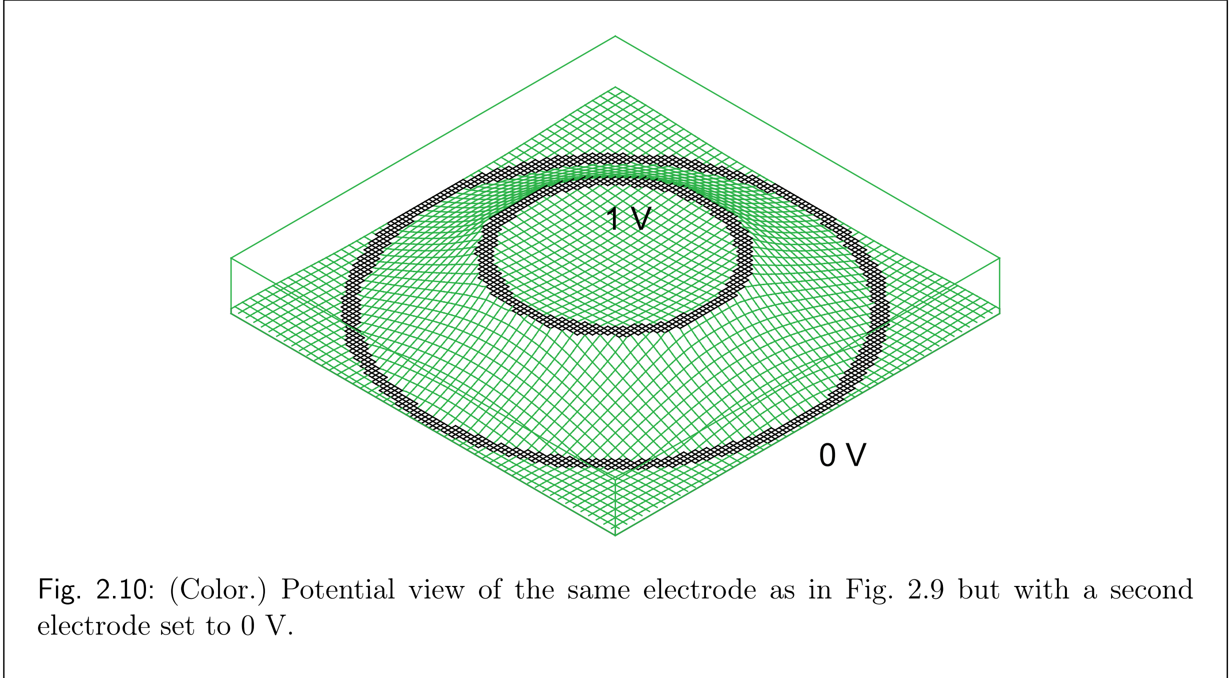

Fig. 2.10: (Color.) Potential view of the same electrode as in Fig. 2.9 but with a second electrode set to 0 V.

2.3.4 Over-Relaxation

The numerical approximation process in simion is called refining. In order to speed up the refining process in reducing the number of iterations, simion uses a variant of the relaxation method, the so called over-relaxation:

$$V_{n+1}^{\mathrm{or}} = V_n + (1 + a)(V_{n+1} - V_n), \tag{2.26}$$

where V_{n+1} is calculated with the usual relaxation method, and $a \in [0, 1]$ is called over-relaxation factor.

For each potential array there is an optimal over-relaxation factor a that is generally in the range of 0.9. Simion uses a dynamically self-adjusting factor to minimize the number of iterations. See fourth line in Tab. 2.1 (equation for F). Table 2.1 gives an overview of the over-relaxation calculation in simion. For more information see Ref. [15].

2.3.5 Fast adjustment

Simion has a feature called "fast voltage adjustment method". That means if a potential array is already refined, and electrode voltages have to be changed, it is not necessary to refine the array again with the changed electrode voltages. The potential in each point of the array can be calculated by re-scaling the potentials. Let us now consider the particular case of an array with three electrodes at different voltages. Simion here makes use of the

iteration	over-relaxation factor
1	0.40
2-10	0.67
>10	$F = (F_{\text{old}} \cdot Hist) + (1 - Hist) \cdot (F_{\max} - DF \cdot Error)$
Where:	F_{old} =factor used in prior iteration
	$Hist$ =History factor (*e.g.* 0.70)
	$F_{\max}$ =Max over-relaxation (*e.g.* 0.90)
	$DF = F_{\max} - 0.40$
	$Error = \frac{1}{1+\frac{DEL}{2DELM}}$
	DEL =Max prior abs single point change
	$DELM$ =Convergence Goal (*e.g.* 0.005)

Tab. 2.1: Overview of the over-relaxation calculation in simion (adapted from Ref. [15]).

linear property of the Laplace equation. The potential function of three electrodes with voltages U_1, U_2 and U_3 is equal to a superposition of three different situations, where in turn only one of them has its corresponding voltage and the others are set to 0 V (Fig. 2.11). Simion saves each situation in its own potential array, called "electrode array", with the names "file.PA1", "file.PA2" and "file.PA3". The composite potential is saved in the array "file.PA0". While the potential at any location (lattice point) (n_x, n_y, n_z) in the composite array is calculated from:

$$V_{PA0}(n_x, n_y, n_z) = V_{PA1}(n_x, n_y, n_z) + V_{PA2}(n_x, n_y, n_z) + V_{PA3}(n_x, n_y, n_z),$$

where V_{PA1} is electrode one's solution array (situation 1) and so on.
The voltage adjustment, that is in general much faster than a refining procedure, works as follows: If the voltage at an electrode is changed, *e.g.* U_1 at electrode one, the new potential $V_{\text{PA0, new}}$ at any location in the composite array is calculated with a simple "re-scaling":

$$V_{\text{PA0, new}} = V_{\text{PA0, old}} + \frac{U_{1,new} - U_{1,old}}{U_{1,PA1}} \cdot V_{\text{PA1}}(U_{1,PA1}),$$

where:
$V_{\text{PA0, new}}$ = adjustment point potential (in the composite array PA0),
$V_{\text{PA0, old}}$ = current point potential (in the composite array PA0),
$U_{1,\text{ old}}$ = current electrode voltage,
$U_{1,\text{ new}}$ = new electrode voltage,
$V_{\text{PA1}}(U_{1,PA1})$ = electrode array potential PA1, refined with electrode voltage $U_{1,\text{ PA1}}$,
$U_{1,\text{ PA1}}$ = electrode voltage, the PA1 was refined with.

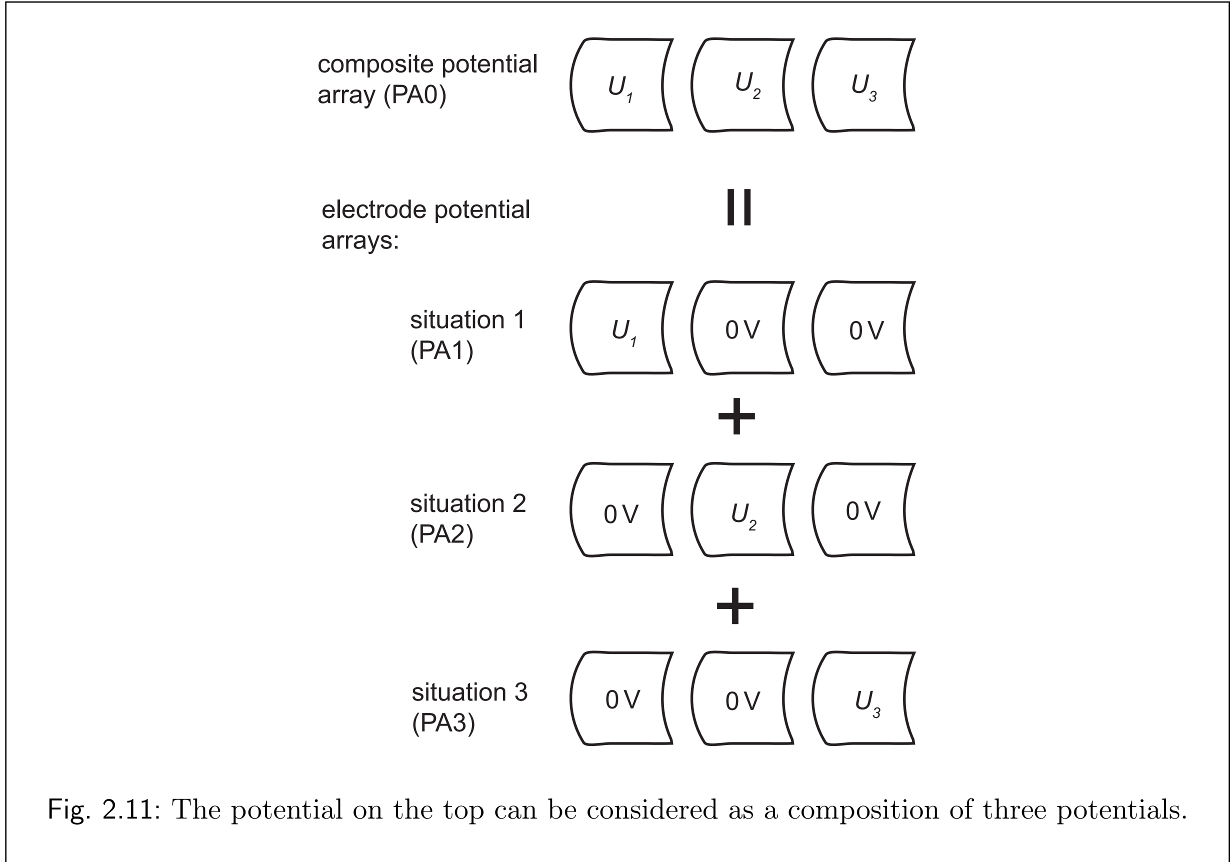

Fig. 2.11: The potential on the top can be considered as a composition of three potentials.

2.3.6 Trajectory calculations in simion

In simion the trajectory of a particle in general is computed by means of a numerical integration (Runge-Kutta integration). The procedure is iterative, *i.e.* from current position, velocity and acceleration the position and velocity in the next time step is calculated, while the current acceleration is estimated depending on current position and velocity of a particle.

There are three independent effects which influence acceleration: electrostatic, magnetic and charge repulsion. Charge repulsion can be switched on or off by the user. In the latter case, interaction between particles is not taken into account.

If we consider a particle in an electrostatic or magnetic potential array, its current acceleration is calculated as follows: From its current position, the potentials of six points (in electrostatic case $V_1..V_6$ and magnetic case $P_1..P_6$) along the coordinate axes, at distance of 0.5 grid units from the current potential array, are calculated by a linear interpolation of the eight nearest neighbor points of each point. From this the forces/accelerations are calculated with the Lorentz equation $m\dot{\vec{v}} = q \cdot (\vec{E} + \vec{v} \times \vec{B})$.

In the case of electric fields:

$$
\begin{aligned}
E_x &= \frac{V_1 - V_2}{1\ grid\ unit}, \\
E_y &= \frac{V_3 - V_4}{1\ grid\ unit}, \\
E_z &= \frac{V_5 - V_6}{1\ grid\ unit},
\end{aligned}
\tag{2.27}
$$

where E_x is the electric field in x-direction, and accordingly E_y and E_z.
Afterward the fields have to be transformed from the potential array coordinates into the workbench coordinates. A workbench is a volume in which the particles' motions evolve, and in which several (up to 200) potential arrays can be rotated and positioned. Now the electrostatic acceleration is calculated fro:

$$
\begin{aligned}
a_x &= \frac{1}{S}\frac{q}{m} \cdot E_x, \\
a_y &= \frac{1}{S}\frac{q}{m} \cdot E_y, \\
a_z &= \frac{1}{S}\frac{q}{m} \cdot E_z,
\end{aligned}
$$

where a_x is the acceleration in x-direction, and accordingly a_y and a_z. $\frac{q}{m}$ is the charge mass ratio and S is the scaling factor (user controllable), since each PA can be scaled in a workbench.

For a magnetic potential array we find:

$$
\begin{aligned}
B_x &= C \cdot \frac{P_1 - P_2}{1\ grid\ unit}, \\
B_y &= C \cdot \frac{P_3 - P_4}{1\ grid\ unit}, \\
B_z &= C \cdot \frac{P_5 - P_6}{1\ grid\ unit},
\end{aligned}
$$

where C is a program internal constant (user controllable, since also magnetic arrays can be scaled in workbenches), and P_n is the magnetic potential. Again the fields have to be transformed from the potential array coordinates into the workbench coordinates. The magnetic acceleration is calculated from:

$$
\begin{aligned}
a_x &= \frac{q}{m}(v_y B_z - v_z B_y), \\
a_y &= \frac{q}{m}(v_z B_x - v_x B_z), \\
a_z &= \frac{q}{m}(v_x B_y - v_y B_x),
\end{aligned}
$$

where B_x is the magnetic field component in x-direction and accordingly B_y and B_z, and v_x is the ion's velocity in workbench axis direction.

3. NEGATIVE ION SOURCE

To make the laser cooling experiment feasible, an adequate production method for $^{192}Os^-$ must be used. One important disadvantage of osmium is its hazardous oxide (OsO_4). Therefore, the formation of osmium oxides must be minimized. Moreover, it must be avoided as much as possible to contaminate surfaces with osmium in the ion generation process. Properties of the element that is to be ionized, as electron affinity and melting point, have to be included in the decision of which ionization process, *i.e.* which ion source, is to be used. Moreover, the beam properties required for the experiment, such as beam current, beam temperature, and beam emittance must be taken into account. To choose a convenient source, the ionization processes must be understood and compared to alternative ion generation methods. It is therefore important to review all different known ionization processes. Hence, basic ionization processes are introduced in this chapter. The main types of negative ion sources can be classified. Some of these main types of sources are also introduced.

3.1 Basic ionization processes

3.1.1 Charge exchange

Beams of negative ions can be generated from positive ion beams by projecting them through a charge exchange cell (donor gas cell or also charge-transfer cell). Charge-transfer cells are vapor cells of low-ionization-potential neutral atoms, in which negative ions are formed out of positive ions through a double-charge exchange process. For alkaline earth vapors, negative ions are formed in a single-step process like:

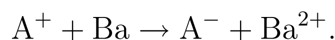

$$A^+ + Ba \rightarrow A^- + Ba^{2+}.$$

If alkali metal vapor is used, the negative ionization is a two-step process:

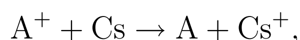

$$A^+ + Cs \rightarrow A + Cs^+,$$

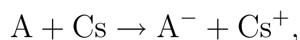

$$A + Cs \rightarrow A^- + Cs^+,$$

which can be summarized to:

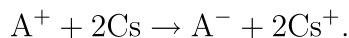

$$A^+ + 2Cs \rightarrow A^- + 2Cs^+.$$

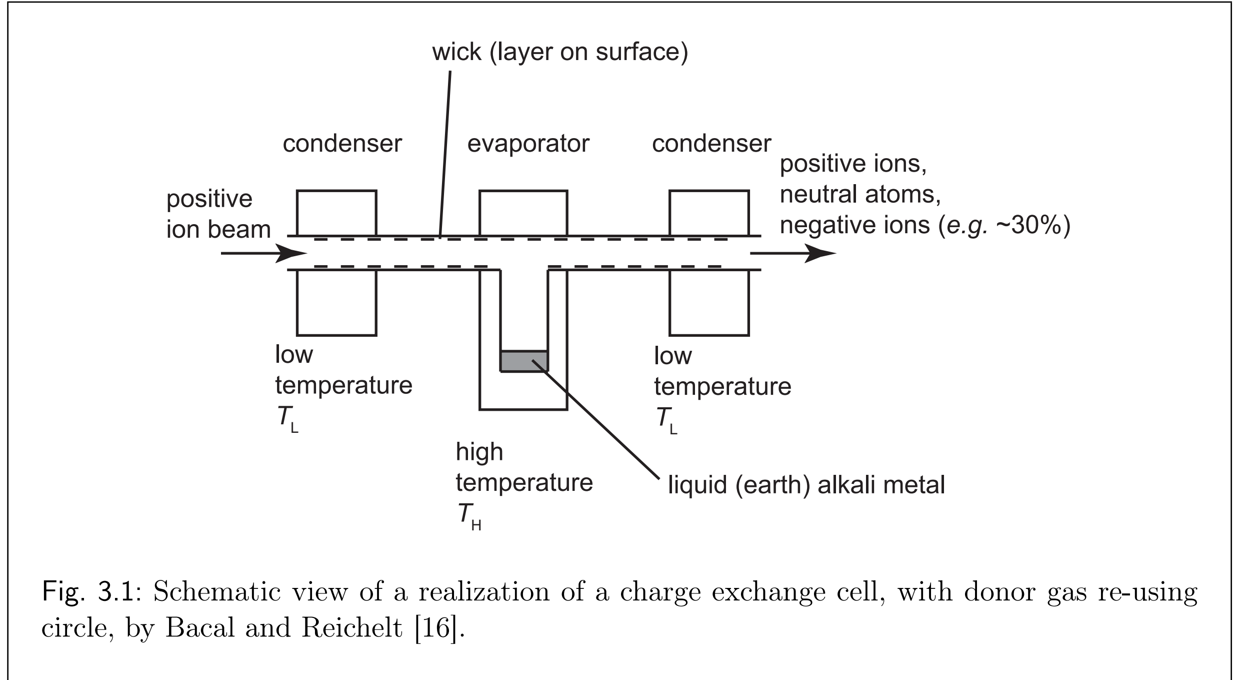

Fig. 3.1: Schematic view of a realization of a charge exchange cell, with donor gas re-using circle, by Bacal and Reichelt [16].

The negative ion yield depends on the electron affinity of the positive ions and the donor gas. In general elements with high electron affinity, such as chlorine, have a larger negative ion yield than elements with low electron affinity. Parameters which influence the ionization yield are the positive ion beam energy and the target thickness (line density) π, which is defined as $\pi := \int_0^l n(x)dx$, where $n(x)$ is the number density of the donor gas particles and l the target length. For a certain positive ion beam energy the negative ion yield can be optimized by tuning the target thickness. This can be done, for example, by changing the temperatures of the charge exchange cell. Figure 3.1 shows a possible realization of a charge exchange cell, as done by Bacal and Reichelt [16]. The temperatures of all parts and surfaces of the charge exchange cell are higher than the melting point of the (earth) alkali metal, used as donor gas. The pressure in the center of the charge exchange canal is on the order of 10^{-3} mbar. This pressure is tunable with the temperature of the evaporator T_H, while this temperature, in combination with the temperature T_L of the condensers, controls the expansion of the charge exchange gas cloud along the canal. The condensed, liquid (earth) alkali metal is returned to the evaporator by capillary action, which is caused by several layers of material on the canal surface, serving as a wick, preventing the liquid metal from "balling up". The (earth) alkali metal in the charge exchange chamber circulates in a closed circle.

Typical maximal negative ion yields of charge exchange cells are between 10% and 40%. For H^+ beams the maximum negative ion yield is achieved at around 200 eV beam energy, while for heavier ions it is usually at higher beam energies in the range of 40 keV (more

detailed information can be found in Ref. [12]).

3.1.2 Extraction from a plasma

The basic mechanism for creating a plasma is a gas discharge. The plasma results from collisions between electrons and the gas atoms inside the plasma source. In plasma sources a gas discharge takes place between a heated cathode, which emits electrons that are accelerated toward an anode. Secondary electrons that emerge from prior collisions can also ionize atoms in further collisions. The basic process of positive ionization is:

$$e^- + \mathrm{A} \rightarrow 2e^- + \mathrm{A}^+. \tag{3.1}$$

In general we find:

$$e^- + \mathrm{A}^{n+} \rightarrow 2e^- + \mathrm{A}^{(n+1)+}. \tag{3.2}$$

The dominant process for the generation of negative ions is electron capture by a rotationally or vibrationally excited molecule with a simultaneous dissociation of the molecule (dissociative attachment of thermal electrons). It can occur according to one of the following reactions:

$$e^- + \mathrm{AB} \rightarrow \mathrm{A}^- + \mathrm{B}, \tag{3.3}$$

$$e^- + \mathrm{A}_2 \rightarrow \mathrm{A}^- + \mathrm{A}, \tag{3.4}$$

$$e^- + \mathrm{AB} \rightarrow \mathrm{A}^- + \mathrm{B}^+ + e^-. \tag{3.5}$$

In plasmas the cross section for forming negative ions is generally a few orders of magnitude lower than that for forming positive ions, since the capture of an electron to a neutral atom requires the relative kinetic energy of atom or molecule and electron to be at most the atom's or molecule's electron affinity, which is in general rather small ($\sim$1 eV). Furthermore, the loss rate of an electron from negative ions, through collisions, is in general rather high in a plasma, since negative ions have rather large radii and therefore large geometrical cross-sections and low binding energies [electron affinity ($\sim$1 eV)]. That is why the negative ion yield is very low, in comparison to positive ones.

Collisions with electrons of higher energy than thermal electrons can be used to excite molecules and to maximize the negative ion yield of the processes of Eqs. (3.3)..(3.5), since the dissociative attachment of thermal electrons has a high cross-section for highly excited molecules.

Another process is three-body collision, either in a two-component gas (the atoms or molecules to be ionized and an inert gas), or atoms formed in the prior processes, *i.e.* Eq. 3.3 with afterward neutralization of A^-:

$$e^- + \mathrm{A} + \mathrm{B} \rightarrow \mathrm{A}^- + \mathrm{B}.$$

Surface ionization (Sec. 3.1.3) can be used to increase the number of negative ions in a plasma.

By choosing the sign of the extraction electrode voltage, either positive or negative ions can be extracted. However, when negative ions are extracted from a plasma, electrons are also obtained, since they have equal charge. Electrons can be separated from negative ions, for example, by using a transverse magnetic field in the vicinity of the extraction.

There are very efficient HF- , Penning- , and Duoplasmatron sources for H^- beams, which are based on their positive ion counterparts. Further information on ion plasma sources can be found in Refs. [13, 17, 12].

3.1.3 Surface ionization

Surface ionization is a process that works in a similar way for positive and negative ions. An atom or molecule ejected from a surface can capture an electron from the surface or lose an electron to it. Neglecting statistical weights, according to the Langmuir-Saha equation [13, 18], the ratio of the number of positively ionized (n^+) and neutral (n_n) atoms, emitted from a surface is given by:

$$\frac{n^+}{n_\mathrm{n}} \propto exp\left[\frac{\varphi_\mathrm{S} - I_\mathrm{p}}{k_\mathrm{B}T}\right], \tag{3.6}$$

where φ_S is the effective work function of the surface, I_p the ionization potential of the atom or molecule and T the temperature of the surface.

From Eq. (3.6) we see that the positive ionization yield is maximal for small ionization potentials, high effective work functions and high temperatures of the ionizing surface. The ionization potential of many elements is between 5 eV and 25 eV. It is low for alkali metals and high for noble gases. For three alkali metals (K, Rb, Cs), it was measured to be smaller than 4.5 eV. The effective work function of clean elemental surfaces mostly lies between 3.5 eV and 4.5 eV.

With small modifications, Eq. (3.6) can also be applied to negative surface ionization. For this purpose, the ionization potential I_p is substituted by the electron affinity E_A, and the sign of the exponent is inverted [22]. We find:

$$\frac{n^-}{n_\mathrm{n}} \propto exp\left[-\frac{\varphi_\mathrm{S} - E_\mathrm{A}}{k_\mathrm{B}T}\right]. \tag{3.7}$$

Electron affinities of many elements are between 1 and 2 eV (see Fig. 2.1). The negative surface ionization yield is maximal for low work functions and high electron affinities.

The effective work function of many plain surfaces lies between 3 and 6 eV, while it is usually rather high for heavy metals (*e.g.* rhenium $\sim$ 5.0 eV), and the lowest for cesium,

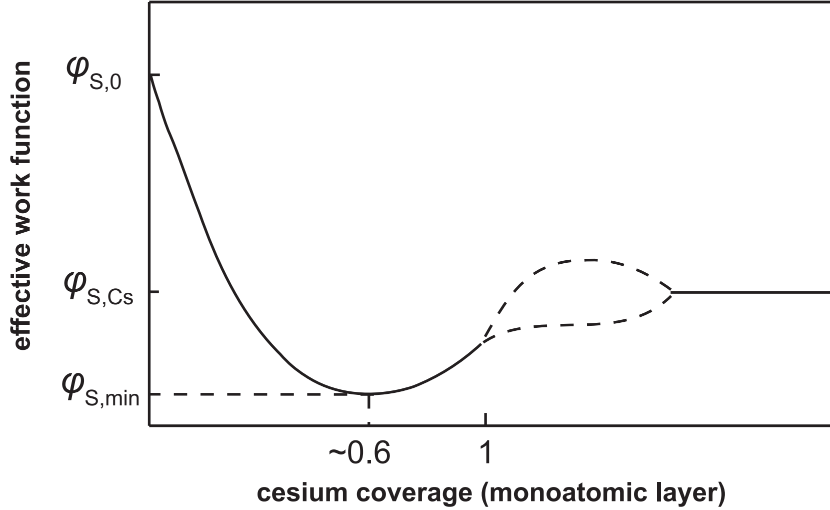

Fig. 3.2: Typical behavior (schematic) of the effective work function of a surface, as a function of the cesium coverage. (Adapted from Ref. [12].)

with ≈ 1.81 eV. The effective work function of metals and semiconductors [19] decreases if the surfaces are covered with a cesium layer. It is usually even smaller than the work function of the surface of pure cesium. Moreover, it was found that there is an optimal cesium coverage, less than one monoatomic layer (average layer thickness around ∼ 0.6 times the thickness of a monoatomic layer), for which the effective work function of the surface is minimal (Fig. 3.2). With an optimal cesium coverage, the work function decreases to a minimum value $\varphi_{\mathrm{S,min}}$ of mostly between 1.37 and 1.76 eV. With a further increasing coverage, until a monoatomic layer covers the surface, the work function increases to a value between 1.56 and 2.15 eV.

The degree of cesium coverage of a surface depends very much on the temperature and the properties of the material to be covered. For metals, a monoatomic cesium layer is built at temperatures reaching from room temperature to several hundred degrees Celsius. However, a cesium multilayer is not built above the melting point of cesium (∼ 28.5 °C), and usually not even above room temperature, regardless of the covered material. If the surface is cold enough, a cesium multilayer can appear, and the effective work function converges to that of pure cesium.

Alton found a semi-empirical equation which describes the minimum effective work function of a surface, covered by an elemental layer [20]:

$$\varphi_{\mathrm{S,min}} = 0.62 \cdot (I_{\mathrm{p}} + E_{\mathrm{A}}) - 0.24 \cdot \varphi_{\mathrm{S,0}}, \tag{3.8}$$

where I_{p} is the ionization potential, E_{A} the electron affinity of the element covering the

surface, and $\varphi_{\mathrm{S},0}$ the effective work function of the uncovered surface. In the case of cesium, the sum $(I_{\mathrm{p}} + E_{\mathrm{A}}) \approx 4.35$ eV is the smallest of all elements.

3.2 Types of negative ion sources

All negative ion sources, both commercially available and custom-built models, are based upon the ionization processes presented above. In the following, the most frequently used negative ion sources are introduced and the ion source type chosen for our experimental setup is discussed in detail.

3.2.1 Plasma sources with volume production

As already mentioned above, the percentage of negative ions in typical plasmas is rather low. In order to increase the cross section of negative ion formation, *i.e.* the dissociative electron attachment cross section of hydrogen molecules, the plasma is divided into two parts, by means of a magnetic field. Because of their small mass, compared to atoms or molecules, the electron's motion is much more sensitive to magnetic fields. In one part of the plasma, hydrogen molecules are highly excited by collisions with high-energy electrons ("high-temperature electrons"), while in the other part, negative ion formation takes place mainly through collisions of molecules in high states with electrons of low energy, around ~ 1 eV ("low-temperature electrons").

The direct generation of negative ions in a plasma, through collisions between electrons and highly excited molecules, is also known as "volume production". Several H^- sources have been developed, based on volume production. In Fig. 3.3, a multicusp plasma chamber of a volume production H^- source is shown. The filaments generate a discharge between anode (chamber) and cathode (filaments). Magnetic fields (permanent magnets) are applied to the multicusp ion source (multicusp plasma chamber), in order to realize a magnetic filter and to keep the plasma away from the walls. The magnetic filter divides the plasma into a region with high energetic electrons, where H molecules become highly excited, and in a second region with low-energy electrons, where negative H ions are produced (extraction region). A second magnetic filter supresses electrons from being extracted. This source delivered a H^- beam current of 44 mA. With cesium vapor added into the plasma chamber, the H^- beam current was increased to 86 mA (see Ref. [12]).

3.2.2 Plasma sources with surface ionization

In the development of plasma sources for negative ion beams, it was found that the negative ion production in plasmas is increased in the presence of electrodes, especially those with low work function. Many negative ion plasma sources based on surface ionization have been

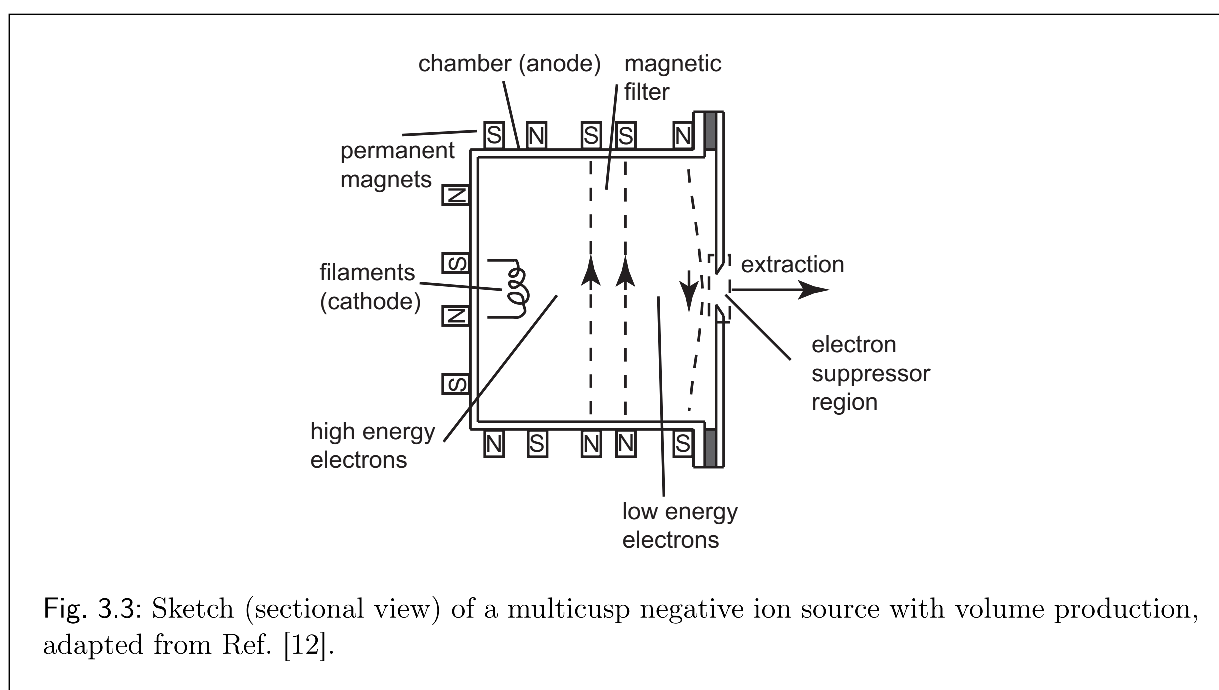

Fig. 3.3: Sketch (sectional view) of a multicusp negative ion source with volume production, adapted from Ref. [12].

developed; some are variations of originally positive ion sources, such as duoplasmatron and Penning sources. The principle is that a mostly cesiated surface is positioned close to, or even within, the plasma. Plasma particles reaching the surface and being bound to it can be (re-)ionized while being re-emitted from the surface ("surface ionization" Sec. 3.1.3). The cesiated electrode (converter) can be one of the electrodes causing the discharge to generate the plasma, or it can be an additional electrode. In the latter case, the negative ion production can be controlled with a voltage between plasma (chamber and discharge electrodes) and ionization electrode. The energy of ions reaching the convertor can be controlled with the converter voltage. Figure 3.4 shows an overview of a multicusp type negative ion source, in which a converter is placed to negatively ionize particles of the plasma in its vicinity.

The converter is a cesiated Mo surface, and the whole chamber acts as an anode. The plasma is generated through collisions between gas atoms and electrons emitted from the hot filaments and accelerated due to a voltage (90 V) between filaments and chamber. Permanent magnets are mounted around the chamber in order to keep the electrons and the plasma away from the chamber walls. The negative ion generation on the converter can be controlled with a negative bias voltage, on the converter. During the operation the converter is permanently exposed to neutral cesium vapor. Negative ions, which are produced on the converter, are repulsed from it and, because of its circular shape, focused onto the exit aperture. The source delivered a H^- current of more than 1 A (see Ref. [12]).

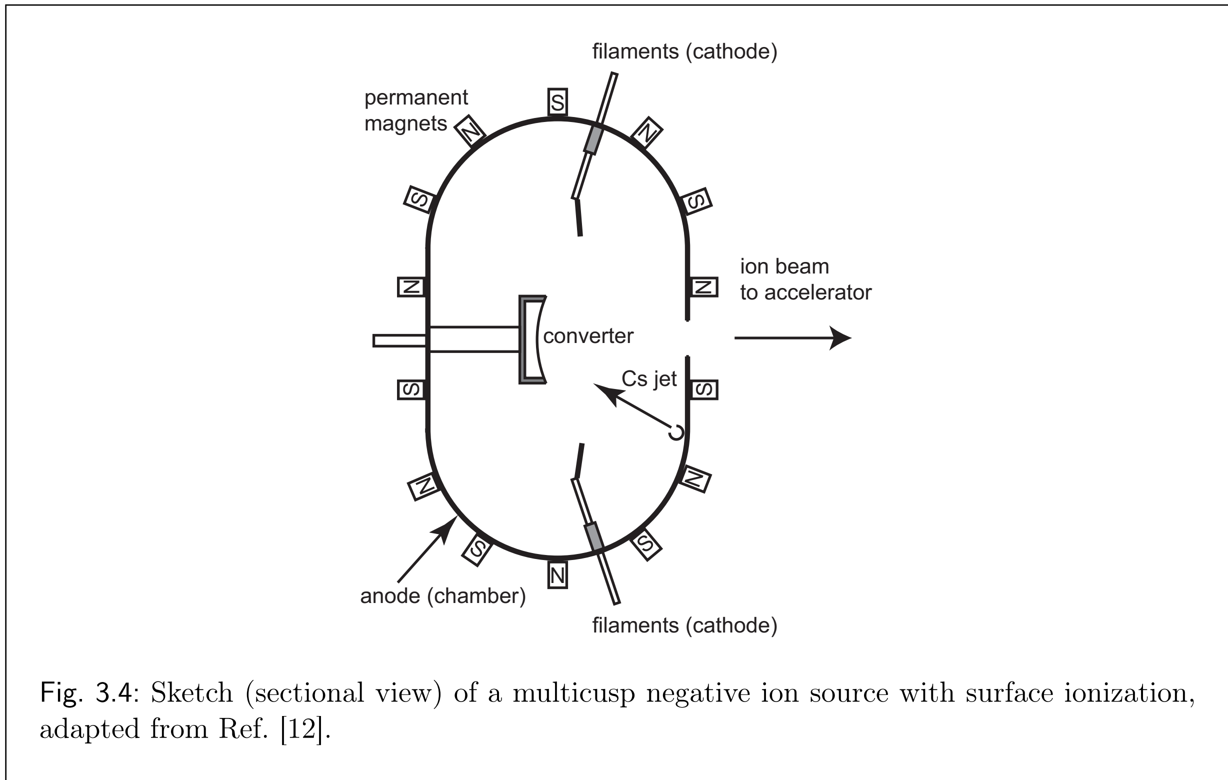

Fig. 3.4: Sketch (sectional view) of a multicusp negative ion source with surface ionization, adapted from Ref. [12].

3.2.3 Sputter type negative ion sources

Various types of the sources already presented were often designed to generate H^- beams. Generally speaking, one main disadvantage of the negative ion sources presented above is that the material, *i.e.* the element or molecule that is to be negatively ionized, is required to be in the form of a vapor or gas. Sputter sources overcome this problem, since they allow the direct transformation of a solid material into a negative ion beam. Heavier elements, with rather high melting point, such as many heavy metals, can be transformed into negative ion beams with sputter sources. Figure 3.5 gives a schematic overview of the working principle of negative ion production in sputter sources. A target contains the desired material X (“sample”) for negative ion formation. On the one hand, the sample is exposed to neutral cesium vapor in order to form a thin cesium layer on the target surface through condensation. In this way the negative ion yield of secondary emitted particles is increased (see Secs. 3.1.3). On the other hand, the target is sputtered (bombarded) with a positive ion beam to generate secondary particle emission. As a positive ion beam Xe^+ or the Cs^+ ions themselves can be used, for example. The positive ion beam energy is usually a few keV but can vary a lot ($\sim$ 0.1..50 keV), depending on the target material,the desired beam current and operation time (target wastage). The different kinds of negative ion sputter sources mainly differ in the way the positive ions are generated.

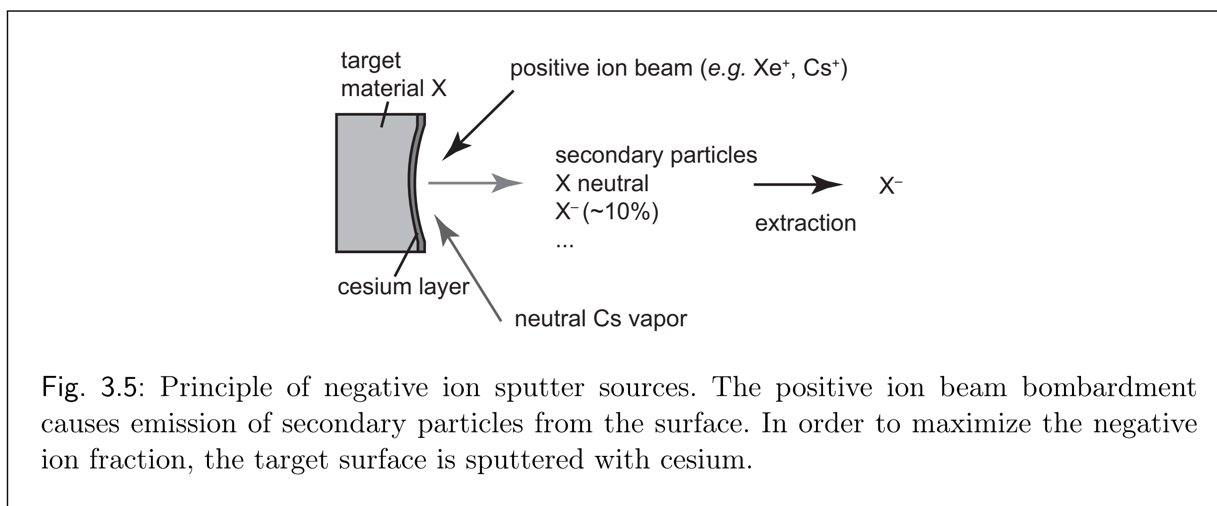

Fig. 3.5: Principle of negative ion sputter sources. The positive ion beam bombardment causes emission of secondary particles from the surface. In order to maximize the negative ion fraction, the target surface is sputtered with cesium.

Plasma sputter type

In plasma sputter type negative ion sources the positive ion beam (Xe^+) for sputtering the target is generated in a plasma close to the target. Since the target is negatively biased, positive ions are accelerated toward the target. These plasma sputter sources mainly differ in the way the plasma is produced. The plasma generation is mostly adapted from usual positive ion sources. One example is the ANIS (Aarhus Negative Ion Source), in which a PIG-discharge ("Penning Ion Gauge") in a xenon gas generates the plasma, others are the RF and microwave-discharge plasma sputter types, where the plasmas are generated just like in usual positive ion beam RF and microwave plasma sources (see Ref. [12] p.305 for an overview). In Fig. 3.6 a sketch of an ANIS source is shown. Electrons are emitted from the filament and repulsed from the cathodes. A magnetic field drives the electrons to move on a helix like trajectory in order to increase the effective path length, and to increase the effective number of collisions between electrons and xenon atoms. The Cs vapor condenses on the target surface. Xe^+ and Cs^+ are accelerated to the target, since it is negatively biased. Their energy was tuned between 1 and 2 keV, while the current was measured to be about 10 mA. Secondary negative ions are repulsed from the target surface and focused to the exit aperture, since the target surface has a spherical shape. Diverse negative ion beams were produced with this source and beam currents ranged from 1 µA (Li^-) to 80 µA (Au^-).

Beam sputter type

In other types of negative ion sputter sources, the positive ion beam for the target bombardment is supplied by an external positive ion source or by a filament with high work function, in order to positively ionize gas atoms at its surface. Some of these sources are the

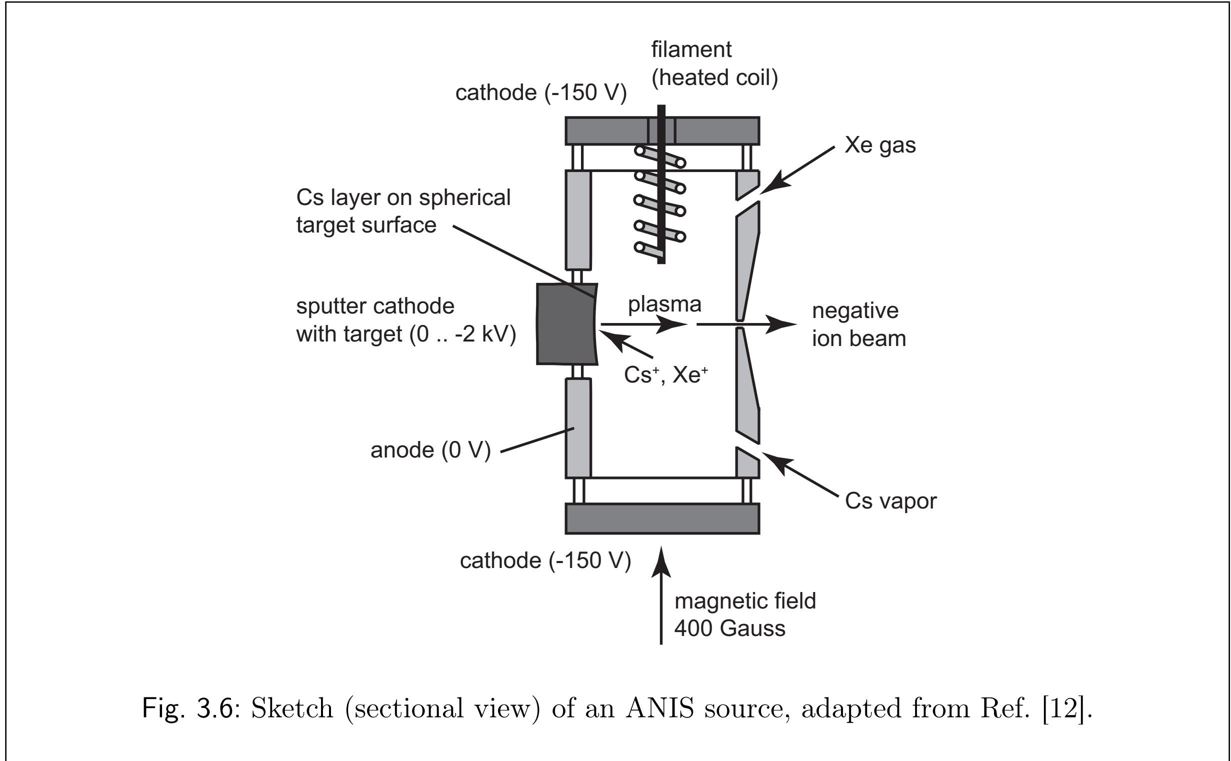

Fig. 3.6: Sketch (sectional view) of an ANIS source, adapted from Ref. [12].

UNIS (universal negative ion source) developed by Middleton [21], the NIABNIS (neutral and ionized alkaline metal bombardment negative ion source) developed by Ishikawa *et al.* [12], and the VNIS (versatile negative ion source) developed by Middleton [22] as well. The VNIS is also known as "high intensity Middleton type source". The source used in our experimental setup is of the VNIS Middleton type and is introduced in the following.

3.2.4 Negative ion source in our experiment

It is not feasible to transform osmium into the form of gas or vapor, because it has a very high melting point of about 3000°C, and in addition osmium is hazardous. As already mentioned, in sputter sources the sample from which the ions are generated is in solid form.

A variation of a Middleton-type ion source was already operated at the MPI-K, *i.e.* in the vicinity of our experimental setup, such that we were able to benefit from the experience of the people who routinely operate it. Additional advantages are the rather low costs compared to commercially available sources and that the MISS is of course small enough to match into our setup. For these reasons it was decided to design such a source, make technical drawings of it and produce it, for our experimental setup.

This ion source used in our setup is a beam sputter type negative ion source and more specifically a negative ion source of the Middleton VNIS type (versatile negative

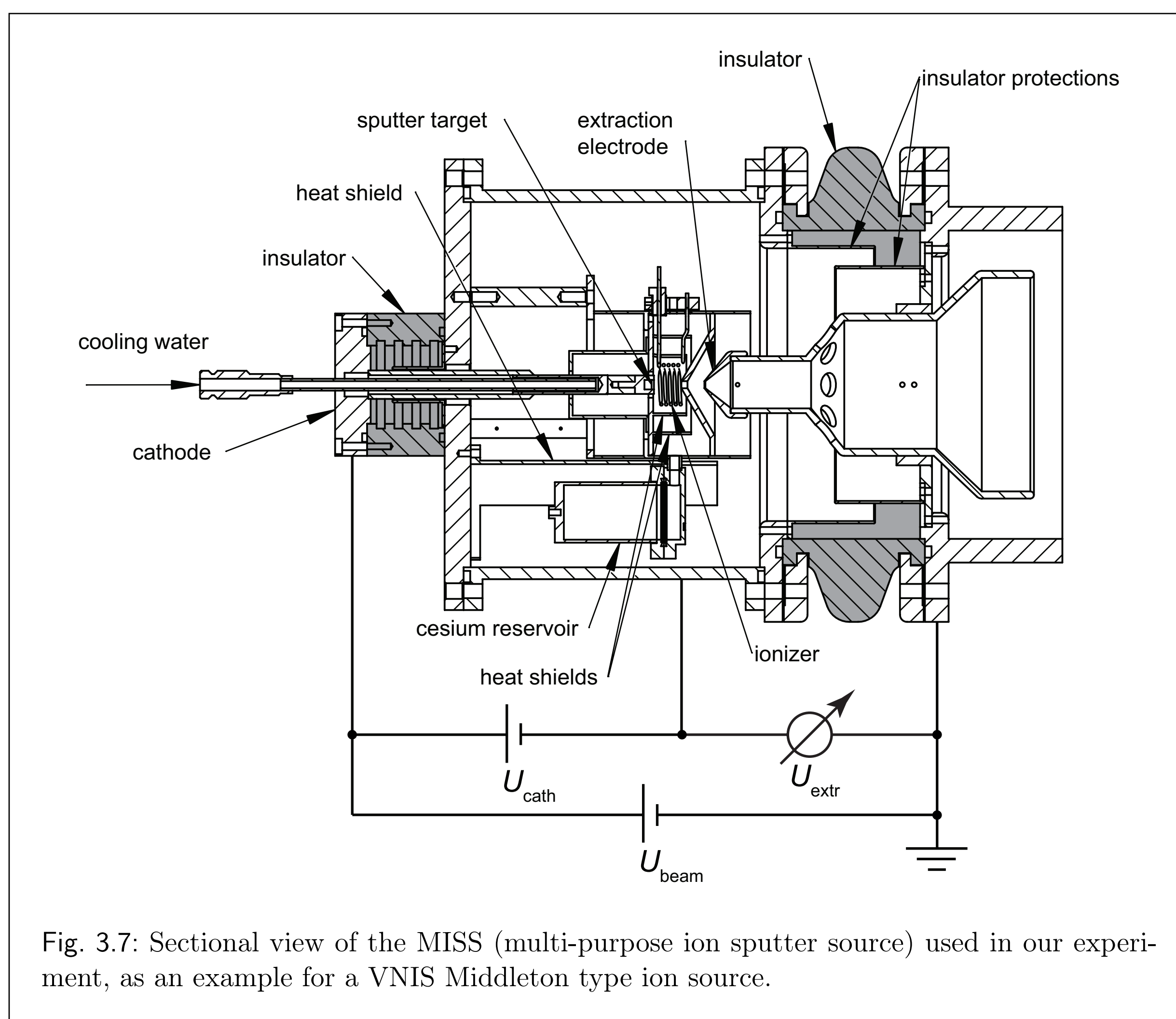

Fig. 3.7: Sectional view of the MISS (multi-purpose ion sputter source) used in our experiment, as an example for a VNIS Middleton type ion source.

ion source). It is based on a design developed at the Max Planck Institute for Nuclear Physics in the 1980s for use with the tandem accelerator and test storage ring (TSR). Its design has similarity to the design of source VII from Ref. [22]. Figure 3.7 shows a sectional view. While the source is operating, there is a permanent flux of neutral cesium vapor from the cesium reservoir to the inner chamber, where the sputter target and the ionizer are situated. Some of the cesium atoms are positively ionized on the ionizer surface. Cesium was chosen as the positive ion for driving the sputter process in Middleton type sources, since in addition to reducing the sputter surface work function it has the advantage of having a high positive ionization yield because of its low ionization potential (surface positive ionization see Sec. 3.1.3). Furthermore, in Middleton type sources ionizers are made of heavy metals with high effective work function (*e.g.* rhenium $\sim$ 5.0 eV, tantalum $\sim$ 4.25 eV, tungsten $\sim$ 4.5 eV) and high melting points in order to reach high temperatures

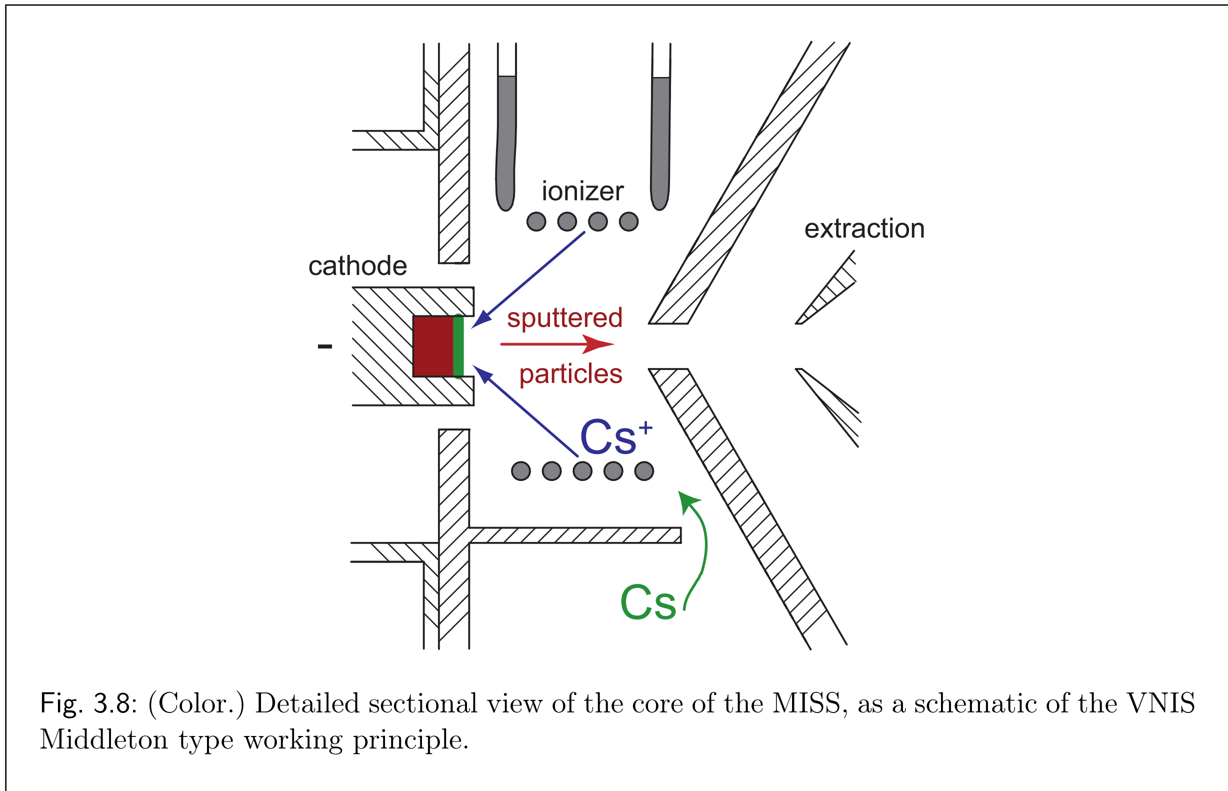

Fig. 3.8: (Color.) Detailed sectional view of the core of the MISS, as a schematic of the VNIS Middleton type working principle.

of more than 1000°C. Cs^+ ions are accelerated toward the sputter target with an electric field generated by a voltage between sputter target (cathode) and ionizer (which is kept at the same potential as the surrounding chamber).

When the cesium ions impact the surface of the sputter target material with sufficient energy, secondary particles of the material can be emitted. Usually a portion ($\sim$ 10%) of these particles is negatively ionized and therefore repulsed from the surface (Sec. 3.2.3). Negative ions passing through the hole in the inner chamber are further accelerated by the extraction potential and travel toward the ion optical system. Figure 3.8 shows a zoomed view of this working principle. So-called poisoning of the ionizer surface by (neutral) sputtered particles and cesium condensation decreases the cesium ionization rate, since it reduces the work function of the ionizer surface. To reduce condensation, and maintain the cesium ionization rate at a high level, the ionizer is heated by an electrical current of about 30 A. For high temperatures the surface positive ionization rate is maximal, as explained in Sec. 3.1.3. The ionizer consists of a tungsten/rhenium wire (95% W and 5% Rh), shaped like a helix. The working temperature of the ionizer in the MISS has not been measured, but is estimated to be higher than 1000°C. To protect the sputter target material from melting and to increase cesium condensation on the sputter target material surface, the sputter target is cooled by cooling water such that its temperature is lower than that of

the surroundings.

Negative ions and electrons are both repulsed from the target. An even larger number of electrons is emitted from the ionizer, since it is very hot. The extraction potential is attractive to both negative ions and electrons. In order to suppress electrons from reaching the extraction electrode, a weak magnetic field can be applied. This can be realized in setting up permanent magnets around the vacuum chamber of the source. In source VII from Ref. [22] a magnetic field of about 100 G was created in the region between target (cathode) and exit aperture, which reduced the current of the extraction power supply by several mA.

There are two important features of this type of source that should be mentioned here, both of which are very desirable. The first is that the Cs^+ beam is electrostatically focused onto one small area on the target surface. A focused Cs^+ beam decreases the emittance of the sputtered beam, since it then originates from a smaller area, and in this way improves the negative ion beam quality. The second feature is that the extraction electrical field and the cathode electrical field are almost decoupled. That means that the extraction electrical field has almost no influence on the sputter process, since it hardly reaches into the inner chamber, as shown in Fig. 3.10. The sputter process, and therefore the beam current are well tunable with the cathode voltage, thus allowing to tune the beam current independently from the beam energy. Fig. 3.9 shows the potential "seen" by the positive cesium ions, which drives the sputter process. One possible realization is shown in Fig. 3.7, where the beam energy is determined by U_{beam} and so is tunable with one power supply. The beam current is determined by U_{cath}, that is tunable with another power supply.

In the following, I will summarize the operation parameters for ion source operation. The sputter rate depends on the sputter energy. The cathode voltage determines the sputter energy and is therefore the main parameter to tune the negative ion beam current in a short time (temperature based parameters change much more slowly). According to Middleton [22], the cesium current hardly depends on the rate of flow of neutral cesium vapor, but of course on the cesium ionization rate. The cesium ionization rate is tunable with the tungsten wire current, since it has a strong influence on the ionizer temperature. The rate of flow of neutral cesium vapor depends on the cesium reservoir temperature. In our case this temperature is controlled with a compressed air cooling helix and an electrical heating coil both enclosing the Cs-reservoir (not shown in the previous figures). We then tune this temperature with the rate of flow of the compressed air (in general only done once; after a convenient value was found it is fixed) and the heating current. The temperature is then maintained with a regulator circuit, controlling the heating current.

Figure 3.11 shows an overview of all relevant parameters and their respective dependencies. We only use the parameters in the dark boxes to tune the negative ion current generated by the MISS. Of course, the target temperature also depends on the ionizer current, since the ionizer heats its surrounding too. However, the target temperature was not used in the measurements described below for any tuning, and we can consider it as a

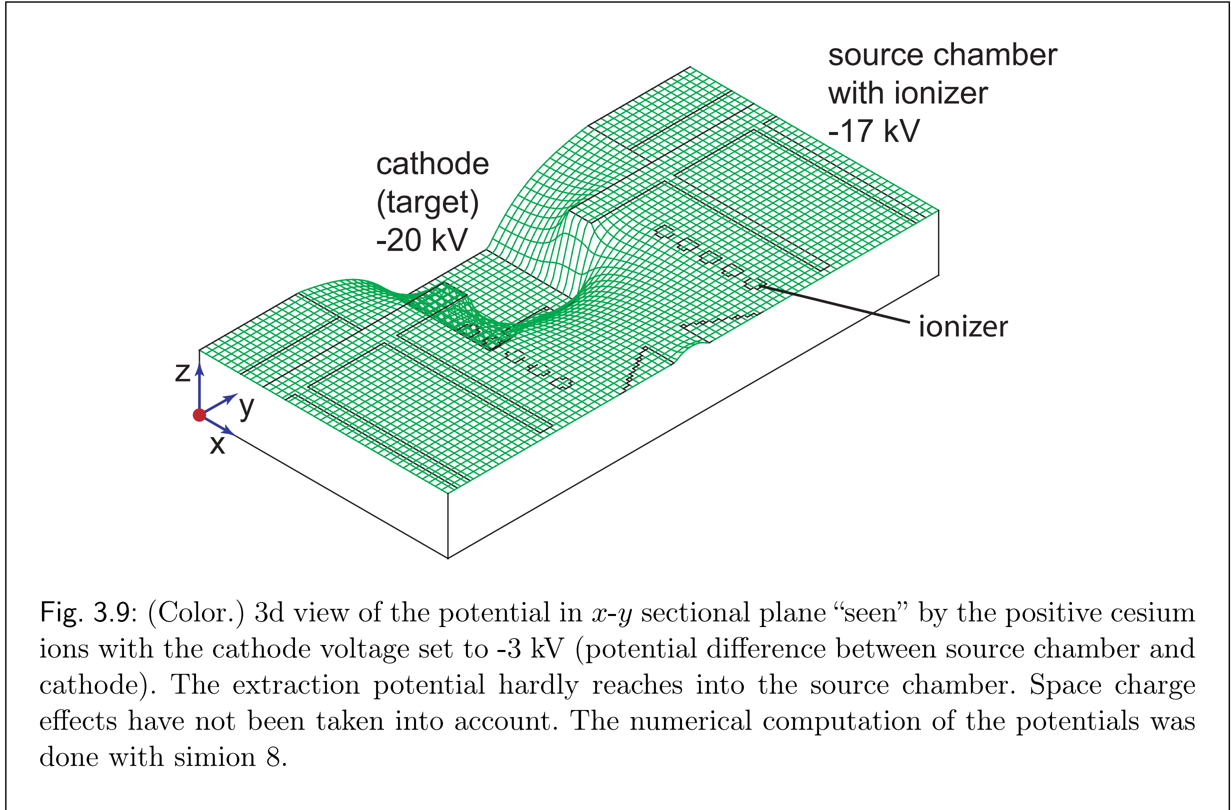

Fig. 3.9: (Color.) 3d view of the potential in x-y sectional plane "seen" by the positive cesium ions with the cathode voltage set to -3 kV (potential difference between source chamber and cathode). The extraction potential hardly reaches into the source chamber. Space charge effects have not been taken into account. The numerical computation of the potentials was done with simion 8.

constant value, since we usually waited until an approximately thermodynamic equilibrium situation was reached in the MISS before generating a beam. The ionizer current is usually fixed to an empirical value depending on the target material.

3.3 Experimental results

The goal of the measurements reported here was to test and characterize the ion source, as well as to produce a reference for future source operations and experiments. Since the construction of our ion source was completed before the beam line components, the beam current measurements described here were performed at an existing setup in the accelerator hall at the MPI-K. The setup consisted of the MISS and its einzel lens, a second einzel lens, a 35° bending magnet for mass separation, a pre-accelerator, and a Faraday cup behind it. The beam current measurement is based on a direct measurement of the electrical current, measured with a Faraday cup and a micro ampere meter.

Iron sulfide was used as target material. A scan of the bending magnet current, and hence the magnetic field of the bending magnet, was performed. Afterward the current was held at a constant value to maintain an almost pure $^{32}S^{-}$ ion beam (the resolution

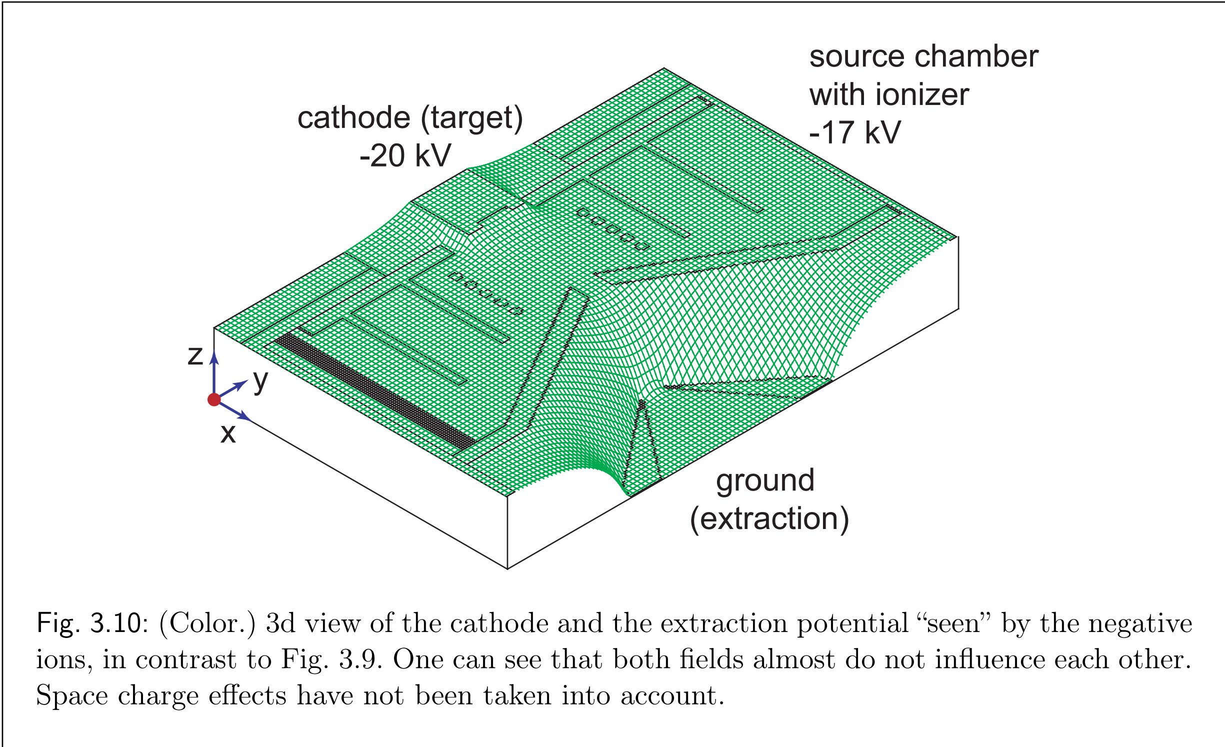

Fig. 3.10: (Color.) 3d view of the cathode and the extraction potential "seen" by the negative ions, in contrast to Fig. 3.9. One can see that both fields almost do not influence each other. Space charge effects have not been taken into account.

was not high enough to ensure complete isotope separation) behind the bending magnet. Figure 3.12 shows the result of the current scan of the bending magnet coils.

Figures. 3.13 and 3.14 show the $^{32}S^{-}$ beam current as a function of the cathode voltage, with a beam voltage U_{beam} fixed to 20 kV, *i.e.* a beam energy of 20 keV. The maximum recommended value for the cathode voltage to operate the MISS reliably in DC mode is 3 kV. This is an empirical value. For higher cathode voltages usually discharges occurred [23].

During the first three beam current measurements (Fig. 3.13), the cathode voltage was not allowed to exceed 3 kV. One night after the source was flanged and evacuated for the first time, the heating procedure (see Sec. B.2.1) was started. In this routine procedure, the ionizer current is switched on to heat the MISS, such that surfaces inside the MISS begin to outgas. The first measurement was started three hours, the second five hours, and the third six hours after the beginning of the outgassing procedure. During all measurements, the ionizer current was set to 26 A. Since the reservoir temperature fluctuated somewhat due to the regulation circuit, I started every series of measurement when the cesium temperature seemed to be the most stable. That is why the series of measurements were performed at different cesium reservoir temperatures. As apparent from the plots, the beam current increases with time, which was already observed with other MISS sources [23]. Initially after evacuation, the source must be heated up and outgas for several hours until the beam current reaches a maximum.

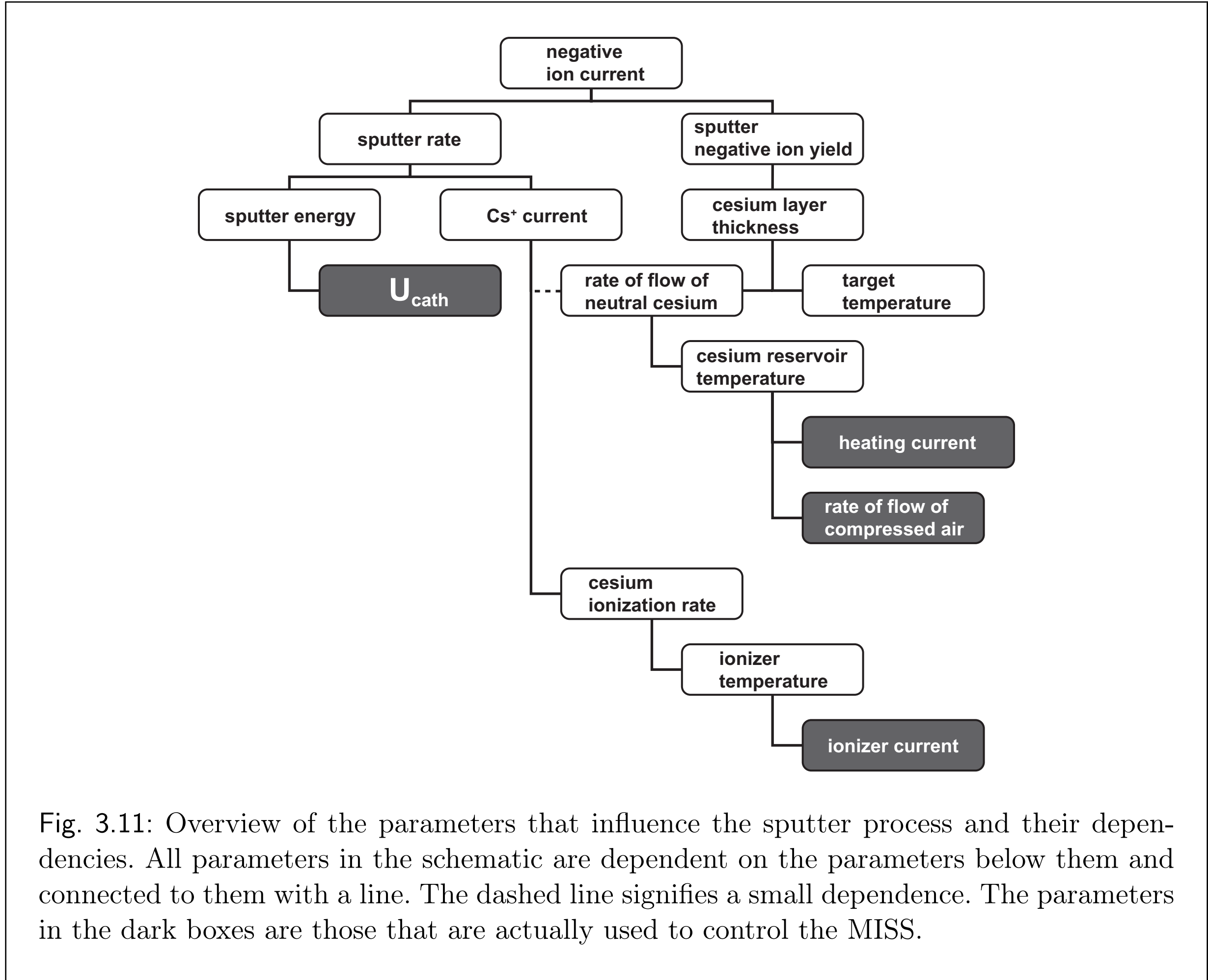

Fig. 3.11: Overview of the parameters that influence the sputter process and their dependencies. All parameters in the schematic are dependent on the parameters below them and connected to them with a line. The dashed line signifies a small dependence. The parameters in the dark boxes are those that are actually used to control the MISS.

In the next measurements (Fig. 3.14), I exceeded the recommended maximum cathode voltage in order to find a maximum in the beam current. But before a maximum was reached, discharges occured at 3.7 kV. Thus it was not possible to further increase the cathode voltage without risking to damage the source. It is apparent from the plots that the cesium reservoir temperature fluctuated a lot. Since the original MISS was designed for reliable and stable beams and long operation times, but not necessarily for high beam currents, it was not deemed necessary to reach high cathode voltages. This explains why discharges occurred at 3.7 kV cathode voltage.

The goal of the next series of measurement was to find out if the MISS is able to generate a sufficient beam current with lower beam voltages U_{beam}, in the 5 kV range. For this purpose, the cathode voltage was fixed at 3 kV and the beam current was measured as a function of U_{beam} (Fig. 3.15). The fact that the beam energy changed with U_{beam}, made these measurements particularly challenging, as the different parts of the ion optical setup

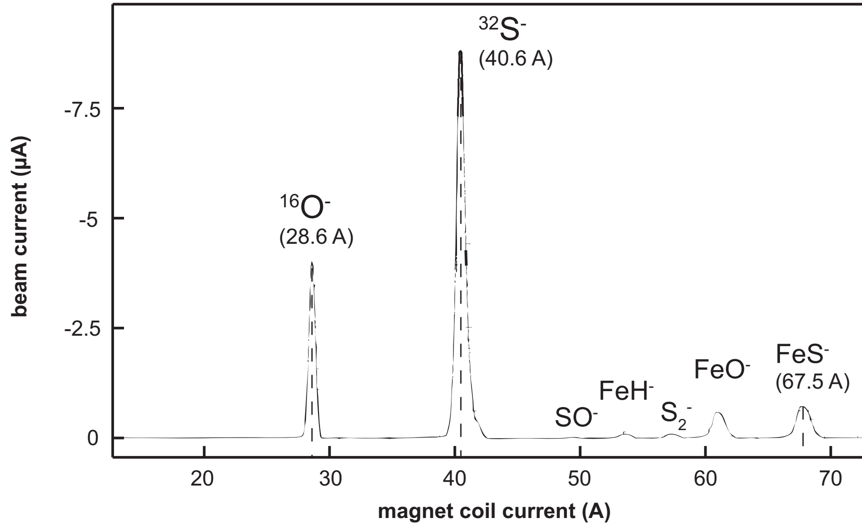

Fig. 3.12: Beam current as a function of the current of the bending magnet coils. The target material is iron sulfide with naturally abundant iron (91.7% ^{56}Fe) and sulfur (95% ^{32}S).

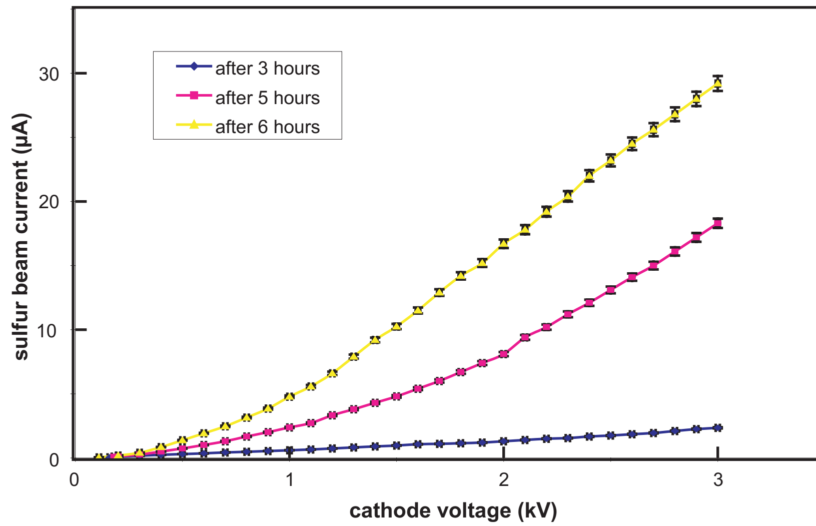

Fig. 3.13: (Color.) ^{32}S$^-$ beam current as a function of cathode voltage. The first series of measurement was accomplished three hours after starting the outgassing procedure ($t = 3$ h) [$I_{\text{ionizer}} = 26$ A, $T_{\text{Cs}} = 82.5(5)$°C]. For the second series of measurement, it was $t = 5$ h, $I_{\text{ionizer}} = 25.4$ A, $T_{\text{Cs}} = 65.0(2)$°C. Furthermore, for the third series of measurement, the values were $t = 6$ h, $I_{\text{ionizer}} = 25.6$ A, $T_{\text{Cs}} = 88(1)$°C.

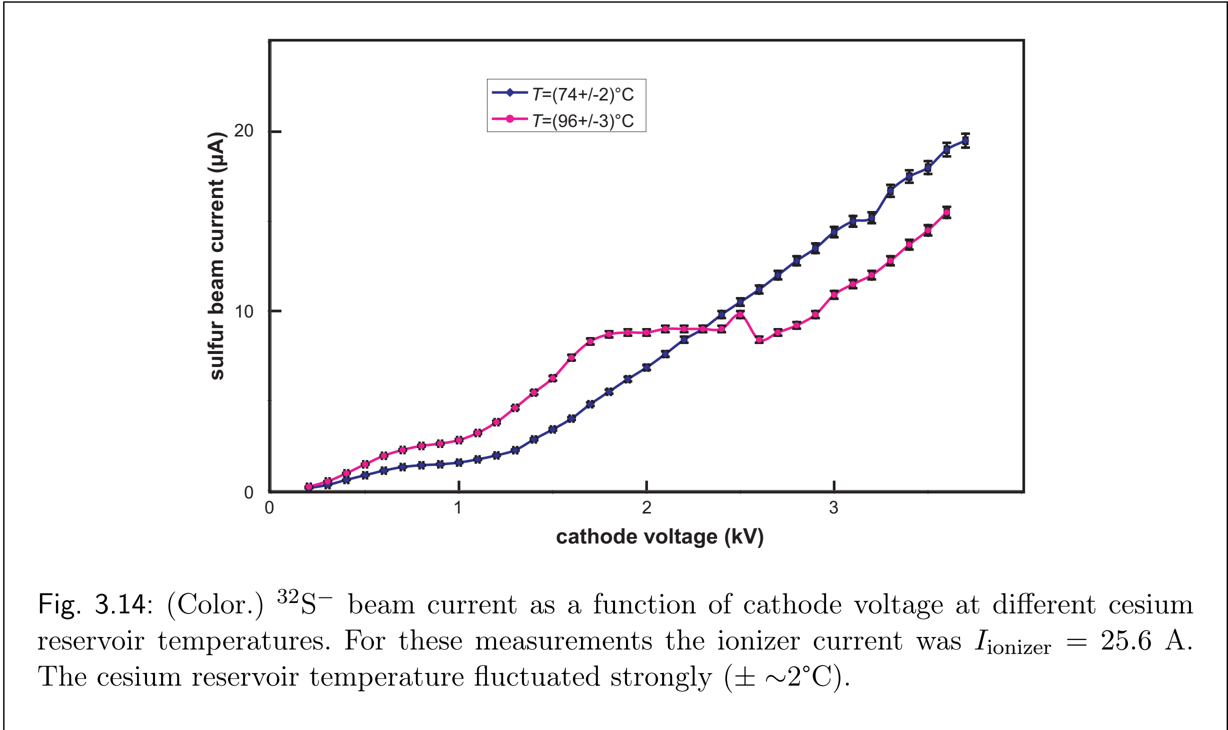

Fig. 3.14: (Color.) $^{32}S^-$ beam current as a function of cathode voltage at different cesium reservoir temperatures. For these measurements the ionizer current was $I_{\text{ionizer}} = 25.6$ A. The cesium reservoir temperature fluctuated strongly ($\pm \sim 2$°C).

had to be re-adjusted for every measured value.

The error bars in all graphs in the Figs. 3.13, 3.14 and 3.15 result from the current measurement uncertainty of the microamperemeter. Errors resulting from temperature fluctuations are not included in these error bars. Furthermore, an additional source of errors in the graph in Fig. 3.15 is the uncertainty in the maximization of the beam transmission through the ion optical system, since many parameters (electrode voltages and the bending magnet current) have to be changed. To avoid fluctuations of the cesium reservoir temperature the temperature regulation might be optimized further by finding more optimal values for the regulator circuit and the rate of cooling compressed air. To ensure a constant rate of flow of neutral cesium vapor, it should be waited until a thermal equilibrium and a dynamic equilibrium of the rate of flow of vapor is approximately reached after the temperature was changed.

From the measurements with U_{beam} at about 5 kV it can be concluded that the MISS generates sufficient beam currents for the planned Os^- laser cooling experiment. A worst case estimation, taking into account the projected beam line for the setup, yields a 200 nA beam current of $^{192}Os^-$ for a cathode voltage of 3 kV.

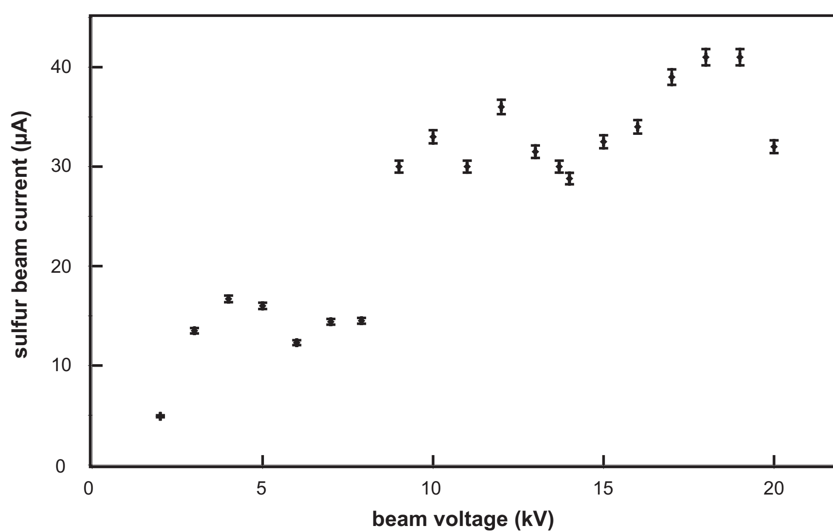

Fig. 3.15: To determine whether the MISS is also adequate for the generation of negative ion beams for beam energies E_{beam} in the 5 keV range, the cathode voltage was fixed at 3 kV, and the beam current was measured for different beam voltages.

4. MASS SEPARATION AND ION-OPTICAL ELEMENTS

For a first test on the laser cooling of $^{192}Os^-$ in a Penning trap, the trap should contain only $^{192}Os^-$ with as little contaminations of other ions as possible. Undesired ions would be sympathetically cooled with $^{192}Os^-$, thus influencing cooling rates and possibly the final temperature. Hence, it is important to generate an $^{192}Os^-$ ion beam as pure as possible. Ion beams generated in the MISS contain various molecular and atomic ions, *e.g.* they always contain a fraction of $^{16}O^-$. Using knowledge of the natural abundance of osmium and of a prior mass spectrum measurement [24] in which a similar ion source was used, it was concluded that a mass separator with a resolving power of at least 100 is required for our experiment. Since a magnetic sector lens (bending magnet) was available at the MPI-K, one main goal of this diploma thesis was to find out whether a mass resolving power of a configuration using this bending magnet of at least 100 could be reached. For this purpose simulations with simion 8 were performed. Since osmium tetroxide is hazardous it was decided to use a different target material (FeS) for a first operation of our setup. Therefore a mass spectrum simulation assuming an FeS target was also made. Comparing the full width at half maximum of the peaks in the mass spectrum of simulation and measurement gives insight into the resolving power of the mass separator.

This chapter begins with an overview of the beam line of our experimental setup. The design of the beam line is described. Afterward, it is shown how the geometries of the components of the beam line appear in the simulation, and the simulation parameters are presented. Finally, the results of a mass spectrum measurement with FeS target material are presented. The mass spectrum of simulation and measurement, both with FeS target, are compared. From this comparison the resolving power of the mass separator in our setup is calculated.

4.1 Overall setup

As previously noted, the motivation for this experiment is the trapping and laser cooling of negative osmium ($^{192}Os^-$) in a cylindrical Penning trap. A sectional view (from the top) of the whole beam line is given in Fig. 4.1. The Penning trap, which is currently being built, will be positioned in a large vacuum chamber within a solenoid magnet. In order to ensure the operation of the superconducting coils, they have to be cooled with liquid He to about

4 K temperature. The temperature of the trap and its surrounding will be maintained at about 40 K by the secondary stage of the magnet's cryocooler.

The negative ion sputter source MISS (Sec. 3.2.4) is used to generate the negative osmium ions. The MISS not only generates negative osmium ions but also oxygen ions, molecular ions, and a mixture of all naturally occurring osmium isotopes. The desired negative ion for laser cooling is $^{192}Os^-$, while other ions in the Penning trap are unwanted. Therefore a mass separation is necessary to ensure that an $^{192}Os^-$ beam as pure as possible reaches the trap region.

Just after the MISS, an einzel lens is used to transform the divergent beam delivered from the MISS into a beam able to pass the the vacuum chambers and further beam line components. An electrostatic quadrupole triplet follows the einzel lens. Its task is to maximize the transmission through the mass separation system. The mass separation system consists of slits, drift spaces, and a 90° bending magnet. The magnetic field of the bending magnet can be adjusted by changing the current in the magnet coils in order to maximize the transmission through the separation system for ions of desired mass. The next beam line component is again an electrostatic quadrupole triplet. The function of this triplet is the optimization of the beam transmission through the remaining components of the beam line. Furthermore, it is used to compensate asymmetries in the transverse beam profile. This part of the beam line was finished within my diploma thesis.

For the next beam line component, it is planned to use an electrostatic 90° bender. This bender has shields with gaps large enough for the transmission of laser beams necessary for laser cooling. The further design of the beam line is not yet completed, but will require the simulation to be expanded by additional beam line components. Behind the electrostatic bender at least an einzel lens will have to be positioned to focus the beam into the center of the Penning trap.

For beam diagnostics two Faraday cups are used to measure the beam current. One is situated right behind the entrance slits of the mass separation system, and the other one is behind the exit slits. Each cup is mounted on a linear feedthrough, such that it can be placed into the beam if a current measurement is desired. The beam optimization of the already finished beam line, in practice, is based on the beam current measurement with these two Faraday cups. For beam optimization of the further beam line, an additional Faraday cup will be required. This cup should have a small entrance aperture of a few mm and should be temporarily mounted near the center of the future Penning trap prior the operation of the trap.

The trap is planed to be filled with ions from a pulsed ion beam. On both sides of the trap, high-voltage electrodes are positioned to reflect the ions. A beam pulse will be captured by fast switching the voltage on the entrance electrode once the pulse has passed it. The trap, *i.e.* its capturing electrodes, is designed to capture ions of at most 5 keV energy. For beams with high energy, the demands on the beam quality are somewhat lessened. Considering the acceptances of the beam line components and vacuum tubes, and

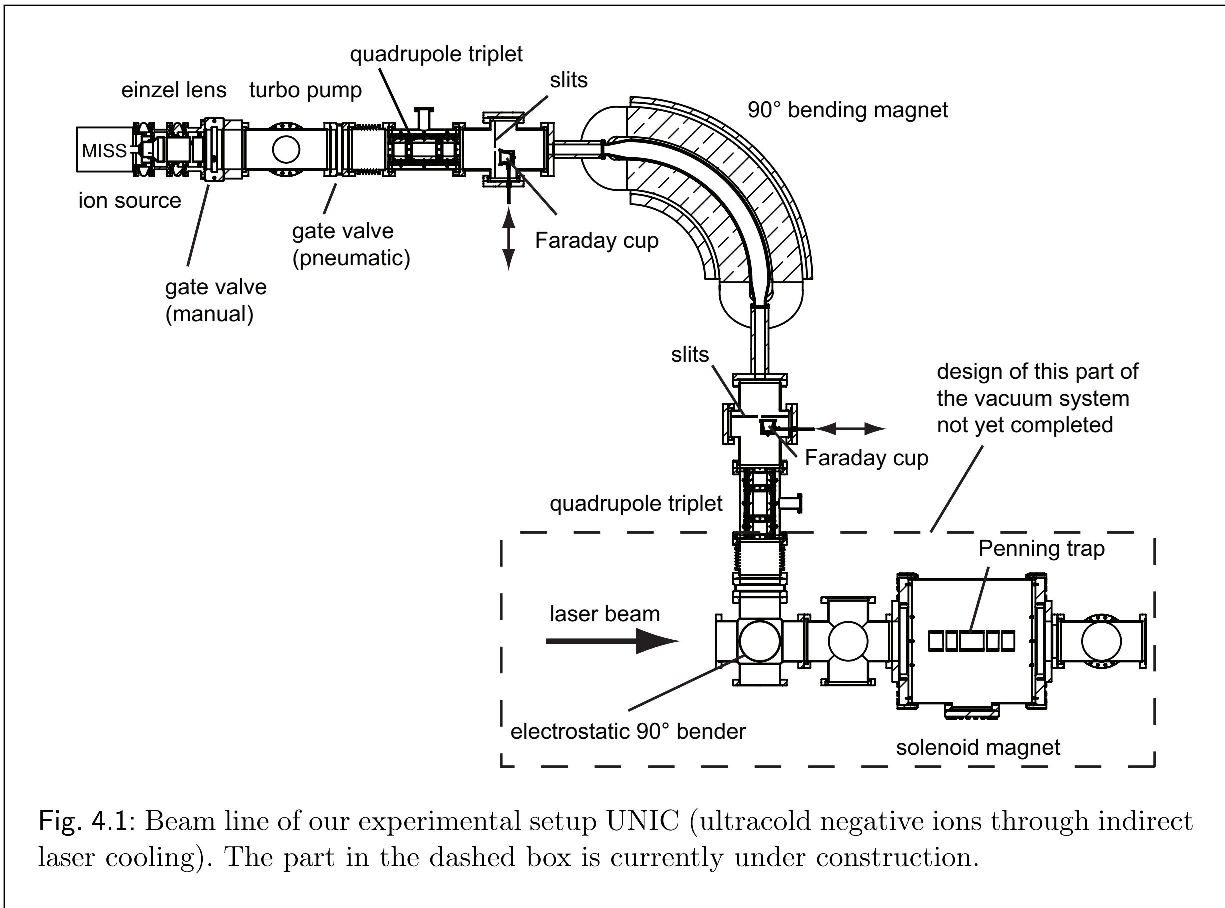

Fig. 4.1: Beam line of our experimental setup UNIC (ultracold negative ions through indirect laser cooling). The part in the dashed box is currently under construction.

the efficiency of the mass separation system, a beam with an energy as high as possible should be chosen in order to reach a maximum beam current and $^{192}Os^{-}$ beam pureness. Based on these competing requirements, it was decided to choose a beam energy of 5 keV and design the beam line components accordingly.

4.2 Ion optical simulation

Figure 4.2 shows the latest version of the geometries and ion trajectory simulations with simion corresponding to the setup in Fig. 4.1. The only component that is not presented in detail here is the electrostatic bender since the design of that part of the beam line is not completed yet, and is not of immediate interest for the simulations and measurements presented below.

In all simulations presented here, space charge effects and particle interactions, *i.e.* the Coulomb repulsion between ions, are neglected. Simion 8 is not able to take space charge effects into account, but can approximate the Coulomb repulsion between the ions. Nev-

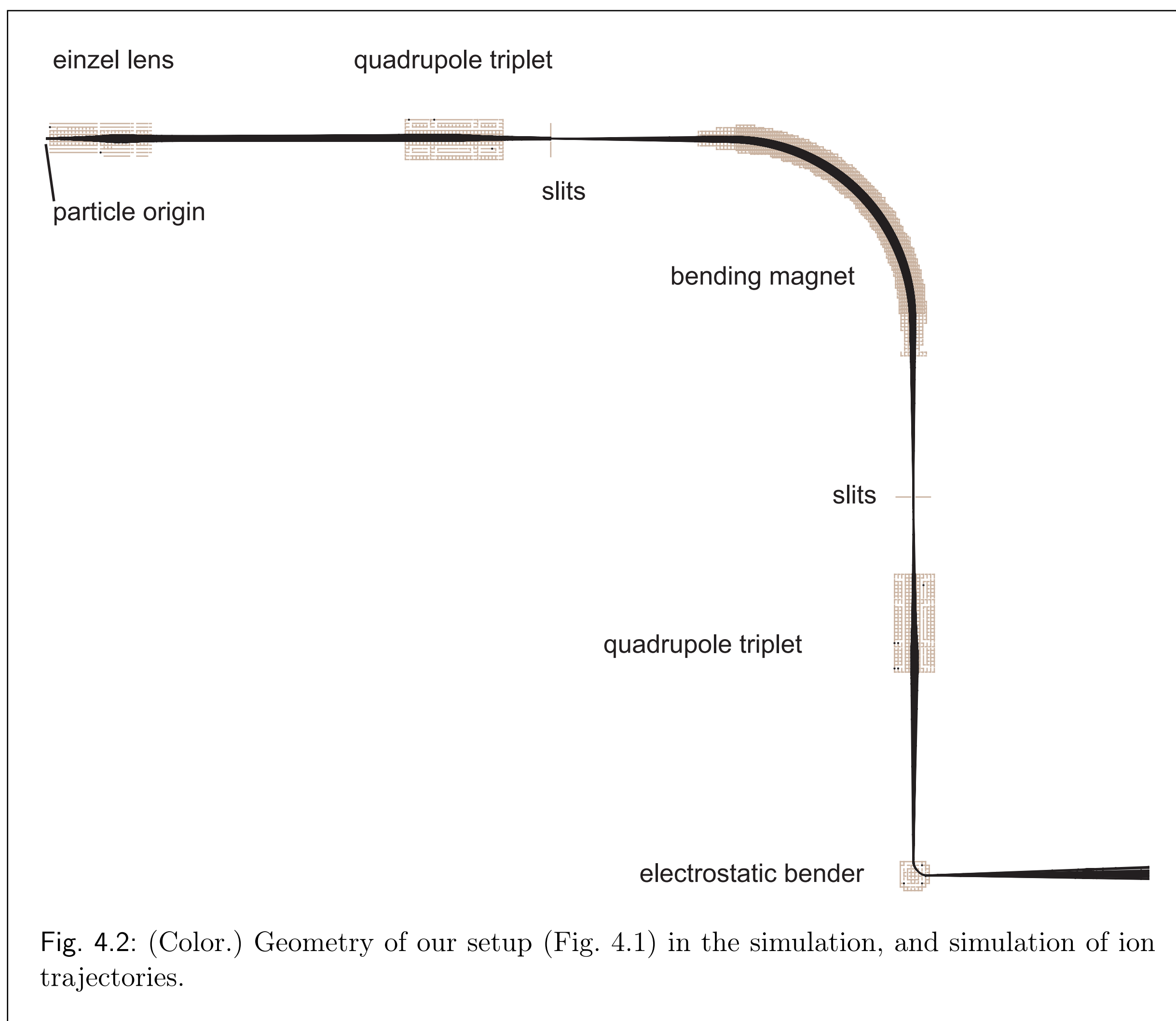

Fig. 4.2: (Color.) Geometry of our setup (Fig. 4.1) in the simulation, and simulation of ion trajectories.

ertheless, this feature was not used in the simulations of the mass spectra, since it would have dramatically increased the computing time. Simulations of the beam line with activated charge repulsion effect approximation have shown that charge repulsion has almost no effect on the beam for beam currents up to 1 µA, and little effect for 10 µA. Taking the voltage settings from a simulation without charge repulsion effects, it should be possible to compensate these effects by slightly tuning the voltages in the setup. At any rate, the voltage settings delivered from the simulation can only be considered a starting point for a beam optimization with the real setup.

4.2.1 Source and einzel lens

To simulate the entire beam line in one single simulation with simion 8, it was convenient to start the simulation after the ion extraction, *i.e.* the simulated particles started to evolve from a position that would in reality be within the exit aperture of the extraction electrode (Fig. 4.3) with a given direction, energy and position distribution. This was done for the following reasons:

- Not all effects occurring in the source are completely known. One could therefore not be sure to include all of these effects in a simulation.
- It would exceed the capabilities of simion to include the simulation of the entire beam generation process.
- Even if possible, this would require unnecessary computer capacity and increase the computing time.

Figure 4.3 shows a sectional view of the MISS and its einzel lens, as well as the geometry of the simulated einzel lens and the beam passing the lens.

Beam properties, like emittance and beam energy distribution (beam temperature), of beams generated by the MISS ion source are unfortunately unknown, since no experimental setup to accomplish such measurements is available at the MPI-K. Up to now, none of these properties were of interest for the operation of the MISS. The purity of the generated (separated) $^{192}Os^-$ ion beam and its current have to be determined experimentally.

In the simulation, the singly charged negative ions start from within a circular area with 3 mm diameter, which corresponds to the extraction exit aperture. The ion energy distribution is a Gaussian distribution with a full width at half maximum of 1 eV around the main value of 5 keV. As already explained above, the energy distribution of the ion beam is unknown. If it were the thermal energy distribution of the target, the full width half value of 1 eV would, for sure, be a worst case value, corresponding to a temperature in the order of 10^4 K.

The directional distribution of the ions is chosen to be a homogeneous distribution with a maximum angle between z-axis (beam main axis of propagation) and individual ion direction of propagation of 2.5°, since it is slightly too large to pass the beam through the beam line without losses. As mentioned before, the emittance of the ion beam is unknown, but with the voltages obtained from the simulation with minimal losses, the real beam line is also optimized.

In Fig. 4.4 a potential view of the potential inside the einzel lens and on its electrodes is shown. The voltages on the outer electrodes are set to ground, while that of the central electrode is set to ≈ -3850 V in all the simulations presented here. The ions leave the einzel lens as an approximately parallel beam until they reach the first electrostatic quadrupole triplet.

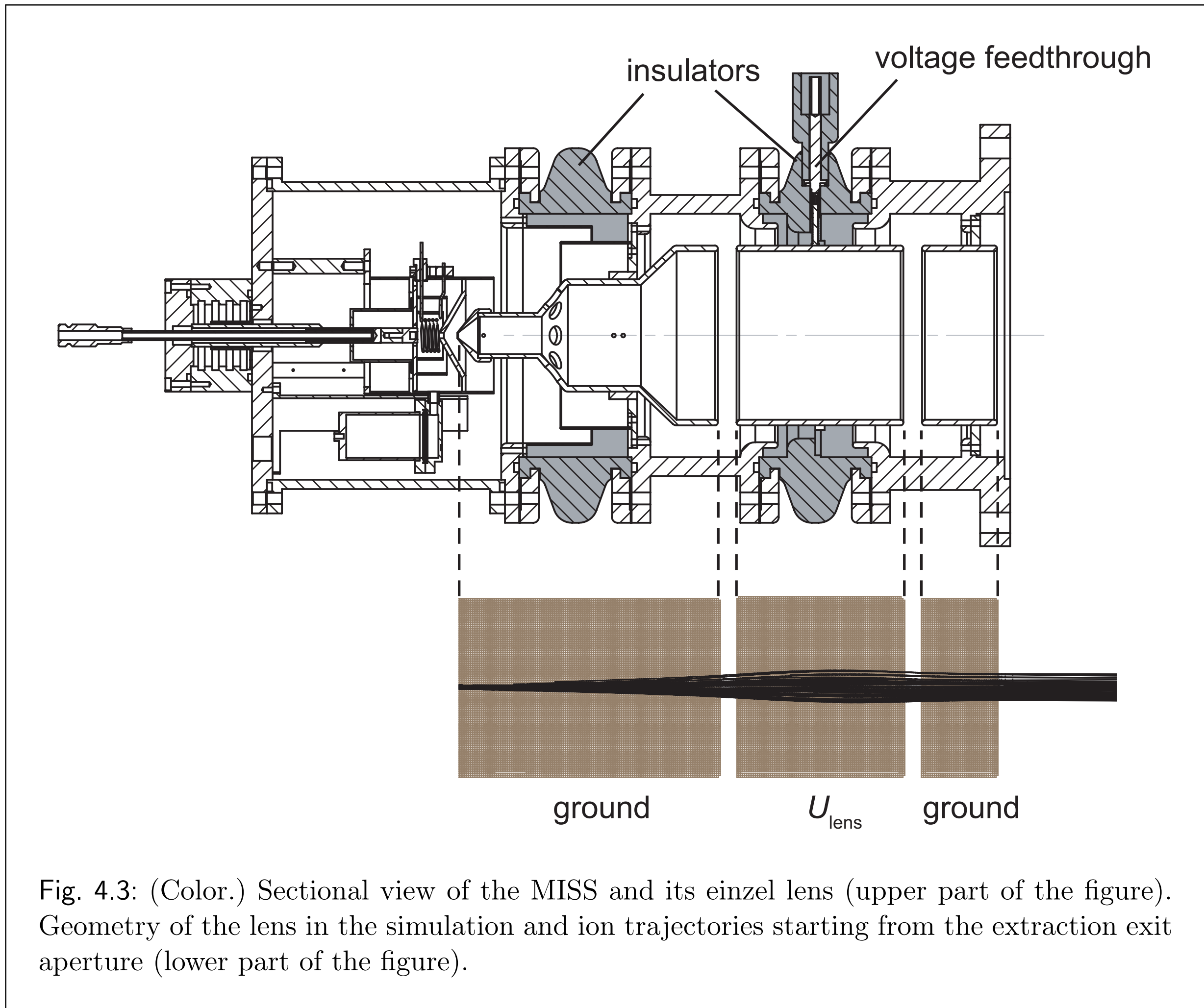

Fig. 4.3: (Color.) Sectional view of the MISS and its einzel lens (upper part of the figure). Geometry of the lens in the simulation and ion trajectories starting from the extraction exit aperture (lower part of the figure).

4.2.2 Quadrupole triplets

In the beam line of our experimental setup, two identical electrostatic quadrupole triplets are used. A quadrupole triplet is simply a sequence of three independent quadrupoles. With quadrupoles the transverse beam profile of the beam can be tuned in order to match the acceptance of vacuum chambers and/or ion optical elements and so to maximize the beam current. The bending magnet, for instance, has a different effect on the two transverse emittances, *i.e.* in the x-direction it acts as a lens and in the y-direction it acts as a drift space. A symmetric beam profile will no longer be symmetric after the beam has passed the bending magnet. This can be compensated with quadrupoles. Figure 4.5 shows a cut through a triplet without vacuum chamber (upper figure) and a potential view in the cutting plane (lower figure).

The first quadrupole of the first triplet is used as a steerer, *i.e.* it is not used as a

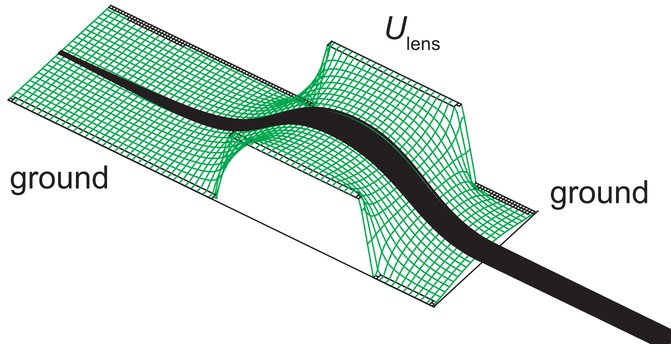

Fig. 4.4: (Color.) 3d potential view of the einzel lens in Fig. 4.3. The potential is a function of the position in the sectional plane of Fig. 4.3. The potential view is inverted, *i.e.* the voltage of the central electrode in negative. Ions passing the central electrode have lower kinetic energy than before and after it.

quadrupole. The central quadrupole focuses the beam to the center of the gap between the first two slits, and in the perpendicular plane, the beam is focused to the center of the bending magnet (Fig. 4.6). In this configuration, a maximal beam transmission is accomplished in the simulation if the voltage of the central quadrupole is set to 190 V and that of the last (closest to slits) is set to -325 V. Opposing electrodes are set to the same voltage, whereas the voltages of upper and lower electrode ($U_{\mathrm{QP2,EL1}}$, $U_{\mathrm{QP2,EL3}}$) of the central quadrupole are set to 190 V and those of the left and right ($U_{\mathrm{QP2,EL2}}$, $U_{\mathrm{QP2,EL4}}$) are set to -190 V. In the last quadrupole the voltage of the upper and lower electrode ($U_{\mathrm{QP3,EL1}}$, $U_{\mathrm{QP3,EL3}}$) are set to -325 V and those of the left and right electrode ($U_{\mathrm{QP3,EL2}}$, $U_{\mathrm{QP3,EL4}}$) are at 325 V.

4.2.3 Bending magnet

The bending magnet used in our setup is a 90° magnetic dipole sector lens. It consists of a copper coil generating a magnetic field and yokes to define the geometry of the field region. The magnetic field of an ideal magnetic dipole sector lens is uniform inside the gap and vanishes outside the gap. For real bending magnets, fringe field effects occur (Sec. A.9).

For ions passing the gap, the bending magnet acts as a drift space in the direction of the magnetic field lines (here y-direction). Perpendicularly to the magnetic field lines it acts as a lens (here x-direction). Figure 4.9 shows the geometry of the bending magnet in the simulation and ion trajectories.

In the simulation of the bending magnet, a volume between two electrodes defining the gap and its volume is set to have a magnetic field of desired strength. In the mass spectra

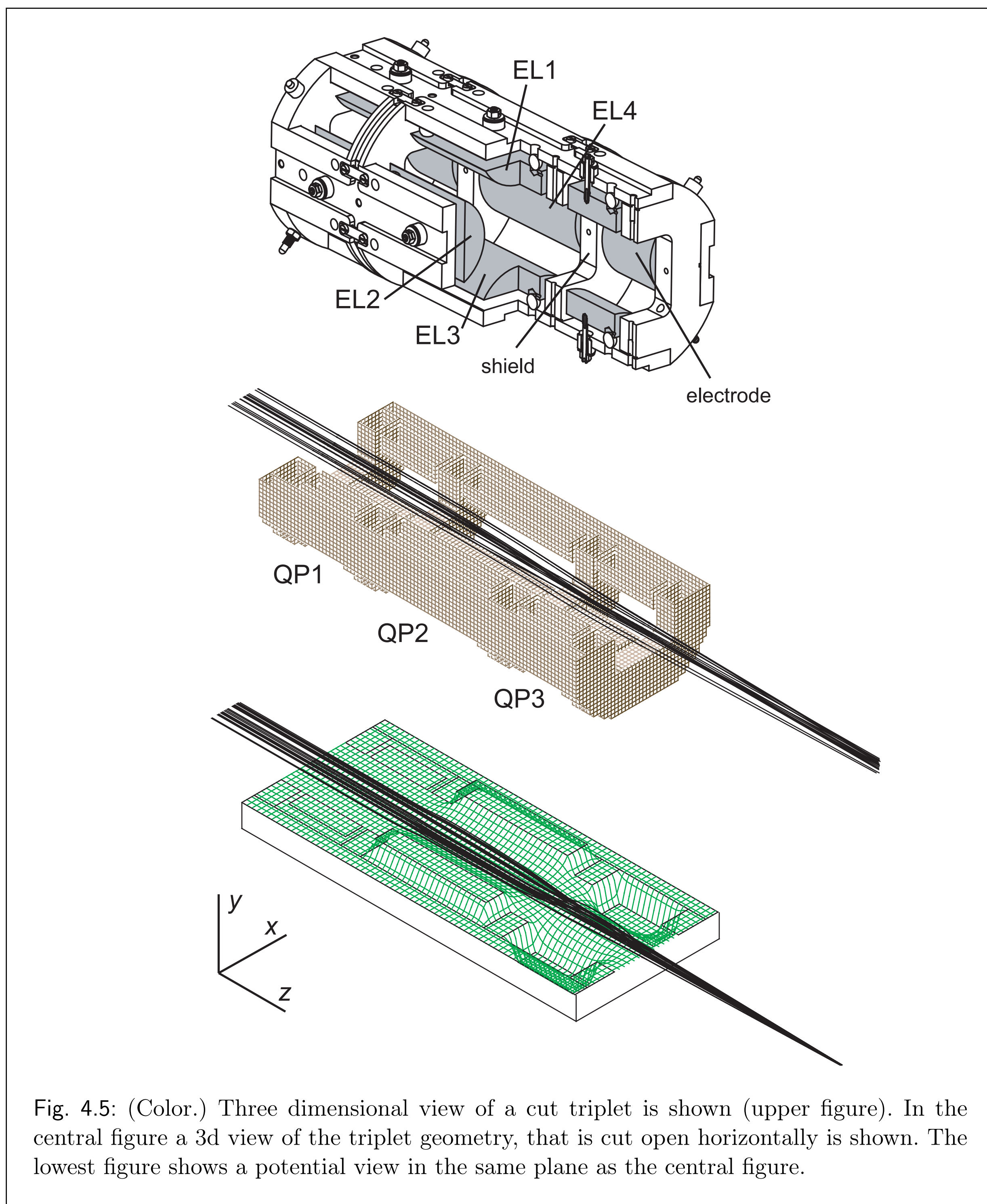

Fig. 4.5: (Color.) Three dimensional view of a cut triplet is shown (upper figure). In the central figure a 3d view of the triplet geometry, that is cut open horizontally is shown. The lowest figure shows a potential view in the same plane as the central figure.

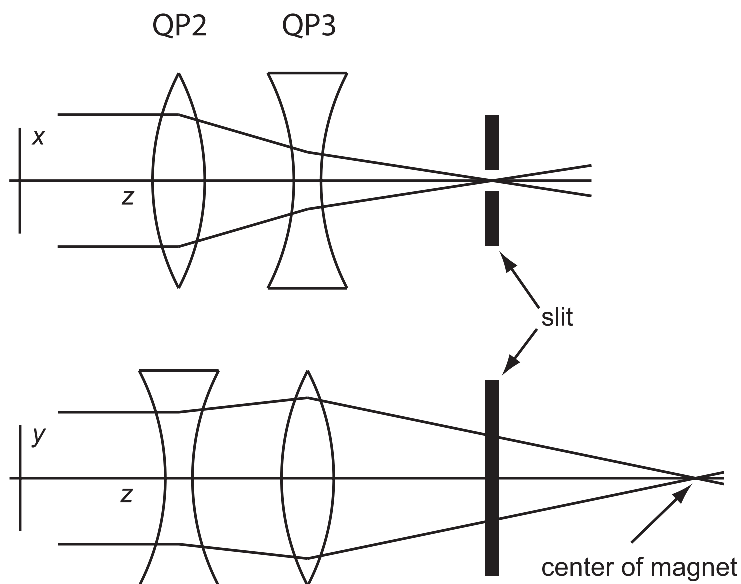

Fig. 4.6: In this configuration, the central and the last quadrupole are used, while the first quadrupole is used for steering only.

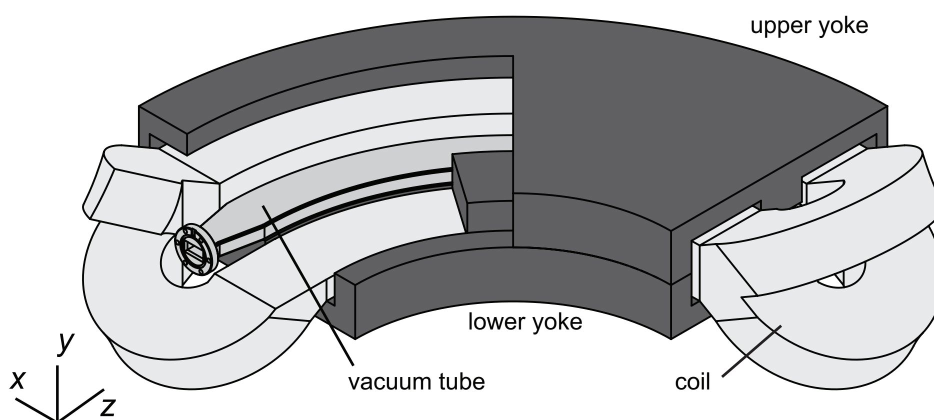

Fig. 4.7: View of our 90° bending magnet. The upper yoke is cut off for illustration purposes.

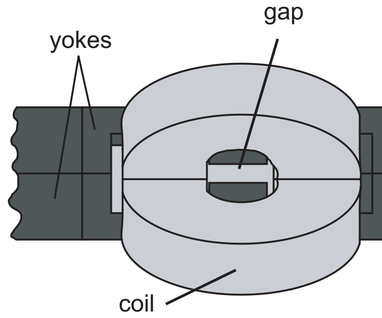

Fig. 4.8: Partial view of our 90° bending magnet from one side without vacuum tube.

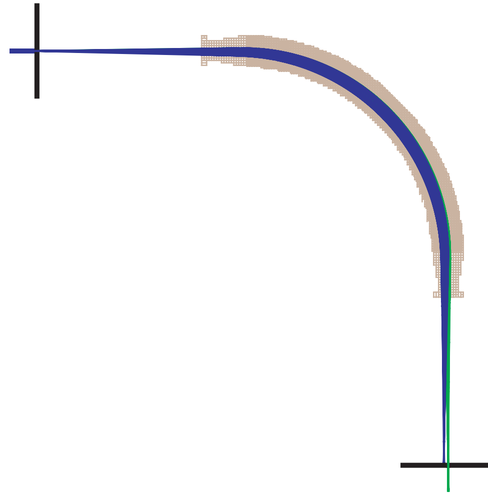

Fig. 4.9: (Color.) Simulation of trajectories of negative ions passing our bending magnet, performed with simion 8. The beam energy follows a Gaussian distribution with maximum value at 5 keV and a full width at half maximum of 1 eV, the Larmor radius $\rho = 501.5$ mm and the distance w_o between the slits is 2 mm. Two ion groups with a relative mass difference $m/\Delta m \approx 50$ are flown. The green colored are the desired ions while the blue ones are separated from the beam.

simulations, this value of the magnetic field strength is changed by a desired step size, every time, after all ions have finished their flight.

In Fig. 4.9 the result of all particle trajectories for one magnetic field value is shown. It can be considered as one step in the mass spectrum simulation. Two particle groups of negative ions but with a relative mass difference of $m/\Delta m \approx 50$ pass the vacuum tube inside the bending magnet. In our configuration the object and image planes are defined by slits that all have the same distance from the bending magnet edges, *i.e.* they are placed in a symmetric configuration. Since we use a 90° bending magnet, the distance of the object and image plane from the effective field boundary is equal to the Larmor radius of the desired particles, in our case $\rho = 501.5$ mm. The particle group of the desired mass is colored in green, while the undesired is colored in blue. Prior to the separation of both groups, the green trajectories are covered by the blue ones. The mass resolution of this configuration is given by

$$\frac{\Delta m}{m} = \frac{w_o}{\rho} + 2\frac{\Delta E}{E}, \tag{4.1}$$

$$\approx \frac{2 \text{ mm}}{500 \text{ mm}} + \frac{1 \text{ eV}}{5000 \text{ eV}}, \tag{4.2}$$

$$\approx \frac{1}{240}. \tag{4.3}$$

The energy uncertainty ΔE of our beam is unknown, but other experiments with similar ion sources have shown that mass resolutions of about 200 were reached with beams of energies around 20 keV [24] and even at lower energy around 8 keV [9].

4.2.4 Simulation of mass spectra

With the voltage settings given above, ion groups with different ion masses and number of ions are started from the particle origin. These voltage settings are summarized in Tab.4.1. After the calculation of all trajectories is finished, the strength of the magnetic field of the bending magnet is increased by a step size value and the particles are started again. This procedure is repeated with a loop, with defined starting value, end value and step size. The programing language is "Lua" and in simion 8, Lua-programs can control workbench programs from outside, *i.e.* they can set voltages and magnetic fields and command simion to compute ion trajectories.

In Fig. 4.10, the setup in the simion workbench program is shown. The geometries and voltage settings are equal to those indicated above. In order to decrease the computation time, only necessary beam line components are used in the workbench. In the simulation, an empty volume acts as a Faraday cup. All particles reaching this empty volume are counted. The magnetic field strength and the number of counts are written into a data file.

beam line component	electrode/voltage name	value
particle origin	beam energy	5000 eV
einzel lens	U_{lens}	-3846 V
quadrupole 1	$U_{\mathrm{QP1,EL1}}$	0 V
quadrupole 1	$U_{\mathrm{QP1,EL2}}$	0 V
quadrupole 1	$U_{\mathrm{QP1,EL3}}$	0 V
quadrupole 1	$U_{\mathrm{QP1,EL4}}$	0 V
quadrupole 2	$U_{\mathrm{QP2,EL1}}$	190 V
quadrupole 2	$U_{\mathrm{QP2,EL2}}$	-190 V
quadrupole 2	$U_{\mathrm{QP2,EL3}}$	190 V
quadrupole 2	$U_{\mathrm{QP2,EL4}}$	-190 V
quadrupole 3	$U_{\mathrm{QP3,EL1}}$	-325 V
quadrupole 3	$U_{\mathrm{QP3,EL2}}$	325 V
quadrupole 3	$U_{\mathrm{QP3,EL3}}$	-325 V
quadrupole 3	$U_{\mathrm{QP3,EL4}}$	325 V

Tab. 4.1: Voltage settings of the ion optical elements used in the mass spectra simulations. The beam energy is a Gaussian distribution with full width at half maximum of 1 eV and maximum at 5000 eV.

The particle settings for a simulation with an FeS target are shown in Tab. 4.2. The ratio of the number of particles is based on the isotopic distributions of the materials, the measurements above (Fig. 3.12) and in Ref. [24]. In Fig. 4.11, the corresponding simulated mass spectrum is plotted. The same simulation was then repeated for naturally distributed osmium. The ratio of the number of particles is chosen accordingly, as shown in Tab. 4.3. Moreover, it is assumed that about 10% of the ions are OsH^- ions, while only $^{190}Os^1H^-$ and $^{192}Os^1H^-$ are taken into account, since they are of particular interest with respect to mass separation. The others are neglected here to save computing resources.

4.3 Experimental results

In order to obtain a mass spectrum, the beam current behind the mass separation system was measured with a Faraday cup behind the mass separation system as a function of the coil current of the bending magnet. The results are shown in Fig. 4.13. The target material in the MISS was FeS and the beam energy was set to 5 keV. The starting points of the voltage settings are based on the simulation described to that above. Before the measurement started, the voltages were tuned in order to maximize the beam current behind the mass separator. In Tab. 4.4, the voltage settings of the different beam line

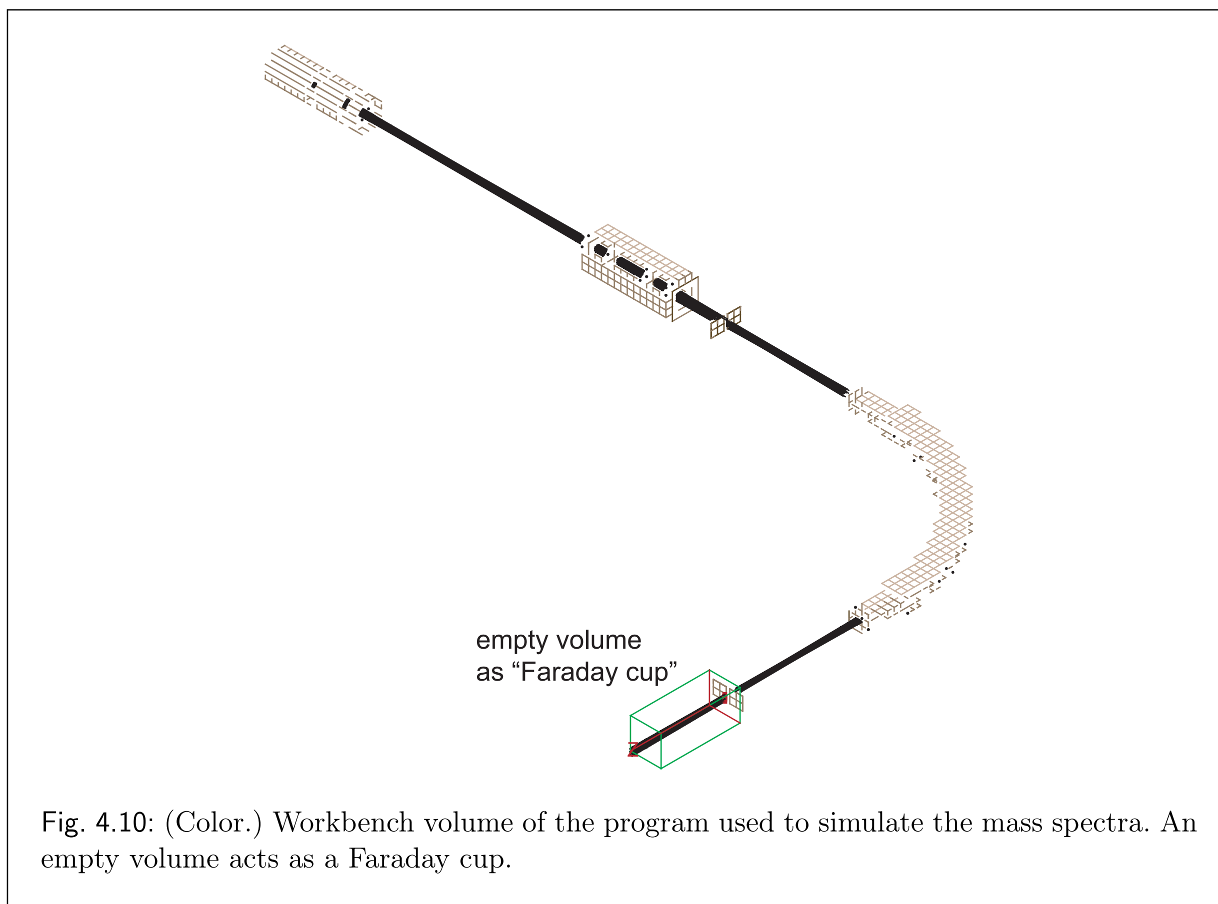

Fig. 4.10: (Color.) Workbench volume of the program used to simulate the mass spectra. An empty volume acts as a Faraday cup.

ion	ion mass	number of particles
$^{16}O^-$	16	500
$^{16}O^1H^-$	17	50
$^{32}S^-$	32	500
$^{34}S^-$	34	22
$^{32}S^{16}O^-$	48	25
$^{32}S_2^-$	64	25
$^{54}Fe^{16}O^-$	70	19
$^{56}Fe^{16}O^-$	72	300
$^{56}Fe^{32}S-$	88	150

Tab. 4.2: Particle settings for the simulation with a FeS target. The simulated mass spectrum is shown in Fig. 4.11.

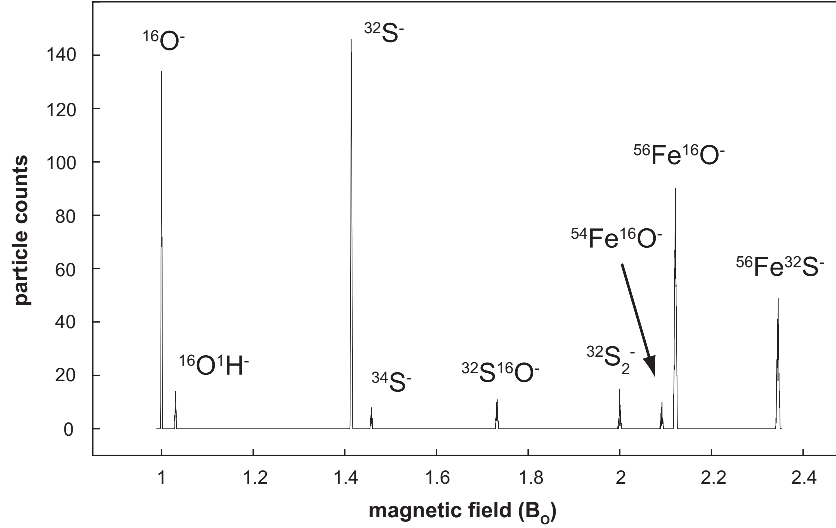

Fig. 4.11: Simulation of a mass spectrum for a FeS target. The individual data points are not shown.

ion	ion mass	number of particles
$^{188}Os^-$	188	133
$^{189}Os^-$	189	174
$^{190}Os^-$	190	280
$^{190}Os^1H^-$	191	26
$^{192}Os^-$	192	410
$^{192}Os^1H^-$	193	41

Tab. 4.3: Particle settings for a simulation with an osmium target. The resulting mass spectrum of the simulation is shown in Fig. 4.12.

components during the measurement are summarized. Furthermore, Tab. 4.5 shows the MISS operating parameter settings with our ion source during the measurement. Based on the measurement above (see Fig. 3.12), on the measurements from Ref. [24], and using knowledge on the atomic and molecular ions that can occur in the ion beam with respect to the materials in the MISS, the different peaks are assigned to the different ion masses. It should be mentioned that in our present setup the transmission of the ion beam for passing the bending magnet (and the exit slits) is measured to be around 10%, which may look small to the reader but is expected, since the vacuum chamber of the bending magnet has

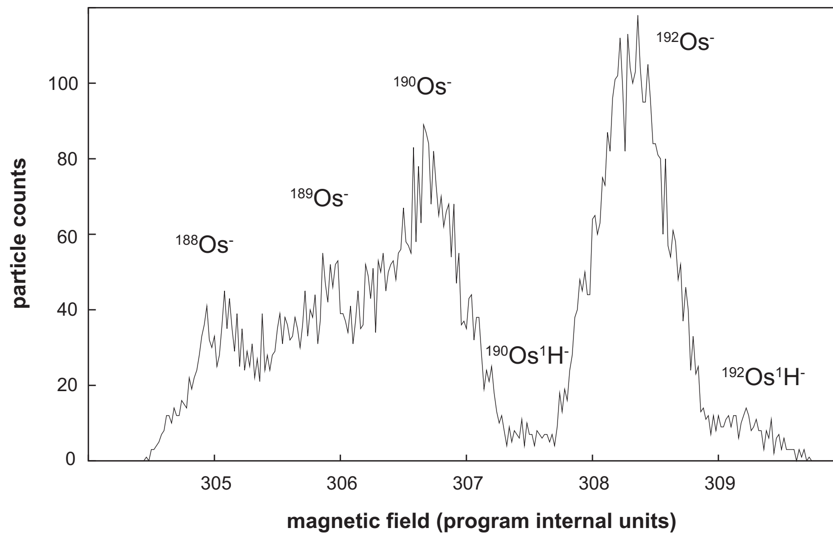

Fig. 4.12: Resulting spectrum from the simulation for a naturally distributed osmium target. Statistical uncertainties, due to a limited number of ions, are responsible for the fluctuations.

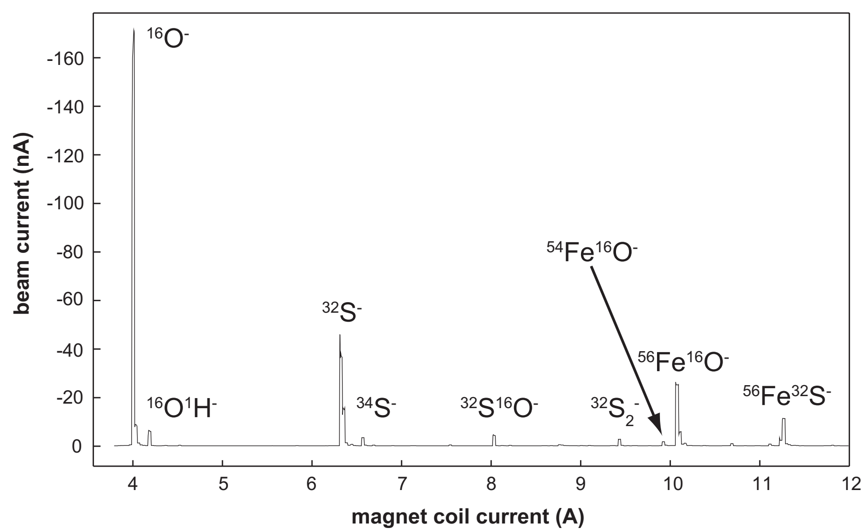

Fig. 4.13: Mass spectrum obtained with a FeS target and 5 keV beam energy. The beam current was measured behind the mass separation as a function of the bending magnet current.

beam line component	electrode/voltage name	voltage (V)
MISS	U_{cath}	-2000(2)
MISS	U_{beam}	-5000(5)
einzel lens	U_{lens}	-3716(4)
quadrupole 1	$U_{\text{QP1,EL1}}$	160.0(1)
quadrupole 1	$U_{\text{QP1,EL2}}$	-210.0(1)
quadrupole 1	$U_{\text{QP1,EL3}}$	220.0(1)
quadrupole 1	$U_{\text{QP1,EL4}}$	-170.0(1)
quadrupole 2	$U_{\text{QP2,EL1}}$	-19.2(1)
quadrupole 2	$U_{\text{QP2,EL2}}$	19.2(1)
quadrupole 2	$U_{\text{QP2,EL3}}$	-19.2(1)
quadrupole 2	$U_{\text{QP2,EL4}}$	19.2(1)
quadrupole 3	$U_{\text{QP3,EL1}}$	-211.5(1)
quadrupole 3	$U_{\text{QP3,EL2}}$	211.5(1)
quadrupole 3	$U_{\text{QP3,EL3}}$	-211.5(1)
quadrupole 3	$U_{\text{QP3,EL4}}$	211.5(1)

Tab. 4.4: Voltage settings of the ion optical elements during in the mass spectrum measurement. The uncertainties in the brackets behind the numbers result from the uncertainties of the power supplies.

parameter name	abbreviation	parameter value
filament current (voltage setting)	U_{fil}	3.25 V (∼25 A)
source temperature (voltage reading)	U_{source}	1.48 V (∼300 °C)
cesium reservoir temperature (voltage reading)	U_{Cs}	4.26 V (∼85 °C)
source pressure	p_{source}	$3.4 \cdot 10^{-6}$ mbar
pressure first triplet (“Fix”)	p_{Fix}	$1.7 \cdot 10^{-6}$ mbar
pressure second triplet (“Foxy”)	p_{Foxy}	$2.9 \cdot 10^{-7}$ mbar

Tab. 4.5: Parameter settings and vacuum pressures during the measurement. The U_{fil} is a controlling voltage setting, while U_{source} and U_{Cs} are read voltages from thermal element electronic circuits.

rather small appertures, of around 20 mm. Furthermore, a small part of the beam is lost at the exit slits (the slit width is 2 mm). The $^{32}S^-$ beam current of the measurement shown in Fig. 4.13 was around 40 nA, which is much smaller than expected, since a beam current of at least 100 nA is predicted from a worst-case estimation for a cathode voltage of 2 kV. The temperature reading of the temperatures in the MISS is somewhat unreliable. It is assumed that the reason for the low current was that the cesium reservoir temperature during the measurements at our setup was lower than that in the measurements in the accelerator hall (Sec.3.3). In later measurements, a 200 nA beam current of $^{32}S^-$ was observed. In these measurements, the cesium reservoir temperature was increased from 85°C to around 95°C (in our present temperature reading) and the voltage settings of the quadrupole were further optimized. The large $^{16}O^-$ beam current was also unexpected. Despite the vacuum pressure of around 10^{-5} mbar, which is normal during source operation, the $^{16}O^-$ beam current indicates a possible leak in the vacuum chambers around MISS and the einzel lens, or outgassing from electrodes. In the following, a linear fit to the functional dependence of the square root of the atomic mass of separated ions and the bending magnet current is performed. For this purpose, a few consideration must be made: The Larmor radius of particles moving inside the bending magnet, as a function of their mass and the magnetic field B, is given by:

$$\rho = \frac{mv}{qB}. \tag{4.4}$$

We now consider the bending magnet as an ideal 90° sector magnet with an effective field B_{eff}. Only ions having the Larmor radius ρ_0 given by the geometry of the mass separator can pass it. With $v = \sqrt{2E/m}$ for a monoenergetic beam and singly charged ions we can conclude that:

$$B_{\text{eff}} = \frac{\sqrt{2E}}{q\rho_0} \cdot \sqrt{m}. \tag{4.5}$$

If we assume that $B_{\text{eff}}(I) = c \cdot I + B_0$ (where c is a constant) we can conveniently substitute:

$$\sqrt{m} = a \cdot I + b, \tag{4.6}$$

where a and b are two unknown constants that can be found by fitting this function. Data points (I, $\sqrt{m}$) were extracted from the named peaks in the plot in Fig. 4.13, where m is chosen to be in atomic mass units u. The data points and the function $\sqrt{m} = a \cdot I + b$ are plotted in Fig. 4.14. The uncertainty of the current I correspond to the full width at half maximum of the peaks, while the values of $\sqrt{m}$ have no uncertainty here, since they are discrete. The fit results for a and b are:

$$a = (0.749 \pm 0.003)\ \frac{\sqrt{\text{u}}}{\text{A}}, \tag{4.7}$$

$$b = (0.91 \pm 0.02)\ \sqrt{\text{u}}. \tag{4.8}$$

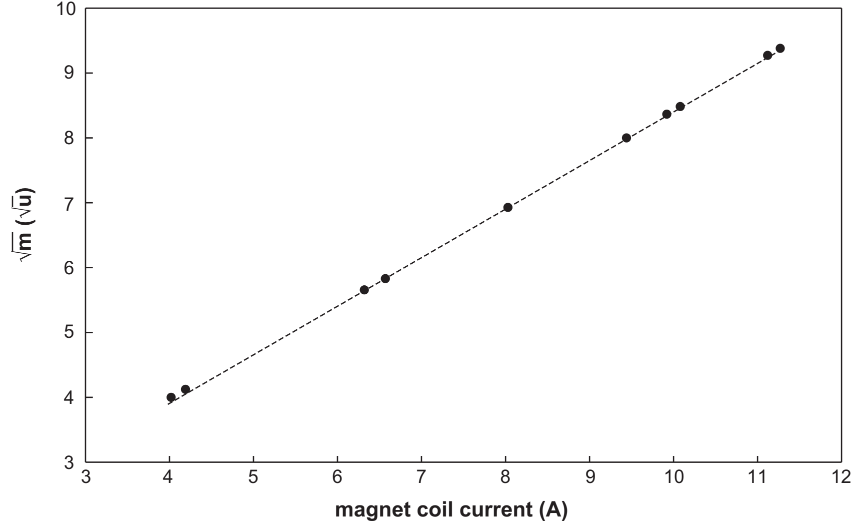

Fig. 4.14: Plot of the data extracted from the mass spectrum in Fig. 4.13 along with a linear fit $\sqrt{m} = a \cdot I + b$, where $a = (0.749 \pm 0.003)\ \sqrt{\mathrm{u}}/\mathrm{A}$ and $b = (0.91 \pm 0.02)\ \sqrt{\mathrm{u}}$. The (horizontal) error bars, corresponding to the width of the peaks in the mass spectrum are too small to be seen. The target material was FeS and the beam energy was 5 keV.

With:

$$\sqrt{m} = \frac{q\rho_0}{\sqrt{2E}}(c \cdot I + B_0), \tag{4.9}$$

$$= a \cdot I + b, \tag{4.10}$$

we find:

$$c = \frac{\sqrt{2E}}{q\rho_0}\ a, \tag{4.11}$$

$$B_0 = \frac{\sqrt{2E}}{q\rho_0}\ b. \tag{4.12}$$

Assuming that the uncertainty of the Larmor radius $\rho_0 = 501.5$ mm given by our geometry is 2 mm and that the beam is monoenergetic with a beam energy of 5 keV, this yields:

$$c = 152.05(86)\ 10^{-4}\ \frac{\mathrm{T}}{\mathrm{A}}, \tag{4.13}$$

$$B_0 = 184.7(4)\ 10^{-4}\ \mathrm{T}, \tag{4.14}$$

or

$$B_{\text{eff}}(I) = \left(152.05 \frac{1}{\mathrm{A}} \cdot I + 184.7\right) 10^{-4}\ \mathrm{T}. \tag{4.15}$$

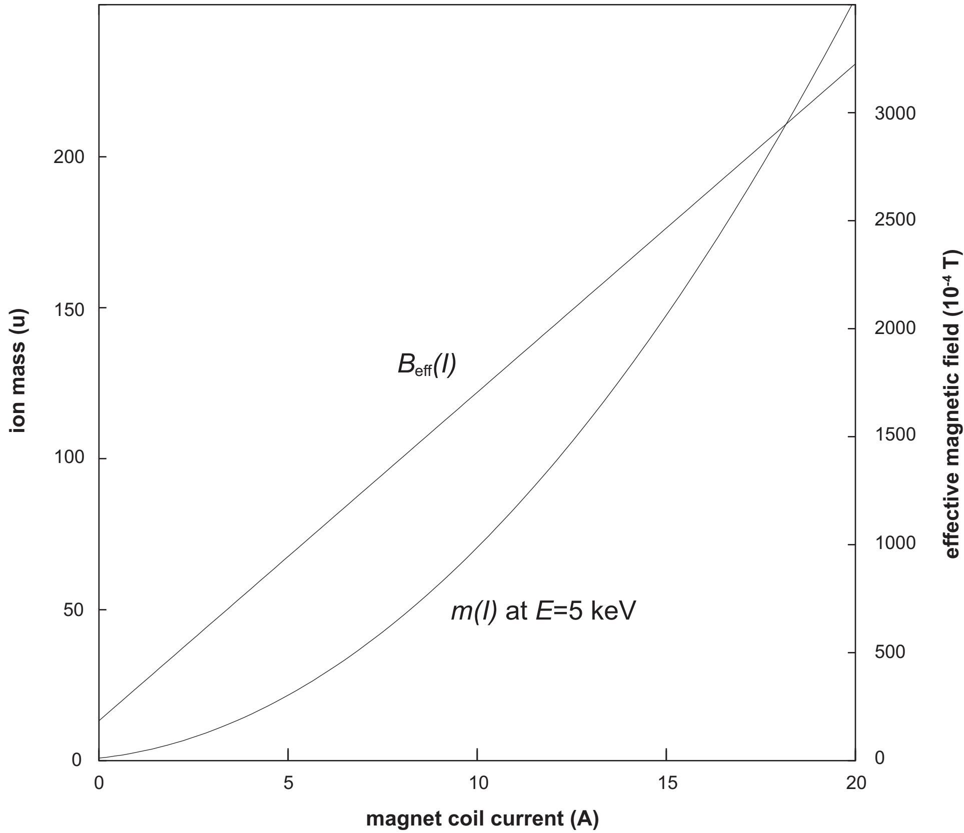

Fig. 4.15: Characteristic plot of our mass separation system. For a 5 keV beam the ion mass $m(I) = (0.749/\mathrm{A} \cdot I + 0.91)^2$ u is plotted as a function of the magnet coil current. Furthermore, the effective magnetic field $B_{\mathrm{eff}}(I) = (152.05/\mathrm{A} \cdot I + 184.7)10^{-4}$ T is plotted.

B_0 arises from hysteresis effects. The ion mass and the effective magnetic field are plotted as a function of the coil current of the bending magnet in Fig. 4.15.

To make conclusions about the beam energy distributions and the resolution of the mass separator, the full width at half maximum of the peaks in the FeS mass separation measurement ΔM_{FWHM} (Fig. 4.13), and that of the simulation ΔS_{FWHM} (Fig. 4.11) are compared. Table 4.6 shows the ratio $r_{\mathrm{MS}} := \Delta M_{\mathrm{FWHM}}/\Delta S_{\mathrm{FWHM}}$ of the full width at half maximum of measurement and simulation. The average value of the ratio r_{MS} is found to be 2.25(61). This means that the resolution of the mass separation configuration in the measurement is by this factor smaller than that of the simulation. With a mass resolution in the simulation of about 240, the mass resolution of the mass separator used in the measurement is calculated to be 107(29).

Since the mass resolution is proportional to the inverse of the full width at half maxi-

ion (peak)	ion mass (u)	r_{MS}
$^{16}O^-$	16	3.0
$^{16}O^1H^-$	17	3.5
$^{32}S^-$	32	2.1
$^{34}S^-$	34	1.9
$^{32}S^{16}O^-$	48	1.8
$^{32}S_2^-$	64	1.8
$^{54}Fe^{16}O^-$	70	2.4
$^{56}Fe^{16}O^-$	72	1.9
$^{56}Fe^{32}S^-$	88	1.9

Tab. 4.6: Ratio $r_{\mathrm{MS}} := \frac{\Delta M_{\mathrm{FWHM}}}{\Delta S_{\mathrm{FWHM}}}$ of the full width at half maximum of the peaks from the mass spectra of measurement (Fig. 4.13) and simulation (Fig. 4.11). The uncertainty of r_{MS} is around 30%.

mum, from:

$$\Delta M_{\mathrm{FWHM}} = r_{\mathrm{MS}} \cdot \Delta S_{\mathrm{FWHM}}, \tag{4.16}$$

it can be concluded:

$$\left(\frac{\Delta m}{m}\right)_{\mathrm{M}} = r_{\mathrm{MS}} \cdot \left(\frac{\Delta m}{m}\right)_{\mathrm{S}}. \tag{4.17}$$

The resolution depends on the slit width w_o, on the beam energy distribution and other effects, like charge repulsion between the ions and errors in the geometry of our experimental setup. All effects, except the slit width w_o, are summarized to an effective energy spread. With this definition and with $\Delta m/m = w_{\mathrm{o}}/\rho + \Delta E/E$ (see Sec. 2.2.4) we can determine the effective energy spread:

$$\left(\frac{w_o}{\rho} + \frac{\Delta E}{E}\right)_{\mathrm{M}} = r_{\mathrm{MS}} \cdot \left(\frac{w_o}{\rho} + \frac{\Delta E}{E}\right)_{\mathrm{S}}, \tag{4.18}$$

$$\Rightarrow \quad \frac{w_o}{\rho} + \frac{\Delta E_{\mathrm{M}}}{E} = r_{\mathrm{MS}} \cdot \left(\frac{w_o}{\rho} + \frac{\Delta E_{\mathrm{S}}}{E}\right), \tag{4.19}$$

$$\Rightarrow \quad \Delta E_{\mathrm{M}} = (r_{\mathrm{MS}} - 1) \cdot \frac{w_o}{\rho} \cdot E + r_{\mathrm{MS}} \cdot \Delta E_{\mathrm{S}}. \tag{4.20}$$

With the values from above and $r_{\mathrm{MS}} = 2.25(61)$, for the measured effective energy spread we find:

$$\Delta E_{\mathrm{M}} = 27.2(7.2)\ \mathrm{eV}. \tag{4.21}$$

To find an approximate value for the real energy uncertainty of the ion beam, we assume that the resolving power only depends on the slit width and the beam energy distribution, and neglect all other effects that can influence the mass resolution. Furthermore, we assume that the energy distribution of the real beam is a Gaussian distribution like that in the simulation (the full width at half maximum in the simulation is 1 eV). With these assumptions, the full width at half maximum of the Gaussian distribution of the real beam is 27.2(7.2) eV. This yields a surface temperature in the order of 10^5 K. The measured energy spread is much too high for a thermal energy distribution of the ions emitted from the target surface. The ions must suffer an energy transfer from the primary particle bombardment that is mainly responsible for the energy spread of the beam.

With the measured effective energy spread of the ion beam we can calculate the maximum resolving power of the mass separation configuration. The maximum reachable mass resolution is obtained when the slit width is zero. With this condition ($w_o \stackrel{!}{=} 0$) we find:

$$\frac{m}{\Delta m} = \frac{E}{\Delta E}, \tag{4.22}$$

$$= \frac{5000 \text{ eV}}{27.2(7.2) \text{ eV}}, \tag{4.23}$$

$$= 184(49). \tag{4.24}$$

That means that even if the slit width is decreased, it is probably not quite possible to generate an isotopically pure $^{192}Os^-$ beam, since for a successful separation a resolving power of at least 192 is necessary. If a successful separation were possible, the beam current would probably be rather low since the slit width must probably be small, which results in a low transmission.

With the present beam quality, and with the present mass separation configuration with a slit width w_o of 2 mm a mass resolution of about 100 was measured. It should therefore be possible to generate a beam which consists of mainly $^{192}Os^-$, and smaller fractions of $^{190}Os^1H^-$ and $^{192}Os^1H^-$.

5. CONCLUSION

The present measurements and their detailed analysis show that the experimental setup works as designed. Further optimization might yield a slightly better transmission and resolving power. It should be noted that the beam line was operated for the first time when the mass spectrum was measured. A further increase of the beam transmitted through the mass separation system could be achieved in a further optimization of the voltages of the beam line components. Possibly an additional steerer could be added to the beam line and positioned behind the einzel lens in order to correct the beam direction and enhance the transmission in that section of the apparatus.

Moreover, it can be concluded that the resolving power of the present mass separation is around 100. The maximum resolving power that can in principle be reached with our setup, by decreasing the slit width, is measured to be 184(49). However, the generation of a rather pure $^{192}\mathrm{Os}^-$ beam requires a resolving power of at least 192. Further measurements should be conducted with a platinum target in order to determine the resolving power in a mass range close to that of $^{192}\mathrm{Os}^-$. If the platinum isotopes can be separated, the mass resolving power must be at least as high as that which is necessary for a successful osmium separation.

The resolving power can be further increased by decreasing the slit width and correcting possible geometrical misalignments, especially the positions of the slits. It may also be possible to decrease the energy spread of the beam by applying energy selective elements prior to the mass separator. Decreasing the sputter energy could have an energy spread decreasing effect on the ion beam but would of course also decrease the beam current. Yet another solution would be to increase the beam energy and decelerate the beam behind the mass separator, which could be achieved with time dependent electromagnetic fields.

As mentioned above, it should nevertheless be possible to generate a beam consisting mainly of $^{192}\mathrm{Os}^-$, with only small fractions of $^{190}\mathrm{Os}^1\mathrm{H}^-$ and $^{192}\mathrm{Os}^1\mathrm{H}^-$ without any changes to the setup. I estimate that if the beam line is finally optimized it should be possible to generate such an osmium ion beam of a few hundred nA beam current.

A. MATRIX FORMALISM OF ION OPTICAL ELEMENTS

A.1 Drift space

In field free regions no forces act on particles. Hence, the momentum and thus p_r and r' are constant. The motion of all particles is along straight trajectories. The position r increases linearly with the drift length L and is proportional to the transverse momentum p_r (or r'). After the drift length L, the phase space coordinates $(r_1,\, r_1')$ are transformed into $(r_2,\, r_2')$:

$$\begin{pmatrix} r_2 \\ r_2' \end{pmatrix} = \begin{pmatrix} 1 & L \\ 0 & 1 \end{pmatrix} \cdot \begin{pmatrix} r_1 \\ r_1' \end{pmatrix} . \tag{A.1}$$

In Fig. A.1 an emittance diagram is shown in which the shape of an elliptical phase space changes while the particle beam moves along a drift space. For every point in the diagram, the coordinate r' is constant and so the transformation of every coordinate is parallel to the r-axis. The change of r is proportional to the corresponding r' and the transformation can be considered as a shearing action parallel to the r-axis. In particular, points on the r-axis ($r' = 0$), *i.e.* particles moving parallel to the z-direction or main direction of the beam, are not transformed by drift spaces.

A.2 Thin lens

The action of a thin lens on a point (r_1, r_1') in phase space is given by the linear transformation:

$$\begin{pmatrix} r_2 \\ r_2' \end{pmatrix} = \begin{pmatrix} 1 & 0 \\ -1/f & 1 \end{pmatrix} \cdot \begin{pmatrix} r_1 \\ r_1' \end{pmatrix} , \tag{A.2}$$

where f is the focal length of the lens. By this transformation for every point (r, r'), r remains constant, while the transverse momentum, *i.e.* r', is changed by $\Delta r'$, which is proportional to the distance r from the beam center (z-axes). This can be seen in Fig. A.2. Especially points in the r'-axis ($r = 0$) are not changed by this transformation. The transformation can be considered as a shearing action on the area parallel to the r'-axis.

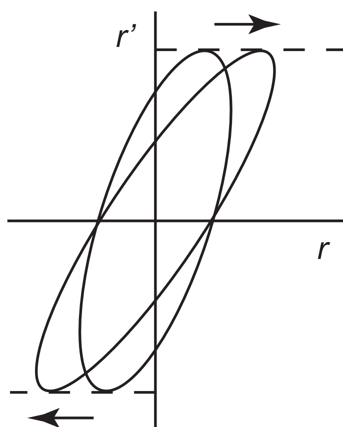

Fig. A.1: Influence on the emittance by a drift space.

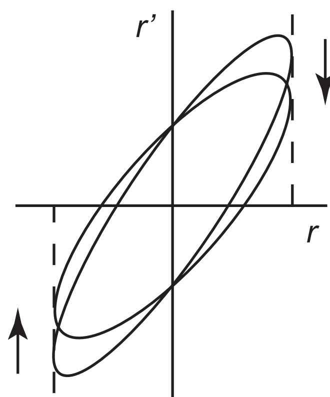

Fig. A.2: Influence on the emittance by a thin lens.

A.3 Examples

Figure A.3 shows how the shape of the emittance of a beam changes while it traverses a beam line consisting of a thin lens and two drift spaces. If a beam passes a drift space, from the instantaneous shape of the beam emittance one can conclude whether the beam is convergent, divergent or at a focus. Figure A.4 is an example for these situations.

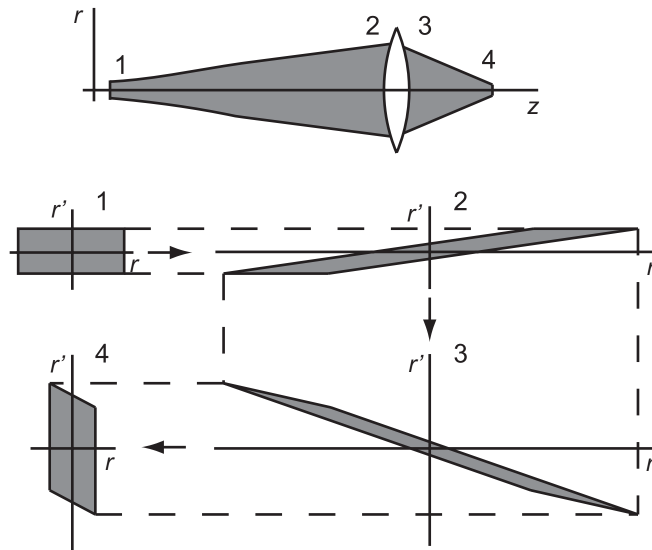

Fig. A.3: Change of emittance shape, while a beam is flying through a drift space, a thin lens and a second drift space until it is focused. (Adapted from Ref. [25].)

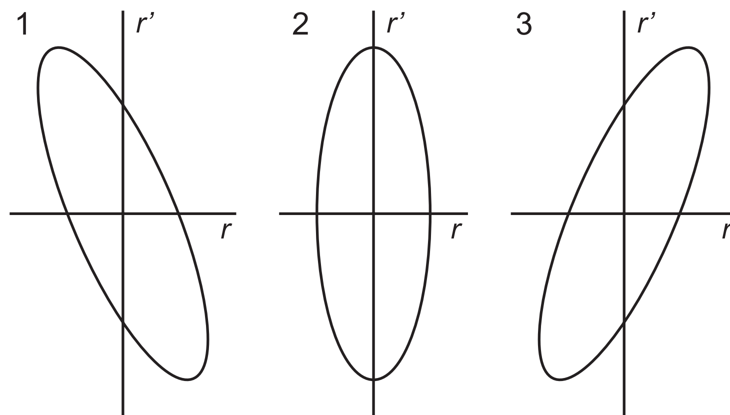

Fig. A.4: Emittance diagrams with emittance ellipses. In 1) the beam is convergent (prior focus), in 2) at a focus and in 3) it is divergent (after focus).

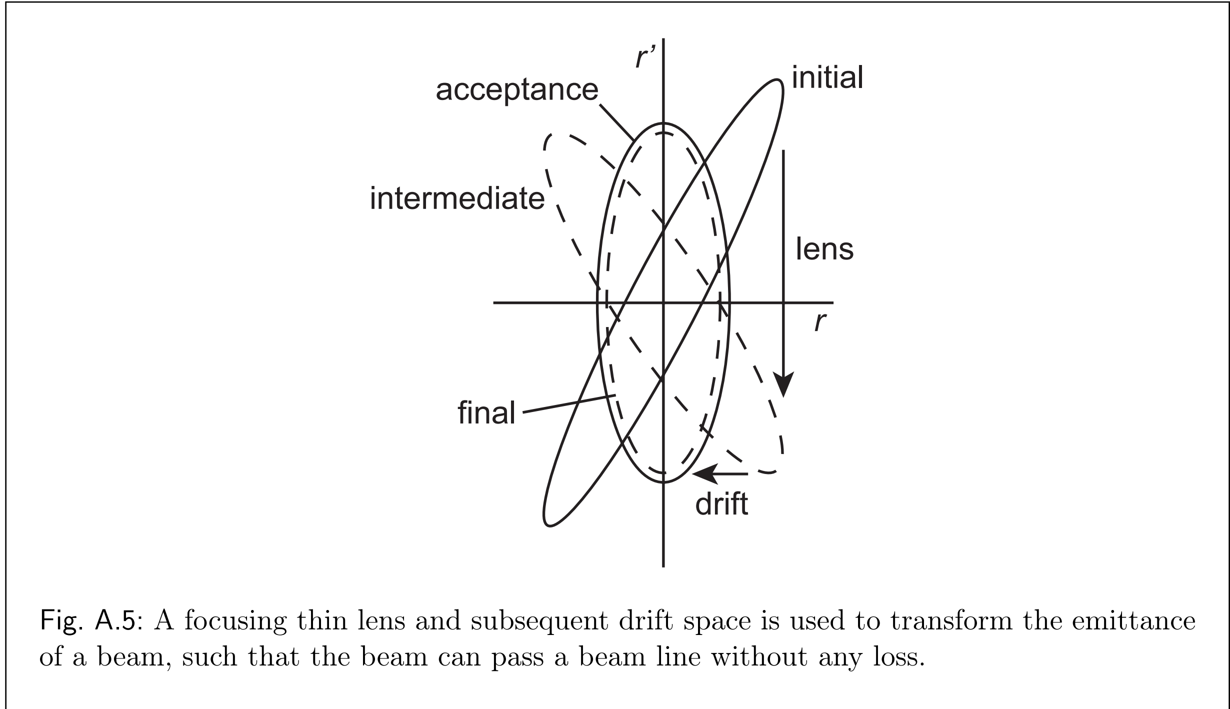

Fig. A.5: A focusing thin lens and subsequent drift space is used to transform the emittance of a beam, such that the beam can pass a beam line without any loss.

A.4 Acceptance

The acceptance A of a beam line is defined as the maximum possible emittance that can pass it without any loss, *i.e.* $A = \epsilon_{\text{max}}$. The acceptance can of course be displayed in an emittance diagram as well. This is done in Fig. A.5. A beam whose emittance does not fall completely inside the acceptance area suffers a beam loss. All parts outside the acceptance are cut off. With the help of ion optical elements, a beam can be transformed in such a way that a maximum beam, or if possible even the whole beam, is able to pass the beam line.

A.5 Einzel lens

An einzel lens is an axially symmetric ion optical element. It is used immediately behind ion sources in order to focus a divergent ion beam. Figure A.6 shows a sectional view of an einzel lens with its geometrical parameters R, d and h, and the electrostatic potential $V(z)$ along the z-axis (symmetry axis). Further parameters are the beam energy and the voltages on the electrodes. Usually the voltage U_1 is set to ground, such that in this case only U_2 can be considered as a parameter to control the focal length of the einzel lens. Figure A.7 shows a schematic view of typical ion trajectories, where in reality the distance from the z-axis is much smaller. $x_1(z)$ is an ion trajectory that belongs to a parallel beam

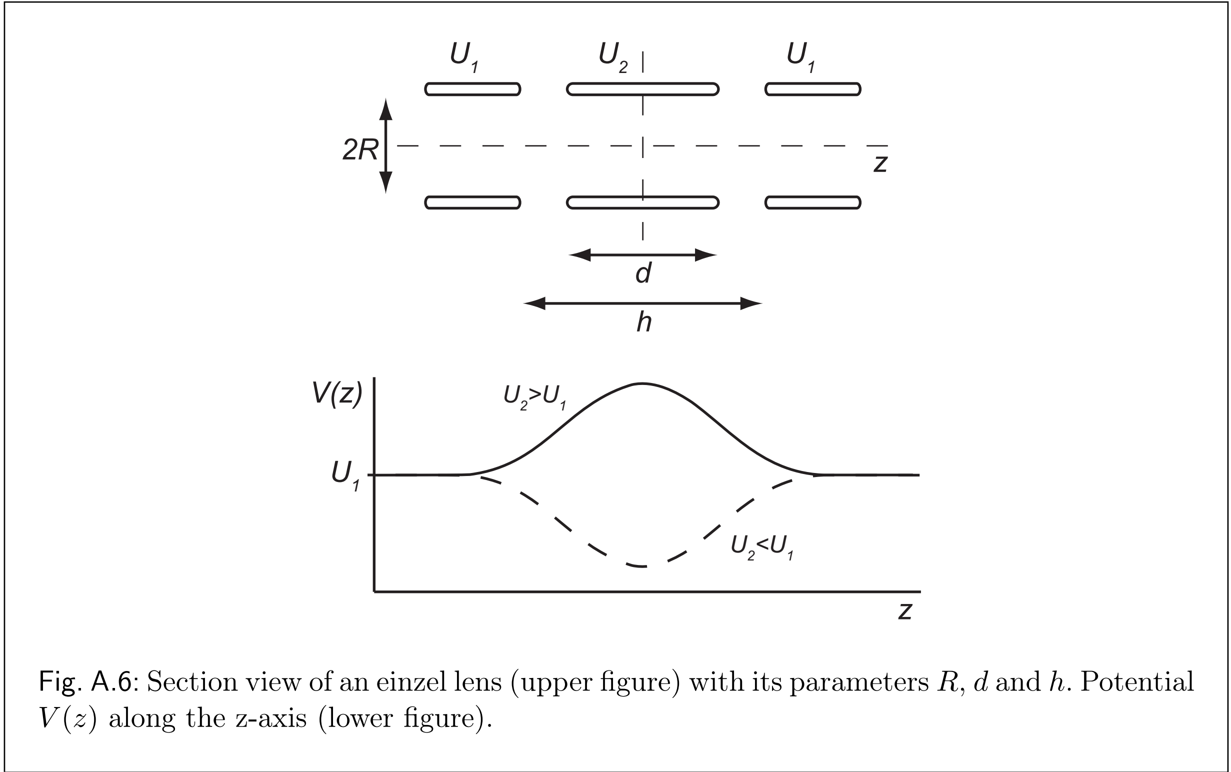

Fig. A.6: Section view of an einzel lens (upper figure) with its parameters R, d and h. Potential $V(z)$ along the z-axis (lower figure).

prior to the einzel lens. All particles of this beam are focused to the focal point behind the einzel lens. The trajectory x_2, in contrast, belongs to a particle of a beam that is focused in the focal point prior the lens. This beam is transformed into a parallel beam behind the lens. The planes H_1 and H_2 are at positions z where the linear trajectories in the field free region in front of and behind the lens intersect, if they are lengthened (dashed lines). The analogon of an einzel lens in the light optics is a thick lens. Figure A.8 shows a thick lens with rays connecting an object and an image. A thick lens is optically identical with a thin lens, but the length of the beam line is the distance of $L - z_1 - z_2$ longer (Fig. A.9). The transformation of a point (r_1, r_1') in phase space for a particle in front of an einzel lens or a thick lens in general to a point behind the lens can be written as:

$$\begin{pmatrix} r_2 \\ r_2' \end{pmatrix} = \begin{pmatrix} 1 - z_2/f & z_1 + z_2 - z_1 z_2/f \\ -1/f & 1 - z_1/f \end{pmatrix} \cdot \begin{pmatrix} r_1 \\ r_1' \end{pmatrix} . \tag{A.3}$$

This transformation can be considered as the product of the transformation of a drift space with length z_1, the transformation of a thin lens with focal length f, and the transformation of a second drift space with length z_2 (Fig. A.9):

$$\begin{pmatrix} 1 - z_2/f & z_1 + z_2 - z_1 z_2/f \\ -1/f & 1 - z_1/f \end{pmatrix} = \begin{pmatrix} 1 & z_2 \\ 0 & 1 \end{pmatrix} \cdot \begin{pmatrix} 1 & 0 \\ -1/f & 0 \end{pmatrix} \cdot \begin{pmatrix} 1 & z_1 \\ 0 & 1 \end{pmatrix} . \tag{A.4}$$

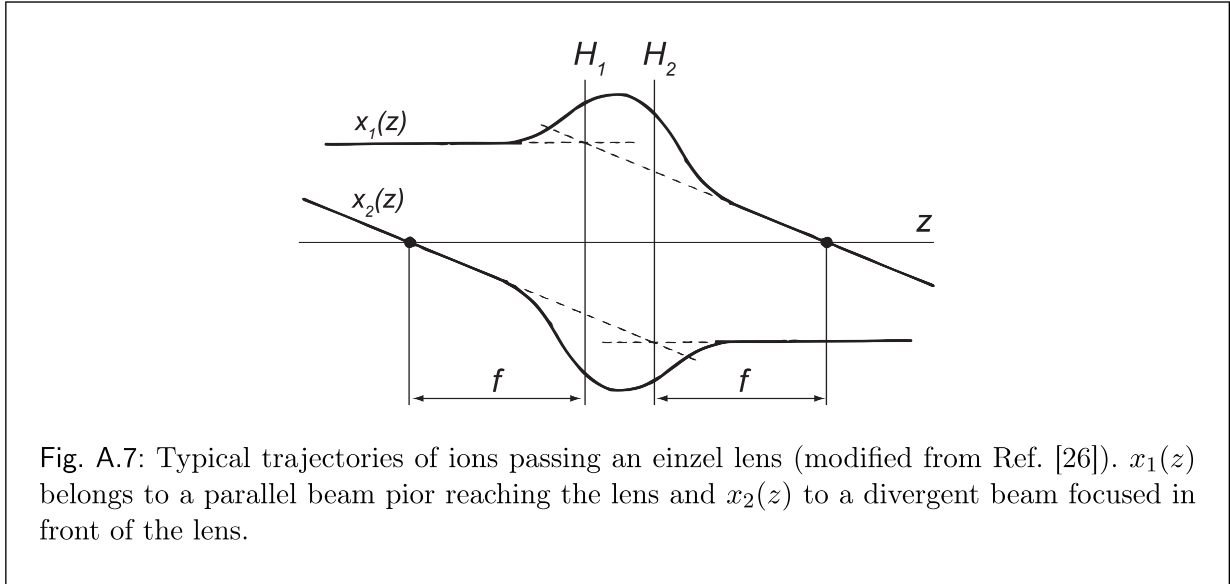

Fig. A.7: Typical trajectories of ions passing an einzel lens (modified from Ref. [26]). $x_1(z)$ belongs to a parallel beam pior reaching the lens and $x_2(z)$ to a divergent beam focused in front of the lens.

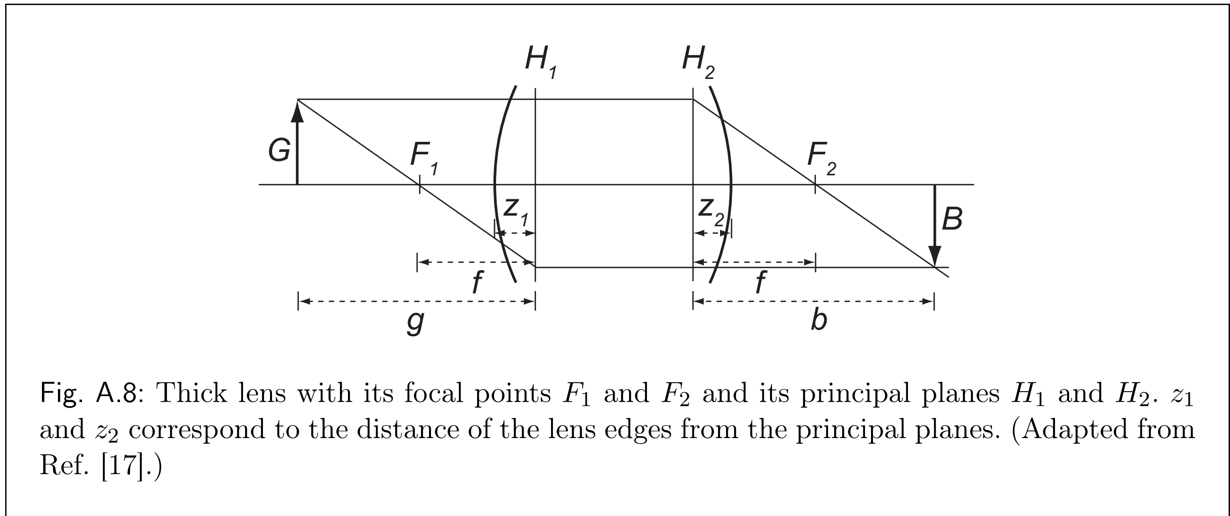

Fig. A.8: Thick lens with its focal points F_1 and F_2 and its principal planes H_1 and H_2. z_1 and z_2 correspond to the distance of the lens edges from the principal planes. (Adapted from Ref. [17].)

In the symmetric case, like in Fig. A.6, $z_1 = z_2$ applies. In most cases it is impossible to find exact values of the matrix elements, *i.e.* f, z_1 and z_2, of an einzel lens. In general they have to be calculated numerically or found experimentally. An approximation helping us finding the matrix elements is the paraxial ray equation. It is a time independent differential equation for the trajectory $x(z)$ of particles passing axially symmetric potentials close to the symmetry axis. Some other methods for finding (numerical) approximations for the matrix elements of the transformation matrix of an einzel lens can be found in Refs. [17] and [26]. It should be noted that it is often not necessary to know exact values of the matrix elements, since during operation the voltage of the central electrode can be tuned in order to find an optimal value for the focal length.

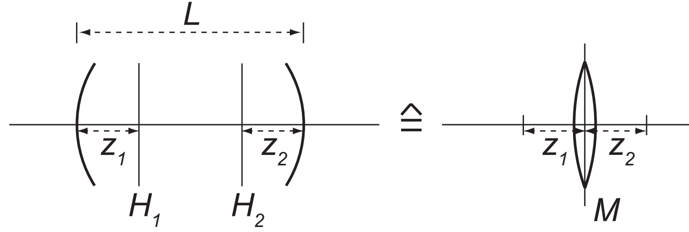

Fig. A.9: A thick lens can be considered as a thin lens with an additional length $L - z_1 - z_2$, that has no optical effect on the beam passing it. (Adapted from Ref. [17].)

In the approximation of the paraxial ray equation, the trajectory $x(z)$ is depends upon the potential $V(z)$ along the symmetry axis, while it is independent on off-axis potentials. With estimations of the potential along the axis, the trajectory $x(z)$ can be approximated and so values of the focal length f and the other matrix elements of an einzel lens can be found.

For a cylindrical symmetry the potential function V, *i.e.* the solution of the Laplace equation $\Delta V = 0$, can be expanded into a Taylor series that in cylinder coordinates is given by:

$$V(r, \phi, z) = V(r = 0, z) - \frac{r^2}{4} V''(r = 0, z) + \cdots, \tag{A.5}$$

where $V'' = \partial^2 V / \partial z^2$. Because of the symmetry it is independent of the azimuthal angle ϕ. In Cartesian coordinates this yields:

$$V(x, y, z) = V(z) - \frac{x^2 + y^2}{4} V''(z) + \cdots, \tag{A.6}$$

where $V(z) := V(0, 0, z)$. This means that if the potential is known along the z-axis the potential in its vicinity can be numerically calculated from it. Because of the rotational symmetry we obtain $\partial V / \partial x = \partial V / \partial y$. We therefore only consider x since the equations of motion are identical for x and y. From the previous equation we find in linear approximation:

$$\frac{\partial V}{\partial x}(x, y, z) \approx -\frac{x}{2} V''(z). \tag{A.7}$$

For small distances from the z-axis (x and y) we can also conclude:

$$\frac{\partial V}{\partial z}(x, y, z) \approx \frac{\partial V(z)}{\partial z}. \tag{A.8}$$

These approximations and $m\ddot{\vec{x}} = q\vec{E} = -q\vec{\nabla}V$ yield:

$$m\ddot{x} = -q\frac{\partial V}{\partial x} \approx q\frac{x}{2}V''(z), \tag{A.9}$$

$$m\ddot{z} = -q\frac{\partial V}{\partial z} \approx -qV'(z). \tag{A.10}$$

With $v_z = dz/dt$ we find:

$$\frac{d}{dt} = v_z\frac{d}{dz}, \tag{A.11}$$

$$\dot{x} = v_z x'. \tag{A.12}$$

Plugging this into Eq. (A.9) yields:

$$\frac{d}{dt}(mv_z x') = q\frac{x}{2}V''(z), \tag{A.13}$$

and

$$x'\frac{d}{dt}(mv_z) + (mv_z)\frac{d}{dt}x' = q\frac{x}{2}V''(z). \tag{A.14}$$

With Eqs. (A.10) and (A.11) we find:

$$x'[-qV'(z)] + mv_z^2 x'' = q\frac{x}{2}V''(z). \tag{A.15}$$

The approximation $\frac{1}{2}mv_z^2 \approx \frac{1}{2}mv^2 = E_{\text{kin}} \approx E - V(z)$ yields a linear approximation of the paraxial ray equation:

$$x'' - \frac{q\ V'(z)}{2[E - V(z)]}x' - \frac{q\ V''(z)}{4[E - V(z)]}x = 0, \tag{A.16}$$

where E is the particle or beam energy. No constant term nor a higher derivative than x'' occur in this equation.

A.6 Electrostatic quadrupole

Figure A.10 shows an example of an electrostatic quadrupole, where ion beams propagate along the z-direction. A sectional view of an electrostatic quadrupole and an ion trajectory is shown in Fig. A.11, where the quadrupole in this example is focusing in the sectional plane of the figure. An ideal electrostatic quadrupole has hyperbolically shaped electrodes. Since the production of hyperbolically shaped electrodes is rather trying compared to cylindrically shaped ones the hyperbola is often approximated by a circle. It turns out that the best approximation is obtained if the radius of the electrodes is ≈ 1.147 times the

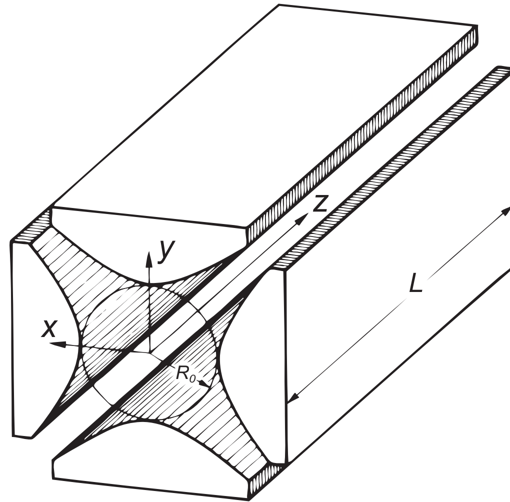

Fig. A.10: Sketch of a typical electrostatic quadrupole with aperture radius R_0 and geometrical parameter L. From Ref. [11].

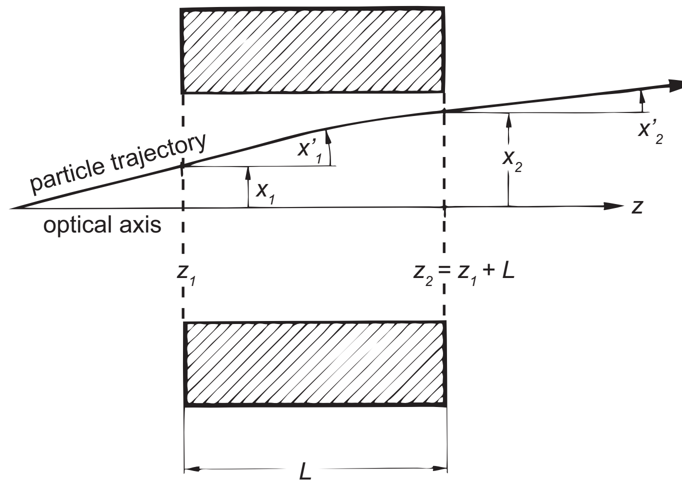

Fig. A.11: Sectional view of an electrostatic quadrupole. A typical ion trajectory is shown. (Adapted from Ref. [11].)

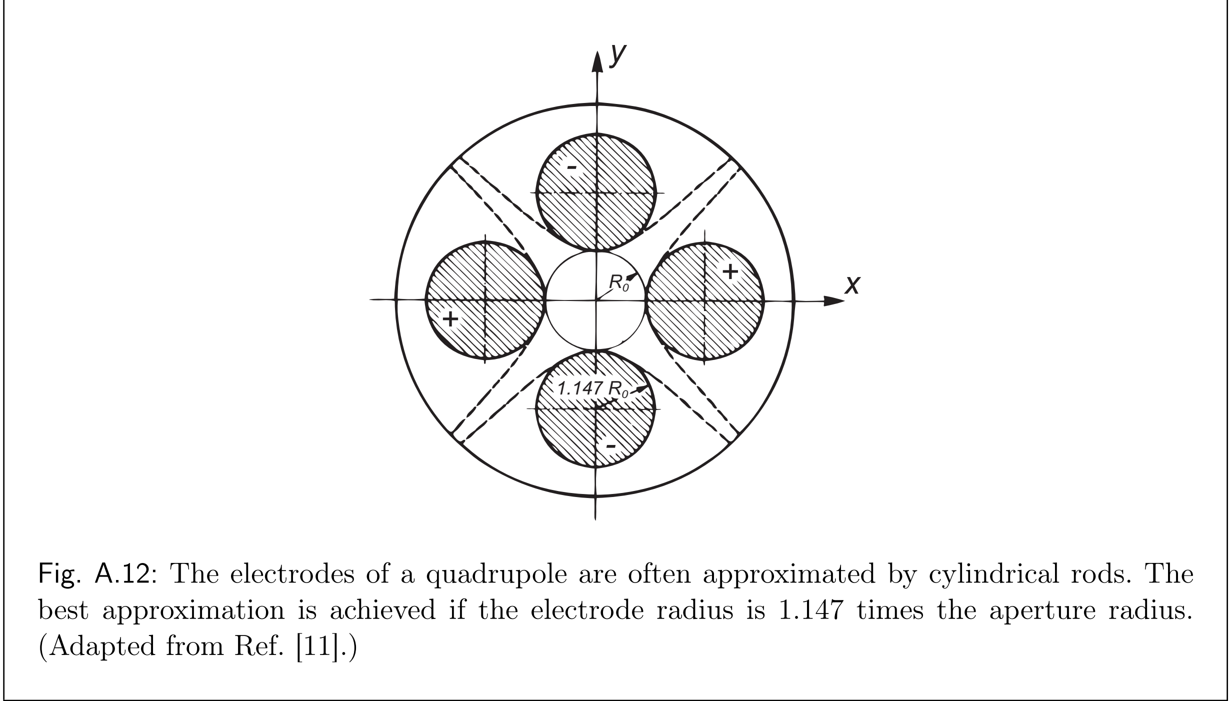

Fig. A.12: The electrodes of a quadrupole are often approximated by cylindrical rods. The best approximation is achieved if the electrode radius is 1.147 times the aperture radius. (Adapted from Ref. [11].)

aperture radius (Fig. A.12). The approximation is only valid close to the z-axis. The beam profile should not exceed half the aperture of the quadrupole in order to maintain a good quadrupole approximation.

An electrostatic quadrupole is an ion optical element that transforms the emittance ϵ_x in the (x, x')-space and the emittance ϵ_y in the (y, y')-space in a different way. It can therefore, for example, change an axially symmetric transverse beam profile [in the (x, y)-plane] into an asymmetric beam profile and vice versa. A quadrupole always focuses in one transverse direction, while it defocuses in the other (perpendicular) transverse direction (Fig. A.13).

The transformations of an ideal electrostatic quadrupole with no fringe field effects, for positive ions, focusing in the (x, z)-plane and defocusing in the (y, z)-plane (Fig. A.13) are given by

$$\begin{pmatrix} x_2 \\ x_2' \end{pmatrix} = \begin{pmatrix} \cos(kL) & k^{-1}\sin(kL) \\ -k\sin(kL) & \cos(kL) \end{pmatrix} \cdot \begin{pmatrix} x_1 \\ x_1' \end{pmatrix}, \tag{A.17}$$

$$\begin{pmatrix} y_2 \\ y_2' \end{pmatrix} = \begin{pmatrix} \cosh(kL) & k^{-1}\sinh(kL) \\ k\sinh(kL) & \cosh(kL) \end{pmatrix} \cdot \begin{pmatrix} y_1 \\ y_1' \end{pmatrix}, \tag{A.18}$$

where (x_1, x_1') and (y_1, y_1') are positions in phase space at the quadrupole entrance (z_1), and (x_2, x_2') and (y_2, y_2') are their transformations at the quadrupole exit $z_2 = z_1 + L$. The quantity L is the quadrupole's length. The parameter k is given by $k \approx 1/R_0\sqrt{V_0/U}$,

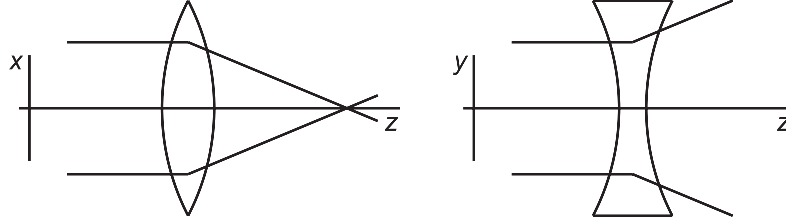

Fig. A.13: A quadrupole focuses in one plane [in this example (x, z)-plane on the left side of the figure], while it defocuses in the perpendicular direction [here (y, z)-plane on the right side].

where $\pm V_0$ is the potential on the electrodes, R_0 is aperture radius, and U is the beam acceleration voltage, *i.e.* qU corresponds to the beam energy.

If the sign of the electrode potentials is inverted, or if the sign of the ion charge is inverted, the quadrupole defocuses in the (x, z)-plane and focuses in the (y, z)-plane. The transformations above are then still valid, if (x, x') and (y, y') are substituted by each other.

In an ideal electrostatic quadrupole the electrical potential is given by:

$$V(x, y) = \frac{x^2 - y^2}{R_0^2} V_0. \tag{A.19}$$

Since $\vec{E} = -\vec{\nabla} V$ the electric field can be calculated as follows:

$$E_x = -\frac{\partial V}{\partial x} = -\frac{2V_0}{R_0^2} x, \tag{A.20}$$

$$E_y = -\frac{\partial V}{\partial y} = \frac{2V_0}{R_0^2} y, \tag{A.21}$$

$$E_z = 0, \tag{A.22}$$

which yields the equations of motion:

$$m\ddot{x} = -q\frac{2V_0}{R_0^2} x, \tag{A.23}$$

$$m\ddot{y} = -q\frac{2V_0}{R_0^2} y. \tag{A.24}$$

With the substitutions:

$$\ddot{x} = \frac{d^2 x}{dz^2} \left(\frac{dz}{dt} \right)^2 = x'' v_z^2, \tag{A.25}$$

$$\ddot{y} = \frac{d^2 y}{dz^2} \left(\frac{dz}{dt} \right)^2 = y'' v_z^2, \tag{A.26}$$

the equations of motion can be transformed into

$$x'' = -k^2 x, \tag{A.27}$$

$$y'' = +k^2 y, \tag{A.28}$$

where $k^2 = 2qV_0/R_0^2 m v_z^2 \approx V_0/R_0^2 U$. $E = q \cdot U$ is the beam energy given by the acceleration voltage U of the particles.

The general solutions of these differential equations are:

$$x(z) = a \cdot \cos(kz) + b \cdot \sin(kz), \tag{A.29}$$

$$y(z) = c \cdot \cosh(kz) + d \cdot \sinh(kz), \tag{A.30}$$

where a, b, c and d are undetermined coefficients. From this, with $x' = dx/dz$ and $y' = dy/dz$, we obtain:

$$x'(z) = -a \cdot k \cdot \sin(kz) + b \cdot k \cdot \cos(kz), \tag{A.31}$$

$$y'(z) = c \cdot k \cdot \sinh(kz) + d \cdot k \cdot \cosh(kz). \tag{A.32}$$

If the positions $x_1 = x(z_1)$ and $y_1 = y(z_1)$, and the directions $x_1' = x'(z_1)$ and $y_1' = y'(z_1)$ are known for a single value of z_1, those for other values of z can be calculated by the prior equations, since the coefficients can then be determined. Therefore, we find:

$$x(z) = x_1 \cdot \cos(kz) + x_1' \cdot k^{-1} \cdot \sin(kz), \tag{A.33}$$

$$x'(z) = -x_1 \cdot k \cdot \sin(kz) + x_1' \cdot \cos(kz), \tag{A.34}$$

$$y(z) = y_1 \cdot \cosh(kz) + y_1' \cdot k^{-1} \sinh(kz), \tag{A.35}$$

$$y'(z) = y_1 \cdot k \cdot \sinh(kz) + y_1' \cosh(kz). \tag{A.36}$$

These transformations are mainly of interest for positions and directions that are transformed from the entrance ($z_1 = 0$) to the exit ($z_2 = L$) of the quadrupole. This yields the transformations given in Eqs. (A.17) and (A.18).

A.7 Magnetic sector lens

Suppose we have a volume with a homogeneous magnetic field $\vec{B}$ pointing in the y-direction (Fig. A.14). Ions moving in the y-direction are not influenced by this field since only ions with a velocity component perpendicular to the magnetic field feel a force. Ions moving in the (x, z)-plane inside the magnetic field travel on circular trajectories (Fig. A.15) with Larmor radius

$$\rho = \frac{\gamma m v}{qB}, \tag{A.37}$$

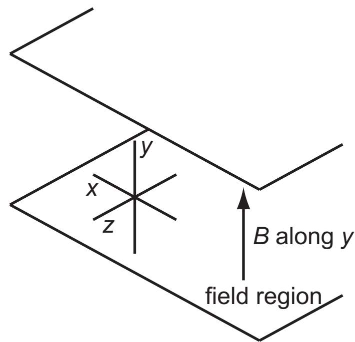

Fig. A.14: An ideal B field (without fringe fields), pointing in the y-direction, is confined to a volume between two planes. The coordinate systems applies to particles propagating into the z-direction, which enter the field region perpendicularly.

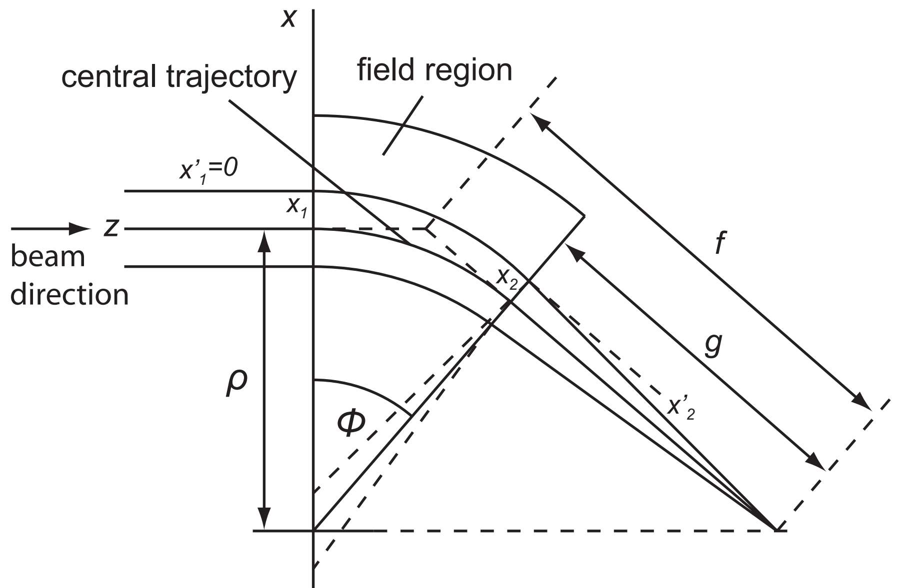

Fig. A.15: A parallel ion beam is focused [only in the (x, z)-plane] to a point at a distance g from the field boundary. (Adapted from Ref. [27].)

where m is the particle's rest mass, v its velocity, q its charge, and $\gamma = 1/\sqrt{1-(v/c)^2}$. If convenient, in non-relativistic approximation, $\gamma = 1$ can be assumed.

Since the radius depends on the ion momentum, magnetic sector lenses can be used for momentum analysis. A magnetic sector lens acts as a thick lens in the x-direction (transverse direction of the beam propagation perpendicular to the B field direction) and as a drift space in the y-direction. The focusing effect in the x-direction is caused by a correlation between path length inside the sector magnet and transverse position x, as is shown in Fig. A.15. Remember that x is the transverse distance from the main beam axis (z-axis). While the ions pass the magnetic sector field which extends over an angle ϕ, the direction of the main beam axis changes. The coordinate system indicated in the figure (x- and z-axis) refers to the moment the beam arrives at the field region and is identical to that of Fig. A.14. In Fig. A.15 a parallel beam ($x'_1 = 0$) entering the magnetic field region is transformed into a convergent beam ($x'_2 < 0$) leaving the field region. From Fig. A.15 it can be derived that:

$$x_2 = x_1 \cos\phi, \tag{A.38}$$

and

$$x'_2 = -\frac{x_1}{\rho}\sin\phi. \tag{A.39}$$

The complete transformation in the x-direction of an ideal magnetic sector field lens, containing these relations, is given by:

$$\begin{pmatrix} x_2 \\ x'_2 \end{pmatrix} = \begin{pmatrix} \cos(\phi) & \rho\sin(\phi) \\ -\frac{1}{\rho}\sin(\phi) & \cos(\phi) \end{pmatrix} \cdot \begin{pmatrix} x_1 \\ x'_1 \end{pmatrix}. \tag{A.40}$$

A more detailed derivation of this transformation can be found in Ref. [11]. Two important quantities are the focal length f

$$f = \frac{\rho}{\sin\phi}, \tag{A.41}$$

and the distance g of the focal plane from the field edge

$$g = \frac{\rho}{\tan\phi}. \tag{A.42}$$

In the y-direction the transformation of an ideal magnetic sector field is equal to that of a drift space with length $\phi \cdot \rho$. It is given by:

$$\begin{pmatrix} y_2 \\ y'_2 \end{pmatrix} = \begin{pmatrix} 1 & \phi\cdot\rho \\ 0 & 1 \end{pmatrix} \cdot \begin{pmatrix} y_1 \\ y'_1 \end{pmatrix}. \tag{A.43}$$

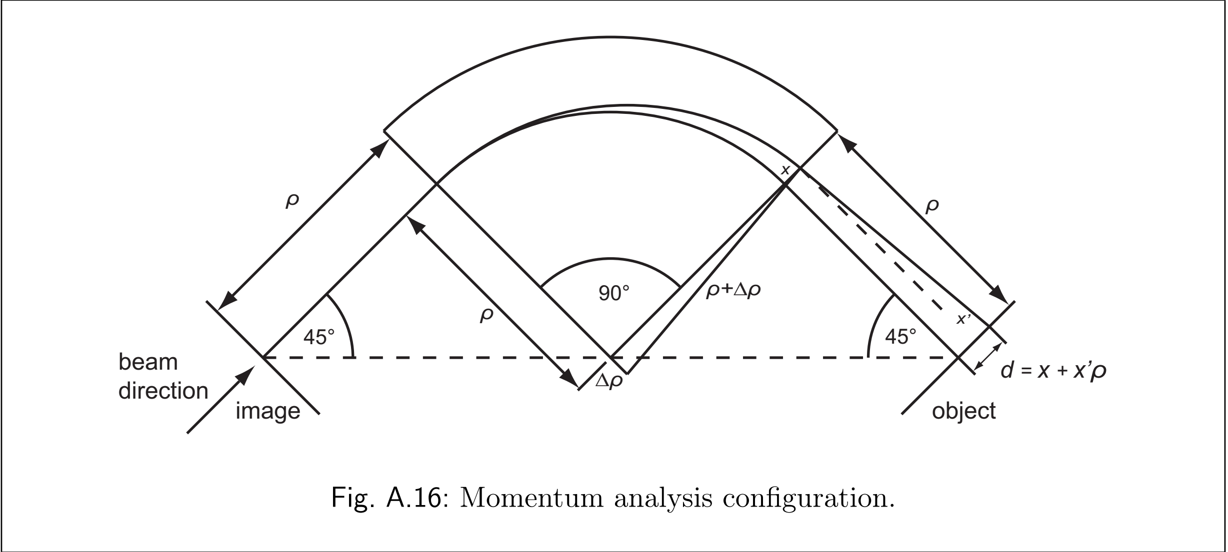

Fig. A.16: Momentum analysis configuration.

A.8 Derivation of mass resolution

Figure A.16 gives a schematic overview of the mass separation configuration used in our setup. The beam trajectory that has a symmetric shape in the figure is that of an ion of the desired momentum. The Larmor radius of this ion is given by

$$\rho = \frac{1}{qB} \cdot p, \tag{A.44}$$

where p is the ion's momentum, q its charge and B the magnetic field strength inside the 90° sector. This radius can be considered as a fixed valued determined by the geometry of the momentum separation, while the desired momentum is chosen by tuning the magnetic field B. Two ions starting with the same direction and at the same position in the object plane but with a momentum difference Δp hit the image plane with a displacement d from each other, which is given by:

$$d = x + \rho \cdot x', \tag{A.45}$$

where x is the transverse distance between the two ion trajectories at the exit of the sector magnet and x' is the angular difference in their direction of flight at this position. From Fig. A.16 we find:

$$(\Delta\rho)^2 + (\rho + x)^2 = (\rho + \Delta\rho)^2, \tag{A.46}$$

where ρ is the Larmor radius of the ion with desired momentum p, and $\rho + \Delta\rho$ the Larmor radius of an ion whose momentum differs from the desired momentum by Δp. This yields for x:

$$x = \sqrt{\rho^2 + 2\rho \cdot \Delta\rho} - \rho, \tag{A.47}$$

and

$$x = \rho \left(\sqrt{1 + 2 \cdot \frac{\Delta\rho}{\rho}} - 1 \right). \tag{A.48}$$

Moreover, from Fig. A.16 we see that for the angle $\alpha \approx x'$, the ion trajectories differ from each other behind the sector magnet, we find:

$$\sin\alpha = \frac{\Delta\rho}{\rho + \Delta\rho}, \tag{A.49}$$

where α and x' are related by:

$$x' = \tan\alpha \approx \alpha. \tag{A.50}$$

The displacement of the two ions in the image plane is given by

$$d = x + \rho \cdot x'. \tag{A.51}$$

With the Eqs. (A.48),(A.49) and (A.50) we find:

$$d = \rho \left(\sqrt{1 + 2 \cdot \frac{\Delta\rho}{\rho}} - 1 + \tan\left[\arcsin\left(\frac{\Delta\rho}{\rho + \Delta\rho} \right) \right] \right). \tag{A.52}$$

For $\Delta\rho/\rho << 1$, the displacement d can be approximated by:

$$\begin{aligned} d &\approx \rho \left(\left[1 + \frac{\Delta\rho}{\rho} \right] - 1 + \frac{\Delta\rho}{\rho + \Delta\rho} \right), && \text{(A.53)} \\ &\approx \rho \left(\frac{\Delta\rho}{\rho} + \frac{\Delta\rho}{\rho + \Delta\rho} \right), && \text{(A.54)} \\ &\approx 2 \cdot \Delta\rho. && \text{(A.55)} \end{aligned}$$

We now consider the momentum of all ions as a function of ion mass and energy:

$$p = \sqrt{2mE}. \tag{A.56}$$

Now we assume that the ion energy is a constant and the ion mass is a variable, which would correspond to a monoenergetic beam, but with different ion mass components. Then Eq. (A.56) yields:

$$\frac{\Delta p}{p} = \frac{1}{2}\frac{\Delta m}{m}. \tag{A.57}$$

In addition we can conclude from Eq. (A.44):

$$\frac{\Delta\rho}{\rho} = \frac{\Delta p}{p} = \frac{1}{2}\frac{\Delta m}{m}. \tag{A.58}$$

If we plug this into Eq. (A.55), we find for a displacement d_m, caused by a relative mass difference $\Delta m/m$ and a monoenergetic beam:

$$d_m = \rho \frac{\Delta m}{m}. \tag{A.59}$$

For two ions of equal mass but where one has an additional energy δE compared to the other, we find for the displacement d_E caused by the relative energy difference $\delta E/E$:

$$d_E = \rho \frac{\delta E}{E}. \tag{A.60}$$

The configuration shown in Fig. A.16 has no magnification, *i.e.* the magnification equals one. The image of an object with expansion or width w_o has the same width as the object. The width w_o is defined by the distance between two silts. However, if we consider a beam with energy spread δE, which is defined here as half of the full width at half maximum ΔE of the beam energy distribution, the image is broadened by $\pm d_E$, so that its width is broadened to $w_\text{o} + 2d_E$. We now define that an image is resolvable if the distance between the centers of them is at least equal to their width. Then we find for an ion beam with different mass components and a relative energy spread $\delta E/E$ that the image of ions with relative mass difference $\Delta m/m$ is resolvable for

$$d_m \geq w_\text{o} + 2 \cdot d_E. \tag{A.61}$$

For an ions beam with an energy distribution, which has a maximum at E and a full width at half maximum ΔE, since $\Delta E = 2 \cdot \delta E$, we find that ions of this beam, of relative mass difference $\Delta m/m$ are resolvable if:

$$\frac{\Delta m}{m} \geq \frac{w_\text{o}}{\rho} + \frac{\Delta E}{E}. \tag{A.62}$$

Or we can say that the resolution $(m/\Delta m)_\text{max}$ of our configuration is given by:

$$\frac{m}{\Delta m} = \frac{1}{\frac{w_\text{o}}{\rho} + \frac{\Delta E}{E}}, \tag{A.63}$$

In this derivation it was neglected that the focal length is dependent on p. It was assumed that all images (for different mass and energy) are focused in the same image plane. This approximation is only valid for very small $\Delta p/p$.

A.9 Fringe field compensation

The magnetic field of an ideal bending magnet has a given value inside the gap volume and vanishes outside it. However, in real bending magnets, fringe fields occur. The upper

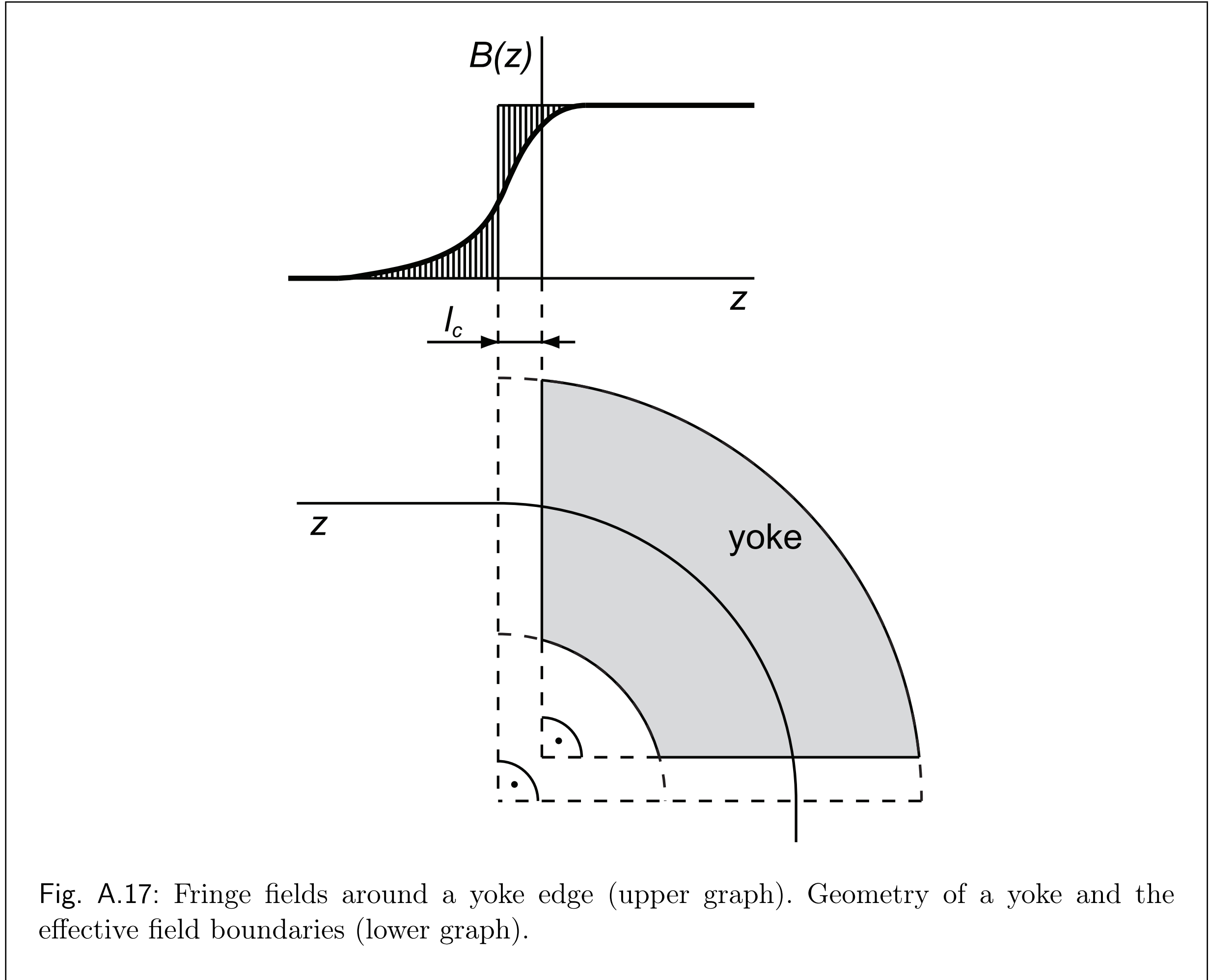

Fig. A.17: Fringe fields around a yoke edge (upper graph). Geometry of a yoke and the effective field boundaries (lower graph).

graph in Fig. A.17 shows how the magnetic field changes in the region of the edge of the yoke. The effective field boundary is at the position where the hashed regions on the left and right side of the effective field boundary have equal areas. This boundary is outside the gap volume, *i.e.* outside the bending magnet yoke. We now consider the volume inside the effective field boundaries as an approximation of the field expansion of an ideal bending magnet. Since the effective field boundaries are outside the yoke, the effective angle through which the ion trajectories are reflected, are larger than the section angle ϕ. To compensate for this, the yoke is cut by a length l_c (Fig. A.17, lower figure). Figure A.18 shows the measured dimensions (in units of mm) of a yoke of our bending magnet, with measurement uncertainties no larger than 0.5 mm. The gap height h_{G} of our bending magnet is 25 mm. The cutting length l_{c} was measured to about 12.5 mm, *i.e.* $l_{\mathrm{c}} \approx h_{\mathrm{G}}/2$. In our setup it was therefore assumed that the effective field boundaries are at the cutting length $l_{\mathrm{c}} = h_{\mathrm{G}}/2$ outside the yoke of the bending magnet. These assumptions

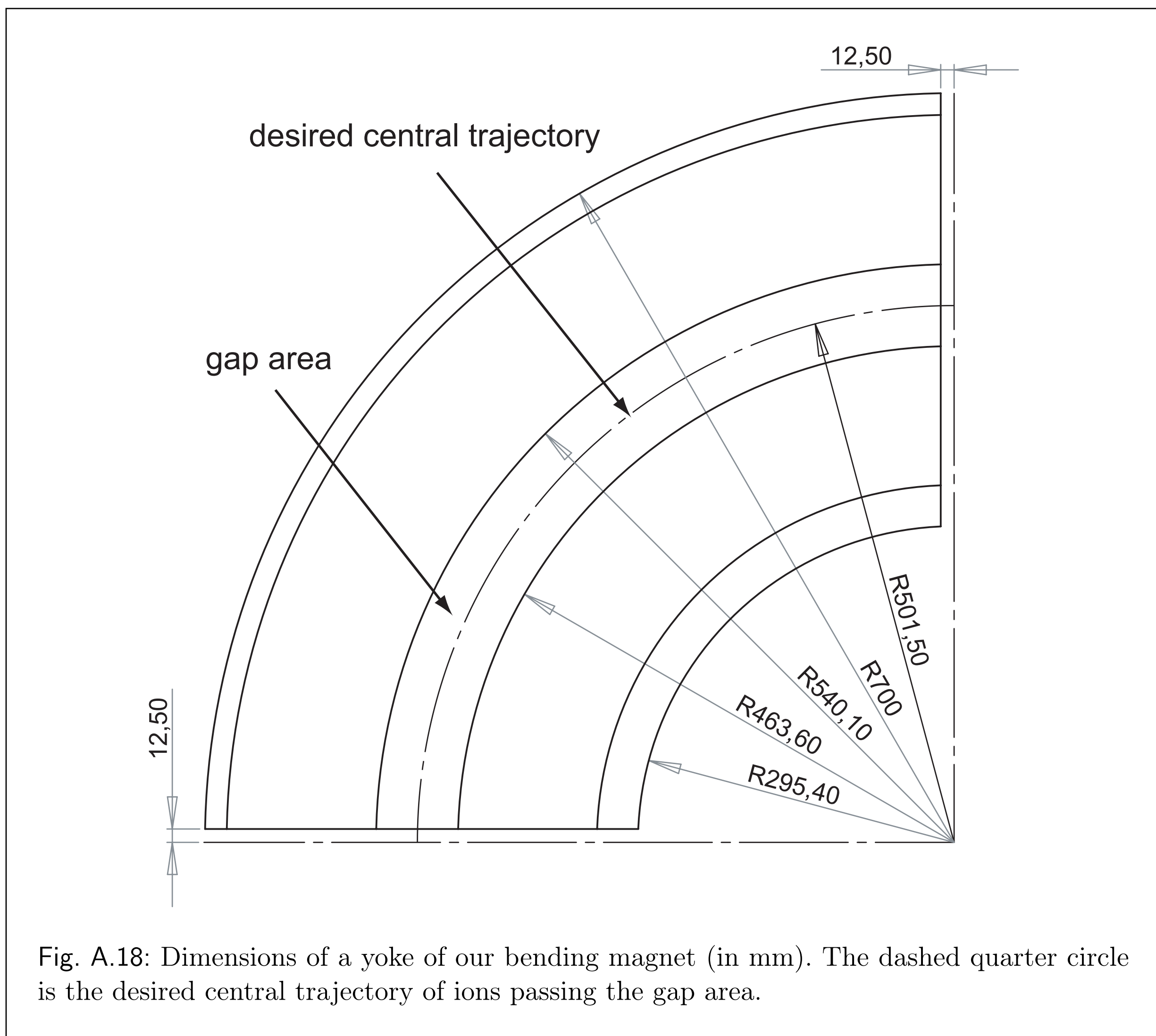

Fig. A.18: Dimensions of a yoke of our bending magnet (in mm). The dashed quarter circle is the desired central trajectory of ions passing the gap area.

worked very well in the simulation.

B. MISS OPERATING MANUAL

B.1 Start up

B.1.1 Target preparation

The target material (a few grams) must be tamped into the copper cup of the target holder. For this purpose a tamping tool is user to hammer the (metallic) powder of the target material into the copper cup of the target/cathode. Figure B.1 shows a filled copper cup.

B.1.2 Target assembly

- Screw the copper cup hand-screwed on the target holder (see Fig. B.2);
- Assemble the target holder. Take care of its rotation (Fig. B.3)! (*i.e.* find out if all connectors of the MISS are suitable for connection);
- Check the ionizer for short circuits and sufficient thickness (if the wire is too thin it should be replaced; the lifetime of an ionizer in permanent operation is about 10 weeks) (see Fig. B.4);
    - Is any electrical contact between the ionizer and the surrounding chamber?

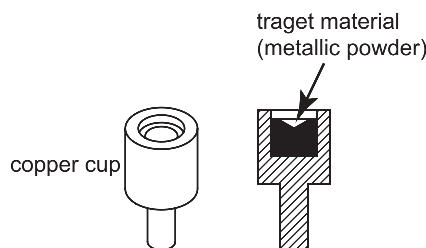

Fig. B.1: Copper cup (cathode), with sputter target material tamped in.

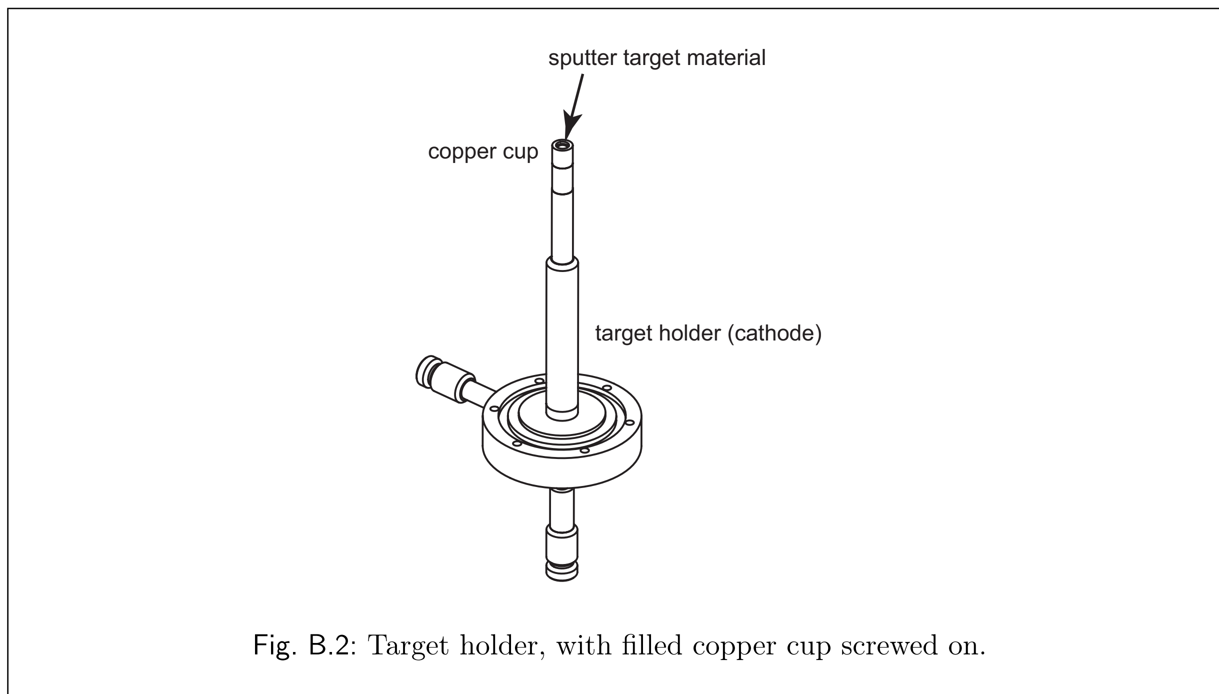

Fig. B.2: Target holder, with filled copper cup screwed on.

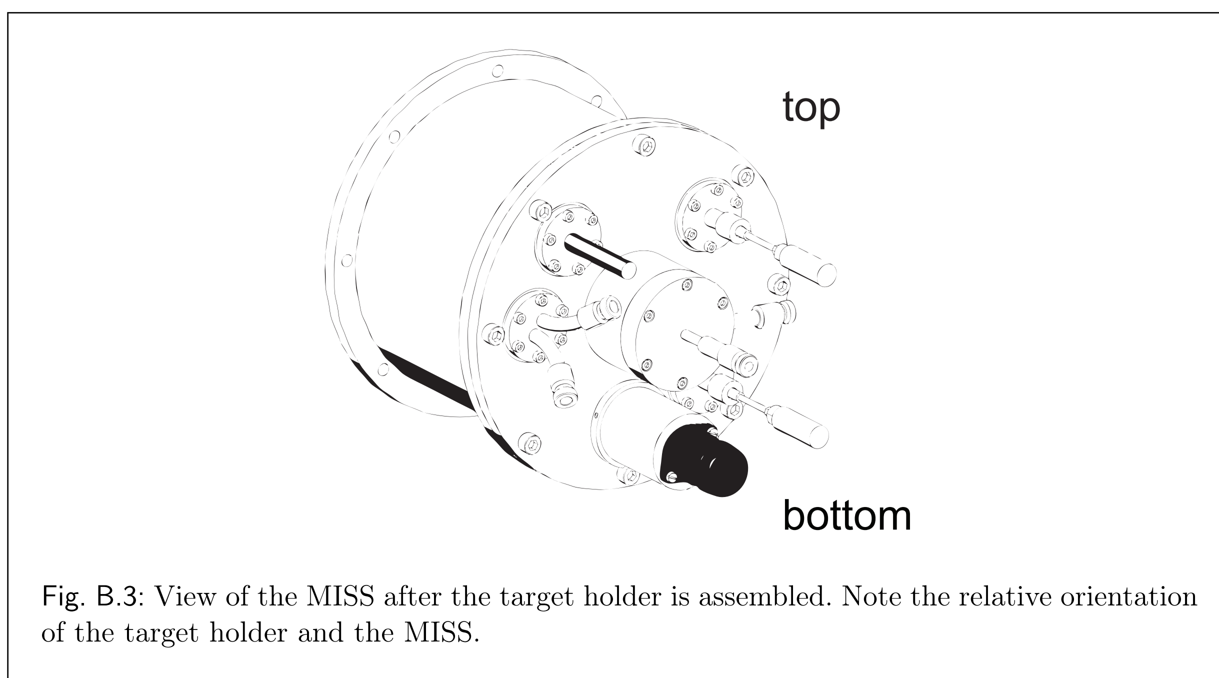

Fig. B.3: View of the MISS after the target holder is assembled. Note the relative orientation of the target holder and the MISS.

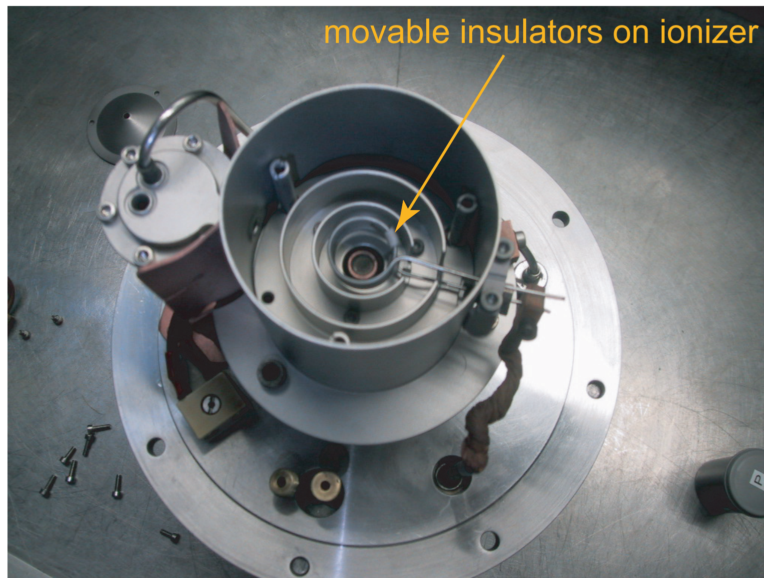

Fig. B.4: (Color.) The insulators on the ionizer can be moved in order to ensure a sufficient spacing between the windings of the ionizer coil and between ionizer and surrounding chamber.

  – Is the separation distance between the windings large enough? (move insulators if necessary);

B.1.3 Filling the cesium reservoir

- Everything should be prepared such that a quick flanging of the MISS is possible;
- Keep the cesium reservoir and copper gasket ready;
- Check if cesium channel (tube from cesium reservoir to inner chamber) is not blocked (*e.g.* insert wire or screwdriver);
- Check if channel of cesium ampule is not closed. If closed heat it (channel at the top) and wait until the cesium is drained from the channel;
- Fill liquid nitrogen into a bowl (the cesium ampule must be completely immersed in the liquid nitrogen!);
- Immerse cesium ampule in the liquid nitrogen with channel upwards (hold it with a gripper);

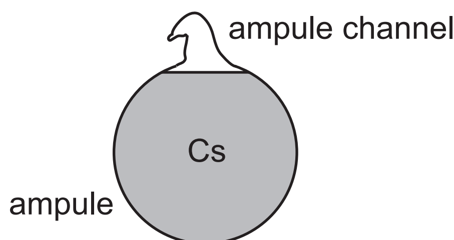

Fig. B.5: Cesium ampule with open channel (*i.e.* no cesium is in the top). After cooling this ampule in liquid nitrogen the channel can be removed (cut off). Afterward the entire ampule can be destroyed, while it is immersed in liquid nitrogen.

- When the cesium is solid take it out of the bowl and knock off the ampule channel with a hammer or similar tool. Place the ampule back into the liquid nitrogen;
- Fragment the ampule into little pieces;
- Place the cesium into the cesium reservoir (ampule fragments can also be inside but should not be too large);
- Quickly assemble the cesium reservoir (don't forget the copper gasket!);
- Tighten the screws successively along the circle;
- Reuse screws at most twice;
- Make sure that cesium reservoir is concentric to flange. It must not be inclined!
- Join electrical connectors of heating coil;
- Assemble the compressed air cooling coil;
- Quickly flange MISS
  - While working with the MISS or carrying the MISS the cesium reservoir must always be turned downward;
  - The vacuum pumps can be turned on as soon as two screws have been tightened;
  - Tighten all screws hand-tight;
- Join all connectors (compressed air, cooling water, electrical connectors...) and switch on the turbo molecular pumps.

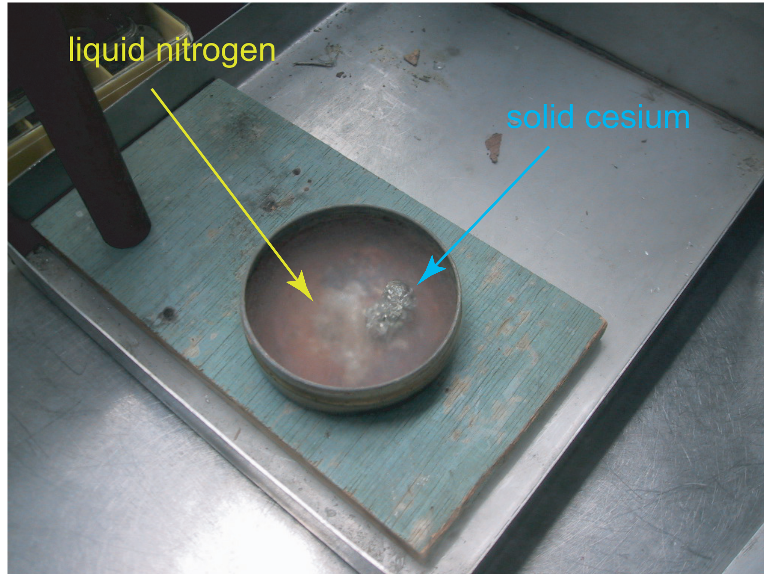

Fig. B.6: (Color.) Cesium in liquid nitrogen after the cesium ampule has been destroyed.

Fig. B.7: (Color.) This MISS is ready for assembly of the cesium reservoir and flanging.

B.2 Operation

B.2.1 Running up (heating up) the MISS

Once the vacuum is good enough ($\leq 10^{-5}$ mbar), the ionizer current can be turned on an initial value of 5 A. The current should be approximately linearly increased in time. Its final value of 25 A should be reached after about 45 minutes. During this process, it is important to always check if the vacuum remains good enough ($\leq 10^{-5}$ mbar), since surfaces are outgas due to the heating. If the previous process was already done and the MISS is still flanged, this heating process can be accomplished in 15 minutes instead of 45 minutes. This process is done to outgas the MISS as well to ensure the working temperature.

Furthermore, the cesium reservoir temperature and the temperature of the inner chamber should be checked all the time. The temperatures are measured with thermal elements. During this heating process, the temperature of the inner chamber increases to about 270°C and the temperature of the cesium reservoir to about 90°C. It should be taken care that the cesium reservoir temperature is at most 90°C. If it further increases, the rate of flow of cooling compressed air must be increased.

Once the MISS has reached its operating temperature and the heating procedure is finished, it can take several hours to maximize and stabilize the emitted beam current of the MISS. When our MISS was used for the first time it took about 5 hours to achieve an approximately constant beam current. The cathode voltage can be tuned up to 3 kV and the maximal recommended extraction voltage is 17 kV. Note that initially a lot of O^- is produced (see Fig. 3.12).

B.2.2 Desired values for operating the MISS

The setpoint values should only be exceeded for short time periods and only if necessary. The maximum values must never be exceeded, since parts of the MISS could be damaged.

Ionizer current I_i

setpoint	$I_\mathrm{i} \leq 30$ A
maximum value	$I_\mathrm{i,max} = 40$ A

Temperature of inner chamber T_{ic}

setpoint	$T_\mathrm{ic} \leq 300$°C
maximum value	$T_\mathrm{ic,max} = 350$°C

Current of heating coil of the cesium reservoir I_{Cs}

setpoint	$I_{\text{Cs}} \leq 0,2$ A
maximum value	$I_{\text{Cs}} = 0,2$ A

Temperature of the cesium reservoir T_{Cs}

setpoint	$90\ °\text{C} \leq T_{\text{Cs}} \leq 110°\text{C}$
maximum value	$T_{\text{Cs}} = 110°\text{C}$

For MISS at operating temperature and with an ionizer current between 20 A and 30 A, the temperature of the inner chamber depends approximately linearly on the ionizer current.

I_{i}	$T_{\text{inner chamber}}$
20 A	$\approx 200°\text{C}$
30 A	$\approx 300°\text{C}$

B.3 Cleaning

B.3.1 Dismantling of the MISS

If the MISS is to be dismantled immediately after its operation, it must be cooled down to at most 60°C, before dismantling. To achieve this as fast as possible all power supplies for the voltages as well for the heating currents should of course be switched off. On the other hand the cooling water and cooling compressed air should remain supplied. The cooling down of the MISS should then take about one to two hours. If there is no need for hurry, I suggest to let the MISS cool down to room temperature (*e.g.* over night) before dismantling, because the Cs reservoir should anyway not be opened before it is cooled down to room temperature. The lower the temperature of the remaining Cs is, the safer the opening of the MISS and the Cs reservoir is, because the lower the reactivity of Cs with oxygen from the air.

B.3.2 Dismantling step by step

- Switch all power supplies off;
- Let the MISS cool down to at most 60°C (room temperature is recommended);
- Turn off the cooling water circle and the compressed air;
- Connect the high voltage area to ground;
- Disconnect all connections/supplies from the MISS (unplug both water connections simultaneously not to make anything wet);
- Close the vacuum gate valve;
- Fill argon gas into the MISS vacuum chamber;
- Dismantle the MISS (mind that the Cs reservoir is downward while taking it out of the vacuum chamber and carrying it!);
- Place the MISS on the rack;
- Dismantle the Cs reservoir compressed air cooling helix and the heating coil;
- Dismantle the Cs reservoir and place it quickly on a corresponding rack into a sink and let water flow over it (danger of explosion!) until it is burned out;
- Spray a bit water on the Cs reservoir cap until no more Cs remains;
- Dismantle all parts that have come into contact with the sputtering material and/or Cs and clean them with a sand jet (if the Cs reservoir is still dirty after the cleaning with water also clean it in this way) (see Fig. B.8);
- Clean everything with alcohol;
- The MISS can now be reassembled and used again!

B.3.3 Circuit diagram

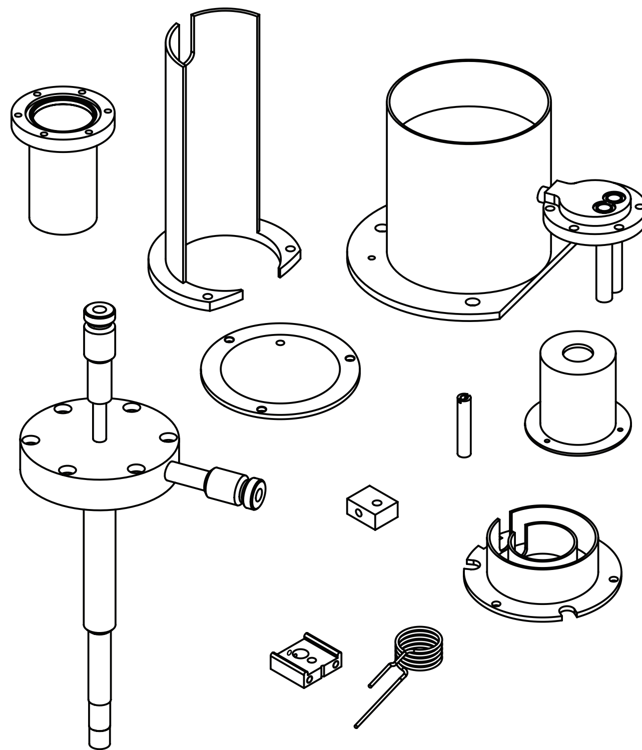

Fig. B.8: These parts should be cleaned.

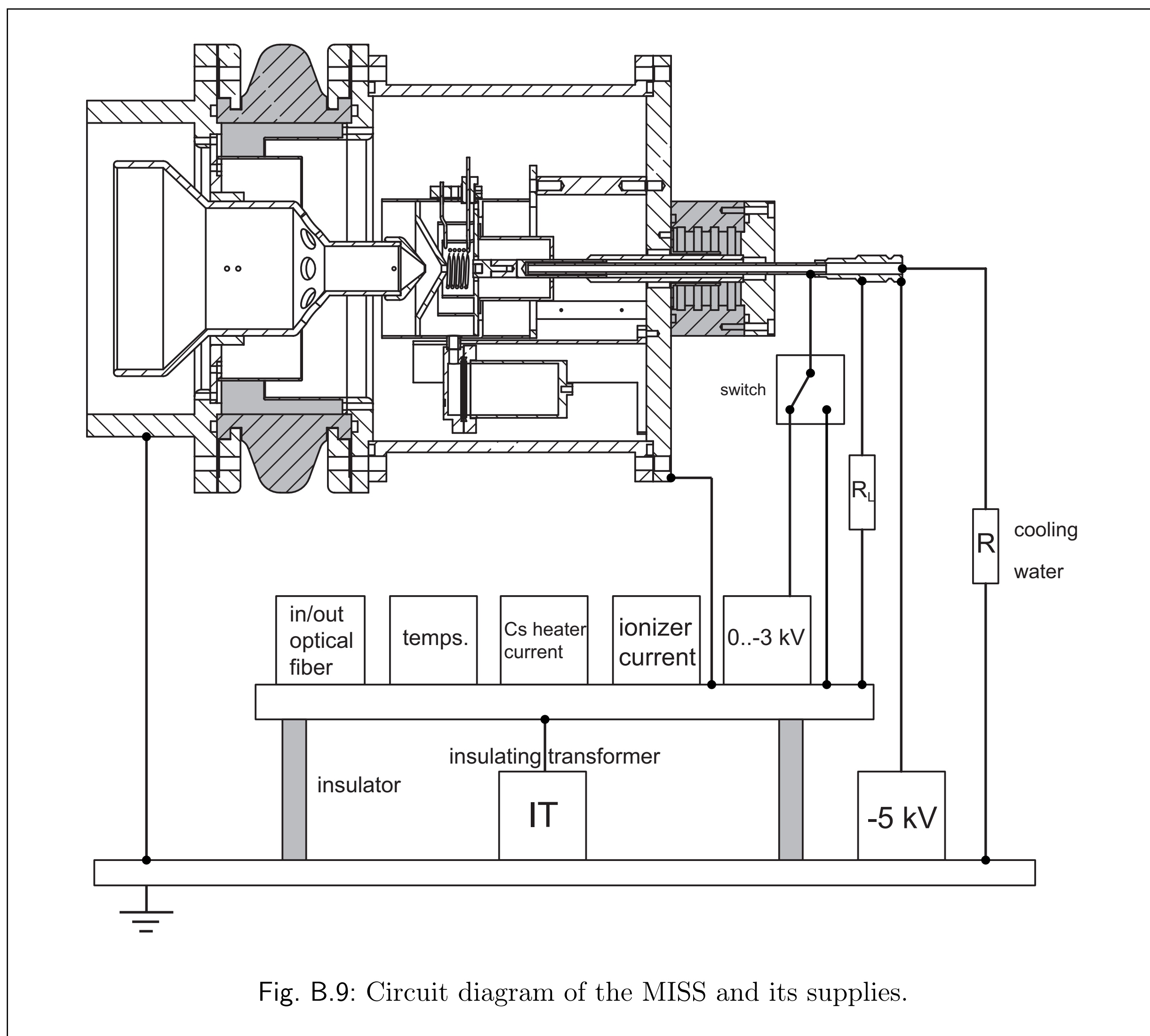

Fig. B.9: Circuit diagram of the MISS and its supplies.

BIBLIOGRAPHY

[1] Dirac P. A. M. 1931 *Proc. Royal Soc. A* 133 60.

[2] Anderson C. D. 1933 *Phys. Rev.* 43 491.

[3] Baur G. *et al.* 1996 *Phys. Lett. B* 368 251.

[4] Amoretti M. *et al.* 2002 *Nature* 419 456.

[5] Gabrielse G. *et al.* 2002 *Phys. Rev. Lett.* 89 213401.

[6] Gabrielse G *et al.* 2004 *Phys. Rev. Lett.* 93 073401.

[7] Madson N. *et al.* 2005 *Phys. Rev. Lett.* 94 033403.

[8] Kellerbauer A., Walz J. 2006 *New Journal of Physics* 8 45.

[9] Bilodeau R. C., Haugen H. K. 2000 *Phys. Rev. Lett.* 85 534.

[10] Andersen T., Haugen H. K., Hotop H. 1999 *J. Phys. Chem. Ref. Data* 28 1511.

[11] Wollnik H., 1987 *Optics of Charged Particles* Academic Press.

[12] Wolf B. 1995 *Handbook of Ion Sources* CRC Press.

[13] Hughes V. W., Schultz H. L. 1967 *Methods of Experimental Physics, Volume 4-Part A, Atomic and Electron Physics, Atomic Sources and Detectors* Academic Press.

[14] Nolting W. 2004 *Grundkurs Theoretische Physik 3 Elektrodynamik* Springer.

[15] Manura D. J., Dahl D. A. 2006 *SIMION Version 8.0 User Manual* Scientific Instrument Services, Inc.

[16] Bacal M., Reichelt W. 1974 *Rev. Sci. Instrum.* 45 769.

[17] Hinterberger F. 1997 *Physik der Teilchenbeschleuniger und Ionenoptik* Springer.

[18] Langmuir I., Kingdon K. H. 1925 *Proc. Roy. Soc. London* A107 61.

[19] Tompa G. S., Seidl M., Ermler W. C., Carr W. E. 1987 *Surf. Sci.* 185 453.

[20] Alton G. D. 1986 *Surf. Sci.* 175 226.

[21] Middleton R., Adams C. T. 1974 *Nucl. Instr. and Meth.* 118 329.

[22] Middleton R. 1983 *Nucl. Instr. and Meth.* 214 139.

[23] König M., 2007 *private communication*.

[24] Middleton R. 1989 http://tvdg10.phy.bnl.gov/COOKBOOK/ (unpublished).

[25] Moore R. B. 1993 *Hyp. Int.* 81 45.

[26] Großer J., 1983 *Einführung in die Teilchenoptik* Teubner.

[27] Brown I. G., 1989 *The Physics and Technology of Ion Sources* Wiley.

ACKNOWLEDGMENTS

I would like to thank Alban Kellerbauer for letting me join his group and giving me the chance of an autonomous and interesting work. It was both very stimulating and challenging to have the possibility of bringing own ideas into to project. Furthermore, I want to thank Ulrich Warring and Raoul Heyne for their very joyful and stimulating collaboration.
I am thanking Manfred König, Roland Repnow, Maximilian Trebis, Karl Hahn and Thomas Sieber for their help and advice. Michael Rappaport must be mentioned, who gave me the technical drawings of the quadrupole triplets used in our experiment and Jose Crespo for giving us the bending magnet and matching power supply. Thanks to Volker Mallinger and all the machinists of the workshop of the MPI-K, and Thomas Weber and Annika Zwilling from the design department.
I want to thank all people who helped our project and I apologize if I forgot to name someone directly.

ERKLÄRUNG:

Ich versichere, dass ich diese Arbeit selbstständig verfasst und keine anderen als die angegebenen Quellen und Hilfsmittel benutzt habe.

Heidelberg, den 02.12.2007